sid.inpe.br/mtc-m21d/2021/11.20.12.11-TDI

TSUJI BURNER AS A NUMERICAL LABORATORY TO STUDY SEVERAL ASPECTS OF DIFFUSION FLAME

Mariovane Sabino Donini

Doctorate Thesis of the Graduate Course in Engineering and Space Technology, guided by Drs. Fernando Fachini Filho, and Cesar Flaubiano da Cruz Cristaldo, approved in November 30, 2021.

URL of the original document:
<http://urlib.net/8JMKD3MGP3W34T/45R594E>

INPE
São José dos Campos
2021

PUBLISHED BY:

Instituto Nacional de Pesquisas Espaciais - INPE
Coordenação de Ensino, Pesquisa e Extensão (COEPE)
Divisão de Biblioteca (DIBIB)
CEP 12.227-010
São José dos Campos - SP - Brasil
Tel.:(012) 3208-6923/7348
E-mail: pubtc@inpe.br

BOARD OF PUBLISHING AND PRESERVATION OF INPE INTELLECTUAL PRODUCTION - CEPPII (PORTARIA Nº 176/2018/SEI-INPE):

Chairperson:

Dra. Marley Cavalcante de Lima Moscati - Coordenação-Geral de Ciências da Terra (CGCT)

Members:

Dra. Ieda Del Arco Sanches - Conselho de Pós-Graduação (CPG)

Dr. Evandro Marconi Rocco - Coordenação-Geral de Engenharia, Tecnologia e Ciência Espaciais (CGCE)

Dr. Rafael Duarte Coelho dos Santos - Coordenação-Geral de Infraestrutura e Pesquisas Aplicadas (CGIP)

Simone Angélica Del Ducca Barbedo - Divisão de Biblioteca (DIBIB)

DIGITAL LIBRARY:

Dr. Gerald Jean Francis Banon

Clayton Martins Pereira - Divisão de Biblioteca (DIBIB)

DOCUMENT REVIEW:

Simone Angélica Del Ducca Barbedo - Divisão de Biblioteca (DIBIB)

André Luis Dias Fernandes - Divisão de Biblioteca (DIBIB)

ELECTRONIC EDITING:

Ivone Martins - Divisão de Biblioteca (DIBIB)

André Luis Dias Fernandes - Divisão de Biblioteca (DIBIB)

sid.inpe.br/mtc-m21d/2021/11.20.12.11-TDI

TSUJI BURNER AS A NUMERICAL LABORATORY TO STUDY SEVERAL ASPECTS OF DIFFUSION FLAME

Mariovane Sabino Donini

Doctorate Thesis of the Graduate Course in Engineering and Space Technology, guided by Drs. Fernando Fachini Filho, and Cesar Flaubiano da Cruz Cristaldo, approved in November 30, 2021.

URL of the original document:
<http://urlib.net/8JMKD3MGP3W34T/45R594E>

INPE
São José dos Campos
2021

Cataloging in Publication Data

Donini, Mariovane Sabino.

D717t Tsuji burner as a numerical laboratory to study several aspects of diffusion flame / Mariovane Sabino Donini. – São José dos Campos : INPE, 2021.

xxiv + 130 p. ; (sid.inpe.br/mtc-m21d/2021/11.20.12.11-TDI)

Thesis (Doctorate in Engineering and Space Technology) – Instituto Nacional de Pesquisas Espaciais, São José dos Campos, 2021.

Guiding : Drs. Fernando Fachini Filho, and Cesar Flaubiano da Cruz Cristaldo.

1. Diffusion flames. 2. Buoyancy-driven flow. 3. Vortex breakdown. 4. Finite volume method. 5. Artificial compressibility method. I.Title.

CDU 544.452.2

Esta obra foi licenciada sob uma Licença Creative Commons Atribuição-NãoComercial 3.0 Não Adaptada.

This work is licensed under a Creative Commons Attribution-NonCommercial 3.0 Unported License.

MINISTÉRIO DA CIÊNCIA, TECNOLOGIA E INOVAÇÕES

INSTITUTO NACIONAL DE PESQUISAS ESPACIAIS

Serviço de Pós-Graduação - SEPGR

DEFESA FINAL DE TESE DE MARIOVANE SABINO DONINI
BANCA Nº 282/2021, REG 138843/2017.

No dia 30 de novembro de 2021, as 09h30min, por teleconferência, o(a) aluno(a) mencionado(a) acima defendeu seu trabalho final (apresentação oral seguida de arguição) perante uma Banca Examinadora, cujos membros estão listados abaixo. O(A) aluno(a) foi APROVADO(A) pela Banca Examinadora, por unanimidade, em cumprimento ao requisito exigido para obtenção do Título de Doutor em Engenharia e Tecnologia Espaciais/Combustão e Propulsão. O trabalho precisa da incorporação das correções sugeridas pela Banca e revisão final pelo(s) orientador (es).

Título: TSUJI BURNER AS A NUMERICAL LABORATORY TO STUDY SEVERAL ASPECTS OF DIFFUSION FLAME

Membros da Banca:

Dr. Fernando Fachini Filho – Presidente/Orientador – INPE
Dr. Cesar Flaubiano da Cruz Cristaldo – Orientador -UNIPAMPA
Dr. Márcio Teixeira Mendonça – Membro Interno - INPE
Dr. João Luiz F. Azevedo – Membro Externo – DCTA
Dr. Pascal Bruel – Membro Externo - CNRS

Documento assinado eletronicamente por **Fernando Fachini Filho**, **Pesquisador Titular**, em 07/12/2021, às 15:10 (horário oficial de Brasília), com fundamento no § 3º do art. 4º do Decreto nº 10.543, de 13 de novembro de 2020.

Documento assinado eletronicamente por **João Luiz Filgueiras de Azevedo (E)**, **Usuário Externo**, em 28/12/2021, às 22:32 (horário oficial de Brasília), com fundamento no § 3º do art. 4º do Decreto nº 10.543, de 13 de novembro de 2020.

Documento assinado eletronicamente por **Márcio Teixeira de menDONÇA (E)**, **Usuário Externo**, em 29/12/2021, às 07:54 (horário oficial de Brasília), com fundamento no § 3º do art. 4º do Decreto nº 10.543, de 13 de novembro de 2020.

Documento assinado eletronicamente por **Cesar flaubiano da cruz cristaldo (E)**, **Usuário Externo**, em 03/02/2022, às 18:23 (horário oficial de Brasília), com fundamento no § 3º do art. 4º do Decreto nº 10.543, de 13 de novembro de 2020.

A autenticidade deste documento pode ser conferida no site http://sei.mctic.gov.br/verifica.html, informando o código verificador **8503375** e o código CRC **4FC321D3**.

Referência: Processo nº 01340.007966/2021-12 SEI nº 8503375

"You're an interesting species. An interesting mix. You're capable of such beautiful dreams, and such horrible nightmares. You feel so lost, so cut off, so alone, only you're not.
See, in all our searching, the only thing we've found that makes the emptiness bearable, is each other".

CARL SAGAN
in *"Contact"*, 1985

To my parents Mario and Beatriz, to my sister Graciela
and to my beloved Carolina

ACKNOWLEDGEMENTS

Throughout the writing of this thesis, I have received a great deal of support and assistance. I would first like to thank my supervisor, Professor Fernando Fachini, whose expertise was invaluable in formulating the research questions, discussing the results and guiding my publications. Your insightful feedback pushed me to sharpen my thinking and brought my work to a higher level. My thanks are also forwarded to my co-advisor Dr Cesar Cristaldo, for his support and motivation throughout this study.

I would like to acknowledge my colleagues from my internship at LMAP/France for their wonderful collaboration and welcome. I would particularly like to single out my supervisor at LMAP, Dr Pascal Bruel. Pascal, I want to thank you for your patient support and for all of the opportunities I was given to further my research.

I gratefully acknowledge the funding received towards my Doctorate from the Coordination for the Improvement of Higher Education Personnel - CAPES. I am also very grateful for the grant Institutional Program for Internationalization - PrInt towards my doctorate sandwich.

In addition, I would like to thank my parents Mario and Beatriz, and my sister Graciela, for their wise counsel and sympathetic ear. My girlfriend Carolina, for her understanding and unconditional support throughout the years. You are always there for me. Finally, I could not have completed this thesis without the support of my friends, Raul, Jonas, Jhonatan, Liviany, Layrson, Fabíola, Rafael, Pedro, Puneeth, Victor, Ellen and many others, who provided discussions as well as happy distractions to rest my mind outside of my research.

ABSTRACT

The present work analyses cylindrical diffusion flames (Tsuji burner) along with the implementation of the unsteady artificial compressibility approach in the limit of a zero Mach number with constant and variable density. Combining a finite-volume approach on fully staggered meshes along with the artificial compressibility method, the resulting code proves to be versatile enough to cope with flow configurations ranging from unsteady cylinder wakes, heated cylinder or steady and unsteady diffusion flames with excellent accuracy, in the limits of the underlying physical modelling. The resulting numerical code has been used to simulate the Tsuji Burner in three main cases: steady Tsuji flame with forced convection, namely Classical Tsuji flame (Case A), steady Tsuji flame with natural convection with heated ambient atmosphere, namely Buoyant Tsuji Flame (Case B), and finally the unsteady Tsuji flame with natural convection at low Froude number, namely Puffing Tsuji Flame (Case C). The results for Case A show that the flame width is proportional to the mass stoichiometric coefficient and reciprocal to the Peclet number the 1/4 power and free stream velocity the 3/4 power, and that the flame height is proportional to the square of the mass stoichiometric coefficient and to the square root of the ratio of Peclet number to free stream velocity. The results for Case B showed that an increase of the ambient temperature leads to the appearance of a counterflow zone below the burner where the flame is undergoing very low levels of strain rate. The overall flame proves to be shorter than its counterpart observed in the forced convection regime, Case A. In addition, it is shown that an order of magnitude analysis is able to recover the sensitivity of the flame behaviour to the Péclet and Froude numbers as well as to the combustion parameters. In a certain range of the ambient-atmosphere temperature, the flow field changes dramatically: for the same boundary conditions, there are two steady-state solutions which depend on the initial conditions, i.e., the system presents a hysteresis. Lastly, the results for case C with constant density showed that the low-frequency instability generated by the displacement of the initial state of the flame was damped, eventually leading to a nonphysical stationary diffusion flame. In the variable density case C, the transient puffing flame was found and two instability mechanisms were highlighted, namely the Kelvin-Helmholtz mechanism near the cylinder and the Rayleigh-Taylor mechanism near the flame pinch-off. Finally, a parametric study varying the Froude number showed that the puffing regime for Tsuji flames follows the same relation as for jet flames, $St \propto Fr^{-1}$. However, it was found that the frequency level of the puffing Tsuji flames is not the same as described in the literature for jet and pool flames.

Keywords: diffusion flames. buoyancy-driven flow. vortex breakdown. finite volume method. artificial compressibility method.

QUEIMADOR TSUJI COMO UM LABORATÓRIO NUMÉRICO PARA O ESTUDO DE DIVERSOS ASPECTOS DA CHAMA DE DIFUSÃO

RESUMO

O presente trabalho analisa as chamas de difusão cilíndricas (queimador Tsuji) juntamente com a implementação da abordagem de compressibilidade artificial transiente no limite de um número Mach zero com massa específica constante e variável. Combinando uma abordagem de volume finito em malhas totalmente deslocadas junto com o método de compressibilidade artificial, o código resultante provou ser versátil o suficiente para lidar com configurações de escoamento que vão desde esteiras transientes em cilindro, cilindro aquecido ou chamas de difusão estacionarias e transientes com excelente precisão, nos limites da modelagem física subjacente. O código numérico resultante foi usado para simular o Queimador Tsuji em três casos principais: Chama Tsuji estacionária com convecção forçada, nomeadamente Chama Tsuji Clássica (Caso A), Chama Tsuji estacionária com convecção natural com atmosfera ambiente aquecida, nomeadamente Chama Tsuji Flutuante (Caixa B), e finalmente a chama transiente de Tsuji com convecção natural em baixo número de Froude, ou seja, a chama de Tsuji *puffing* (Caso C). Os resultados para o Caso A mostram que a largura da chama é proporcional ao coeficiente estequiométrico de massa e recíproca ao número de Peclet a 1/4 da potência e a velocidade do escoamento livre a 3/4 da potência, e que a altura da chama é proporcional ao quadrado do coeficiente estequiométrico de massa e à raiz quadrada da razão entre o número de Peclet e a velocidade do escoamento livre. Os resultados do Caso B mostraram que um aumento da temperatura ambiente leva ao aparecimento de uma zona de recirculação abaixo do queimador onde a chama está passando por níveis muito baixos de taxa de estiramento. A chama em geral prova ser mais curta do que sua contraparte observada no regime de convecção forçada, Caso A. Além disso, é mostrado que uma análise de ordem de magnitude é capaz de recuperar a sensibilidade do comportamento da chama aos números de Péclet e Froude, bem como aos parâmetros de combustão. Em uma determinada faixa de temperatura ambiente-atmosfera, o campo do escoamento muda drasticamente: para as mesmas condições de contorno, existem duas soluções de estado estacionário que dependem das condições iniciais, ou seja, o sistema apresenta uma histerese. Por fim, os resultados para o caso C com massa específica constante mostraram que a instabilidade de baixa frequência gerada pelo deslocamento do estado inicial da chama foi amortecida, levando a uma chama de difusão estacionária não física. No caso C de massa específica variável, a chama de *puffing* transiente foi encontrada e dois mecanismos de instabilidade foram destacados, a saber, o mecanismo Kelvin-Helmholtz próximo ao cilindro e o mecanismo Rayleigh-Taylor próximo ao estrangulamento da chama. Finalmente, um estudo paramétrico variando o número de Froude mostrou que o regime de *puffing* para chamas Tsuji segue a mesma relação que para chamas de jato, $St\ proptoFr^{-1}$. No entanto, verificou-se que o nível de frequência das chamas do Tsuji não é o mesmo descrito na literatura para chamas de jato e poça.

Palavras-chave: chamas de difusão. escoamento gerado por flutuabilidade. quebra de vórtice. método de volumes finitos. método de compressibilidade artificial.

LIST OF FIGURES

Page

CONTENTS

Page

1 INTRODUCTION

The main object of this study is the Tsuji Burner as a numerical laboratory for diffusion flames. This work was inspired by the importance of the geometry of the Tsuji Burner for the combustion domain, combined with the lack of exploration of different configurations besides the classical one. Moreover, the exploration of this diffusion flame geometry was closely related to the development of a self-developed numerical code for computational fluid dynamics, hence the term "numerical laboratory" used in the text.

The classical configuration of Tsuji Burner consists of a fuel ejection from a porous cylinder into an oncoming air stream such that a free stagnation line parallel to the cylinder axis is formed upstream of the porous surface. This line lies in the plane of symmetry of a stagnation point boundary layer, and combustion occurs as a counterflow diffusion flame. This diffusion flame configuration was the main object of investigation of the experimental setup proposed in the seminal work of Tsuji and Yamaoka (1967).

The Tsuji burner is a simple geometry that allows access to several fundamental aspects of diffusion flames that are important for modelling processes of reacting fluid dynamics. For example:

a) diffusion flames in the counterflow regime are found upstream and around the axis of symmetry and the flame properties from this configuration are used in modelling turbulent combustion;

b) the flame is very long and slender downstream of the burner;

c) long flames provide a large residence time for intermediate chemical species, e.g., C_2H_2 and C_3H_3, within the flame, which favours soot formation;

d) long flames are unstable with a characteristic frequency that can be coupled to the natural frequency of the chamber, resulting in flickering combustion instability; and

f) the interaction between the flame and the vortex breaks up the flame and the resulting fuel ball is taken by the flow and burns, resulting in the so-called puffing flames regime.

The applications of all the results from these analyses are as numerous as the fundamental aspects uncovered. For example:

a) long and sooty flames aiming at heat transfer by thermal radiation;

b) development of new combustion chambers;

c) safety issues related to fire propagation under normal conditions and also in microgravity (the covering protection of electric wires can be burnt in case of a short circuit and the flame can ignite other material in the vicinity);

d) also in safety issues, the dynamics of the detached flame ball can determine the spread of the fire;

e) by controlling the ambient temperature, it is possible to control the shape of the flame, which allows simulating a certain level of microgravity on the surface of the Earth.

In addition to the knowledge of the basic processes conveyed by Tsuji flames and their applications, the analysis of the proposed work requires the development of a self-developed numerical code (solver) suitable to simulate compressible flows in the regime of zero Mach number.

The aim of this work is to analyse the total diffusion flame formed in the Tsuji burner (horizontal cylindrical burner from which the fuel is injected) under the influence of forced convection and buoyancy, which in the latter, the cases studied here, are controlled by the ambient temperature. This low-speed buoyant diffusion flame enforces a flow field in the zero Mach regime, which requires a special treatment for its simulation. The use of this burner allows the employment of the steps to build the treatment of the zero Mach number framework in the context of a new numerical code.

The present work is divided into three parts, as follows:

- **Part I:** It deals with the phenomenology of the physical problems that arise in the subject of this work. Here, the Tsuji burner configurations used and their main properties are explained. Then, the puffing flames are presented as an important flame behaviour for one of the Tsuji burner configurations studied.

- **Part II:** It focuses on the modelling and numerical tools used to solve the proposed problem. In this part, the numerical solution method and the motivation for choosing such a method are presented. Moreover, the specifics

of the verification and validation cases for the self-developed numerical code are presented.

- **Part III:** This part consists of all the obtained results and their discussions.

Part I

Phenomenology

2 INTRODUCTION TO THE PHENOMENOLOGY OF THE TSUJI BURNER

It is seen in the literature that the Tsuji burner in a uniform forced flow, as showed schematically in Figure 2.1, is used to establish a counterflow diffusion flame (Tsuji flame) (TSUJI, 1982), from which the flamelet properties are determined (PETERS, 1983; PETERS, 1984); with curvature in one direction around the stagnation point. It is possible to control the stretch rate around the counterflow and its position in relation to the burner changing the fuel injection velocity and the air velocity, which permits to study the influence of the stretch rate and the heat loss on the flame stability. In general, the stretch rate is large, which leads to reactants leakage through the flame and, above a critical value, extinction occurs. Special experimental sets are constructed to obtain low stretch rates, i.e. planar flames (JACONO et al., 2005) and impinging flow onto low curvature body (HAN et al., 2005).

Figure 2.1 - Schematic picture of the diffusion flame established around a horizontal cylindrical burner in an uniform flow field (the velocity in y direction). $\hat{v}_\infty$ is the inlet forced convection and $\hat{u}_b$ is the burner fuel injection.

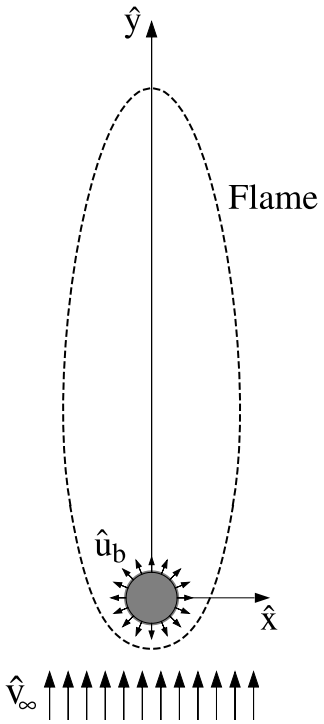

SOURCE: The Author.

In the present work, the surrounding (ambient) temperature of the burner is increased to reduce the buoyancy and, consequently, the flow velocity around the stagnation point, which permits obtaining low stretch rates, and to modify the flame shape. As pointed by a preliminary analysis through an incompressible model (DONINI et al., 2020), the increase of the ambient temperature generates a vortex downstream close to the burner through the combination of the positive buoyancy of hot flame gases and negative buoyancy of cold fuel vapour. The presence of that vortex changes drastically the flame shape, increasing the flame width about four times and the flame height almost twice.

By reducing the buoyancy with an increase in temperature, the velocity decreases, which extend the transport of heat through conduction to farther regions around the flame. Then, the region of high temperature gases increases, which is responsible for augmenting the heat loss by radiation. Therefore the stability of the flame in the downstream in the region far from the burner is influenced strongly by radiation heat loss (BONNE, 1971).

In a recent study (BIANCHIN et al., 2019), flames established by the Tsuji burner without casting the backside of the burner is found to be very large. Long flame means enough time to any perturbation to evolve. Taking into account the velocity profile to be proper to generate Kelvin-Helmoltz hydrodynamic instability (due to inflection on the curvature), one can expect transient process along the flame.

Besides that instability, previous exploratory analysis showed the interaction of Kelvin-Helmoltz instability and the vortices close to burner. This coupling makes the vortices change their properties. In addition, the modification on the flow field affect directly the flame.

Throughout the text, the Tsuji burner will be classified into two main categories:

- The classical Tsuji burner: The classical configuration means that there is forced convection carrying the oxidant from the bottom and the buoyant force is negligible. This configuration strongly correlates with the one used in the seminal Tsuji paper.

- The buoyant Tsuji burner: in the buoyant configuration, there is no inlet forced convection and the buoyant force plays the essential role of carrying

the oxidant towards the cylindrical burner by entrainment.

The buoyant configuration, so far as it is concerned, is divided into steady and unsteady cases.

The problem addressed in this thesis is the use of the above mentioned Tsuji burner configurations as a "numerical laboratory" for studying several aspects involving diffusion flames.

2.1 The classical Tsuji flame

While under normal gravity conditions, the forced convection transport is not separated from the natural convection transport in combustion problem, in microgravity environments the forced convection transport has no contribution of natural one. Then, the understanding of the whole (forward and backward) Tsuji flame under forced convection is important to, e.g., prevent accidental fire in spaceship.

Diffusion flames established around cylindrical burner with oxidant provided by the ambient atmosphere do not exist in steady state (BUCKMASTER; LUDFORD, 1982). The diffusive transport from the atmosphere to the burner is unable to supply oxidiser mass flux in stoichiometric proportion corresponding to the fuel mass flux provided by convective and diffusive transport from the burner to maintain a flame at a stationary position. It implies one-dimensional cylindrical diffusion flames to be inherently unsteady (QIAN; LAW, 1997). Therefore, cylindrical diffusion flames depend at least on two variables: one temporal and one spatial, or two spatial. The latter case is well known and found around the Tsuji burner: a forced convection around a cylindrical burner from which the radial fuel injection causes a second spatial coordinate dependence (TSUJI; YAMAOKA, 1967). The main focuses of Tsuji burner analyses have been the dependence of flame morphology on the forced convection and extinction of the flame forward the burner. The diffusion flame established in Tsuji burner is very long, thus, to shorten it, the backward part of the cylindrical burner was covered to reduce the fuel mass injection and allowing also the establishment of a recirculating flow zone. Since the flame height is very large compared to the cylindrical burner radius, numerical simulations are performed in a truncated domain from which only information about the flame close to the burner is obtained, e.g. envelope flame, side flame, wake flame and liftoff flame (CHEN; WENG, 1990; TSA; CHEN, 2003). No effort, however, has been dedicated on revealing the processes controlling the flame width far from the burner and the flame height.

2.2 Steady buoyant Tsuji flame

The strain rate of the counterflow region of the buoyant Tsuji flame is determined by the fuel injection velocity and the position of the stagnation point imposed by the component of the velocity along the flame driven by the buoyancy. The proposed strategy for reducing the strain rate is to reduce the buoyancy, not by reducing the gravitational acceleration, but by changing the density differences.

The buoyant force is given by $\hat{g}(\hat{\rho}_\infty - \hat{\rho})$ and in the present work, the density $\hat{\rho}$ satisfies $\hat{\rho}_f \leq \hat{\rho} \leq \hat{\rho}_b$, in which $\hat{g}$ is the gravity acceleration and $\hat{\rho}_f$, $\hat{\rho}_\infty$ and $\hat{\rho}_b$ are density of the gases in the flame, in the ambient-atmosphere and in the burner, respectively. A schematic of the problem showing the ambient-atmosphere and burner regions is exhibited in Figure 2.2. The conditions addressed in this analysis are such that $\hat{\rho}_f \leq \hat{\rho}_\infty \leq \hat{\rho}_b$. Thus, in the region with density in the range $\hat{\rho}_f \leq \hat{\rho} \leq \hat{\rho}_\infty$, the buoyant force is positive, $\hat{g}(\hat{\rho}_\infty - \hat{\rho}) \geq 0$, implying that the velocity of the fluid is positive. Meanwhile, in the region with density in the range $\hat{\rho}_\infty \leq \hat{\rho} \leq \hat{\rho}_b$, the buoyant force is negative, $\hat{g}(\hat{\rho}_\infty - \hat{\rho}) \leq 0$, implying that the velocity of the fluid can be negative, which is the condition of the gases in the lower part of the burner. Inside the flame, the density varies from the hot gases density around the flame up to cold gases density close to the burner, i.e., $\hat{\rho}_f \leq \hat{\rho} \leq \hat{\rho}_b$. Outside the flame, the density varies from the hot gases density, around the flame, up to cold gases density of the ambient atmosphere, i.e., $\hat{\rho}_f \leq \hat{\rho} \leq \hat{\rho}_\infty$. Hence, decreasing the ambient-atmosphere density through the increase of the temperature, the difference of density $(\hat{\rho}_\infty - \hat{\rho}_f) > 0$ diminishes, consequently, the positive buoyancy is reduced and the result is a low upward velocity along the flame. However, inside the flame, gases are found in the density range $\hat{\rho}_\infty \leq \hat{\rho} \leq \hat{\rho}_b$, and, consequently, the buoyant force is negative, $\hat{g}(\hat{\rho}_\infty - \hat{\rho}) < 0$. Then, the cold fuel ejected from the forward part of the burner is accelerated by the action of negative buoyancy. The downward velocity of the cold fuel increases and the stagnation point is established farther from the burner.

Therefore, the increase of the ambient-atmosphere temperature leads to the reduction of the positive buoyancy of the hot gases, and to the increase of the negative buoyancy of cold gases. The combination of these two forces by the systematic variation of the temperature of the ambient atmosphere will be used to achieve a low strain rate in the lower region of Tsuji diffusion flame.

The rise in the ambient-atmosphere temperature not only reduces the positive buoyancy intensity and augments the negative buoyancy intensity but it also impacts

their distribution. These changes in the buoyant force modify the flow field and consequently the flame properties. Unexpectedly, a drastic change is observed in the flow field in a specific range of ambient atmosphere temperature. The upper vortex in the wake of the burner is breaking in two. One of them is established close to the position of the primary vortex, but the other is established forward the burner.

Figure 2.2 - Problem schematic (horizontal porous cylinder with fuel injection). Close to the burner, the flame presents a cylindrical geometry driven by the fuel injection, but, above the burner, a rectangular geometry driven by the buoyancy.

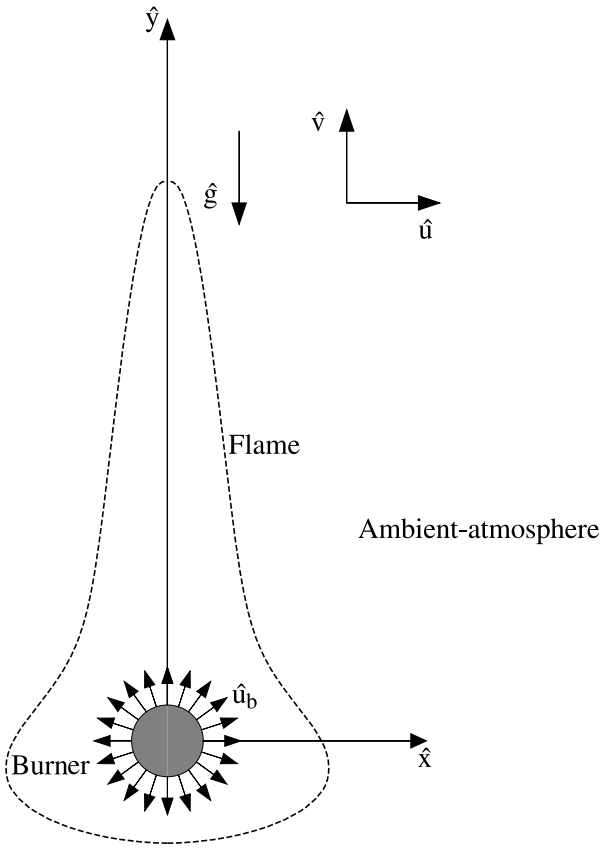

SOURCE: The Author.

3 PHENOMENOLOGY OF PUFFING FLAMES

The low frequency oscillations of buoyant diffusion flames have been known for a long time with the direct observation of candle or of any other light source using solid or liquid fuels. The intrinsically periodic behaviour of those flames was recorded initially by photographs of flame (CHAMBERLIN; ROSE, 1928; KIMURA, 1965; CHEN; ROQUEMORE, 1986), by Schiliren photographs (TOONG et al., 1965; GRANT; JONES, 1975; EICKHOFF; WINANDY, 1985) and by photographs from seeded flow (reactive Mie scattering technique)(CHEN et al., 1988). The low frequencies of flame oscillations (flame flickering) are around 15 Hz and independent on the fuel type (CHAMBERLIN; ROSE, 1928), on the geometry of the source of fuel, and on the flow field in the wake, regarding jet flames and pool fires (TOONG et al., 1965). The coupling among flow field (accelerating around the flame and decelerating in the plume above it), temperature and species field found in buoyant diffusion flames imposes the formation of large vortex outside the flame (WOHL et al., 1949). As the vortex displaces along the flame in direction of the tip, it is forced against the flame. Close to the flame tip, the vortex strangles the flame, a neck is established, large strain rate leads to extinguish locally the flame ending up to the separation of part of the flame tip, in which it is carried out by the flow (CHEN et al., 1988). Using toy models, it is shown that the main process controlling the hydrodynamic instability observed out of the flame is the density gradient effect on the flow field besides the buoyancy.

In general, it would be expected that the mechanisms controlling plume instability could be the same as those controlling buoyant diffusion flame. The reason for that it would be the accelerating flow in both cases. However, the geometrical factor and the increasing acceleration of the flow around flame give a particular character to the buoyant diffusion flames (FLEMING, 1982).

By making use of linear analysis, it was found frequency of 28 Hz for flame oscillation (KIMURA, 1965), which does not agree with experimental results (CHAMBERLIN; ROSE, 1928; KIMURA, 1965; TOONG et al., 1965; DURãO; WHITELAW, 1974; GRANT; JONES, 1975). Even considering the flow and temperature field in the region of the flame and downstream it (KIMURA, 1965; GRANT; JONES, 1975), the failure of the linear analysis on the low frequency prediction is due to no inclusion of the buoyancy. With a infinite candle model (diffusion flame established between two large reservoirs of fuel and oxidant) and buoyancy-induced flow, it is found that the frequency increases with distance from the burner rim and, chosen a proper position, the frequency of 17 Hz is determined (BUCKMASTER; PETERS, 1986). The result of

frequency dependence on the distance from the rim is in accordance with the stability analysis of buoyancy-driven flow in vertical heated plate (BUCKMASTER; PETERS, 1986).

As pointed out, numerical simulations of toy (simplified) models are used to observe the influence of individual process or group of them on the structure and stability of jet flame established by buoyancy-driven flow. The numerical results are able to describe the recirculation zones, the flame bulge formation and displacement, small counter-rotating and large vortices outside the flame, the frequency of about 13Hz of flame oscillation and the flame necking and separation at the same frequency (ELLZEY; ORAN, 1990; DAVIS et al., 1992; CHEN et al., 1992; KATTA; ROQUEMORE, 1993).

The flickering frequency is independent on flux and type of fuel, but is not on the size of the burner (pool). The frequency decreases with the burner diameter according to $f = 1.68D^{-1/2}$ (MALALASEKERA et al., 1996). This line is a good approximation of the data presented by Malalasekera et al. (1996), although the scatter is considerable for burners smaller than $0.01m$ in diameter. In the order hand, since the large scale instability is produced by the buoyancy, the frequency increases with its strength, described by Strouhal number as a function of Froude number, $St = 0.29Fr^{-1}$ (DUROX et al., 1995; MALALASEKERA et al., 1996; SATO et al., 2000; SATO et al., 2002; SATO et al., 2008; XIA; P.ZHANG, 2018). The break of the flame in two parts, one attached on the burner and the other carried out by the flow occurs only for certain conditions. The main of them is the length of the flame, controlled by the degree of dilution of the fuel stream. This characteristic reveals the dependency of the breaking process on the evolution of the large vortex out of the flame (CARPIO et al., 2012).

Detail analysis of the outer vortex shows that it presents a absolute instability in its genesis. However, for a wavelength larger than a critical value, the outer vortex loses the previous behavior and becomes convective unstable, explaining its displacement along the flame (SEE; IHME, 2014; MORENO-BOZA et al., 2016)

Part II

Modelling and numerical tools

4 FORMULATION

4.1 Governing equations

The transport coefficients (dynamic viscosity $\hat{\mu}$, thermal conductivity $\hat{k}$, and species diffusivity $\hat{D}_i$) are functions of the temperature and the thermodynamic coefficient (constant pressure specific heat $\hat{c}_p$) is considered constant. In the following and unless stated otherwise, any quantity $\hat{\Gamma}$ is dimensional whereas its dimensionless counterpart is written as Γ. The governing equations include the conservation equations for mass, momentum, energy and species:

$$\frac{\partial \hat{\rho}}{\partial \hat{t}} + \hat{\nabla} \cdot \hat{\rho}\hat{\mathbf{v}} = 0 \tag{4.1}$$

$$\frac{\partial \hat{\rho}\hat{\mathbf{v}}}{\partial \hat{t}} + \hat{\nabla} \cdot \hat{\rho}\hat{\mathbf{v}}\hat{\mathbf{v}} = -\hat{\nabla}\hat{p} + \hat{\nabla} \cdot \overline{\overline{\hat{\tau}}} + (\hat{\rho} - \hat{\rho}_\infty)\hat{\mathbf{g}} \tag{4.2}$$

$$\frac{\partial \hat{\rho}\hat{c_p}\hat{T}}{\partial \hat{t}} + \hat{\nabla} \cdot \hat{\rho}\hat{c_p}\hat{\mathbf{v}}\hat{T} = \hat{\nabla} \cdot (\hat{k}\hat{\nabla}\hat{T}) + \hat{\mathbf{v}} \cdot \hat{\nabla}\hat{p} + \hat{\Phi} + \hat{Q}\hat{w} \tag{4.3}$$

$$\frac{\hat{\rho}\partial Y_i}{\partial \hat{t}} + \hat{\nabla} \cdot \hat{\rho}\hat{\mathbf{v}}Y_i = \hat{\nabla} \cdot (\hat{\rho}\hat{D}_i\hat{\nabla}Y_i) - s_i\hat{w} \tag{4.4}$$

in which the subscript represent $i = F$ for fuel and $i = O$ for oxidant, $\hat{\mathbf{g}} = (0, \hat{g}, 0)$, $\hat{w} = \hat{\rho}BY_O{}^{\nu_1}Y_F{}^{\nu_2}e^{-\hat{E}_a/(\hat{R}\hat{T})}$ (B is frequency factor, $\hat{R}$ is constant of gases, and $\hat{E}_a$ is the activation energy) is the reaction rate, $\hat{Q}$ is the heat released by the combustion, and $\hat{\Phi}$ is the dissipation function defined as $\hat{\Phi} = \overline{\overline{\hat{\tau}}} : \hat{\nabla}\hat{\mathbf{v}}$.

In the zero Mach number approximation utilised here, the pressure variations can be neglected in the first approximation when writing the equation of state, which therefore reduces to $\hat{\rho}\hat{T} = 1$. Furthermore, in this zero Mach number limit, the viscous stress term proportional to the second viscosity coefficient can be incorporated in the definition of the variable p that represents in Equation 4.2 the pressure difference from the unperturbed ambient distribution. Correspondingly, the resulting viscous stress tensor reduces to $\overline{\overline{\hat{\tau}}} = \hat{\mu}(\hat{\nabla}\hat{\mathbf{v}} + \hat{\nabla}\hat{\mathbf{v}}^T)$,with both p and $\overline{\overline{\hat{\tau}}}$ scaled with the characteristic value of the dynamic pressure. The power-law expression is $\hat{\mu}/\hat{\rho} = \hat{D}_i = \hat{k}/\hat{\rho}\hat{c}_p = \hat{T}^\sigma$, with $\sigma = 0.7$.

4.2 Adimensionalization

To reduce the number of variables and to be independent of system of unit, the equations are expressed in dimensionless form. Thus dimensionless variables used in the analysis are defined as

$$t \equiv \frac{\hat{t}}{\hat{t}_c}, \quad x \equiv \frac{\hat{x}}{\hat{L}_c}, \quad y \equiv \frac{\hat{y}}{\hat{L}_c}, \quad z \equiv \frac{\hat{z}}{\hat{L}_c},$$

$$\rho \equiv \frac{\hat{\rho}}{\hat{\rho}_c}, \quad \mathbf{v} \equiv \frac{\hat{\mathbf{v}}}{\hat{V}_c}, \quad p \equiv \frac{\hat{p}}{\hat{p}_c}, \quad T \equiv \frac{\hat{T}}{\hat{T}_c}, \quad Y_F \equiv \frac{\hat{Y}_F}{\hat{Y}_{F0}}, \quad Y_O \equiv \frac{\hat{Y}_O}{\hat{Y}_{O\infty}},$$

$$\nabla \equiv \frac{\hat{\nabla}}{\hat{L}_c}, \quad \frac{\partial}{\partial t} \equiv \frac{1}{\hat{t}_c}\frac{\partial}{\partial \hat{t}}$$

The variables T, ρ, Y_F, Y_O are temperature, density, fuel mass fraction and oxidant mass fraction, respectively. All lengths are scaled with the reference length $\hat{L}_c$, the velocities with the reference velocity $\hat{V}_c$ and the temperature by the reference temperature $\hat{T}_c$. The time is non-dimensionalized using the residence time $\hat{t}_c = \hat{t}_r = \hat{L}_c/\hat{V}_c$. The pressure $\hat{p}$ is nondimentionalized by the reference pressure $\hat{p}_c = \hat{\rho}_c\hat{V}_c^2$. The transport coefficients are non-dimensionalized by their values from the ambient atmosphere, kinematic viscosity $\nu = (\hat{\mu}/\hat{\rho})/(\hat{\mu}_\infty/\hat{\rho}_\infty)$, the thermal diffusivity $\alpha = (\hat{k}/\hat{\rho}\hat{c}_p)/(\hat{k}_\infty/\hat{\rho}_\infty\hat{c}_{p\infty})$, and the species diffusivity $D_i = \hat{D}_i/\hat{D}_{i\infty}$. Where ∞ represents ambient conditions. All the reference parameters are defined separately for each case studied. Thereby, the nondimensional governing equations are

$$\frac{\partial \rho}{\partial t} + \nabla \cdot \rho\mathbf{v} = 0 \tag{4.5}$$

$$\frac{\partial \rho\mathbf{v}}{\partial t} + \nabla \cdot \rho\mathbf{v}\mathbf{v} = -\nabla p + \frac{1}{Re}\nabla \cdot \overline{\overline{\tau}} + \frac{1}{Fr^2}(1-\rho)\mathbf{e}_y \tag{4.6}$$

$$\frac{\partial \rho T}{\partial t} + \nabla \cdot \rho\mathbf{v}T = \frac{1}{Pe}\nabla \cdot (\rho\alpha\nabla T) + Ec\mathbf{v} \cdot \nabla p + \frac{Ec}{Re}\Phi + Q\dot{w} \tag{4.7}$$

$$\frac{\partial \rho Y_i}{\partial t} + \nabla \cdot \rho\mathbf{v}Y_i = \frac{1}{PeLe_i}\nabla \cdot (\rho\alpha\nabla Y_i) - s_i\dot{w} \tag{4.8}$$

where $Q \equiv \hat{Q}/(\hat{c}_p\hat{T}_c)$ is the dimensionless heat of combustion. The dimensionless

parameters $F_r \equiv \hat{V}_c/\sqrt{\hat{g}\hat{L}_c}$, $Re \equiv \hat{L}_c\hat{V}_c/\hat{\nu}$, $Ec \equiv \hat{V}_c^2/(\hat{c}_p\hat{T}_c)$, $P_r \equiv \hat{\nu}_\infty/\hat{\alpha}_\infty$ and $Le_i \equiv \alpha/D_i$ are Froude, Reynolds, Eckert, Prandtl and Lewis for the i species numbers, respectively, in which $i = F$ for fuel and $i = O$ for oxidant and $\hat{\nu}$ is the viscosity. Q is the rate of heat added by heat source and $\dot{w}_i = S_i\rho D_a {Y_O}^{\nu_1}{Y_F}^{\nu_2}e^{-E_a/T}$ is the net rate of work done on fluid element by surroundings, with $E_a \equiv \hat{E}_a/\hat{R}\hat{T}_\infty$. The parameter $Da \equiv B\mathrm{a}_0^{*2}\hat{Y}_{O\infty}^{\nu_1}\hat{Y}_{F0}^{\nu_2}/\alpha_\infty$ is the dimensionless Damköhler number. The viscous stress tensor is $\overline{\overline{\tau}} = \mu(\nabla\mathbf{v} + \nabla\mathbf{v}^T) + \frac{2}{3}\mu(\nabla\cdot\mathbf{v})\delta$, in which δ is the unit tensor.

4.2.1 Final governing equations

The operator ∇ is defined as

$$\nabla = \frac{\partial}{\partial x}\mathbf{e}_x + \frac{1}{x^\eta}\frac{\partial}{\partial y}\mathbf{e}_y + \frac{\partial}{\partial z}\mathbf{e}_z \tag{4.9}$$

where $\mathbf{e}_i$ is the unit vector and η is 0 for Cartesian Coordinates and 1 for Cylindrical Coordinates. The velocity vector is defined as $\mathbf{v} = [u, v]$.

Taking Equation 4.9 into the nondimensional governing equations, Equations 4.5-4.8 and neglecting the terms $Ec\mathbf{v}\cdot\nabla p + (Ec/Re)\Phi$, knowing that $Ec \equiv (\gamma-1)M^2 \to 0$ for the framework $M \to 0$ considered here. The final form of the governing equations are

$$\frac{\partial \rho}{\partial t} + \frac{1}{x^\eta}\frac{\partial (x^\eta \rho u)}{\partial x} + \frac{\partial(\rho v)}{\partial y} = 0 \tag{4.10}$$

$$\begin{aligned}\frac{\partial \rho u}{\partial t} + \frac{1}{x^\eta}\frac{\partial x^\eta \rho u u}{\partial x} + \frac{\partial \rho v u}{\partial y} = -\frac{\partial p}{\partial x} + \frac{1}{Re}\Bigg[&\frac{2}{x^\eta}\frac{\partial}{\partial x}\left(x^\eta\mu\frac{\partial u}{\partial x}\right) \\ &+\frac{\partial}{\partial y}\left(\mu\frac{\partial u}{\partial y}\right) - \frac{2}{3}\frac{1}{x^\eta}\frac{\partial}{\partial x}\left(\mu\frac{\partial (x^\eta u)}{\partial x}\right) - \frac{2}{3}\frac{1}{x^\eta}\frac{\partial}{\partial x}\left(x^\eta\mu\frac{\partial v}{\partial y}\right) + \frac{\partial}{\partial y}\left(\mu\frac{\partial v}{\partial y}\right) \\ &+\eta\left(-\frac{2\mu u}{x^\eta 2} + \frac{2}{3}\frac{\mu}{x^\eta 2}\frac{\partial (x^\eta u)}{\partial x} + \frac{2}{3}\frac{\mu}{x^\eta}\frac{\partial v}{\partial y}\right)\Bigg]\end{aligned} \tag{4.11}$$

$$\frac{\partial \rho v}{\partial t} + \frac{1}{x^\eta}\frac{\partial x^\eta \rho u v}{\partial x} + \frac{\partial \rho v v}{\partial y} = -\frac{\partial p}{\partial y} + \frac{1}{Re}\left[x^\eta \frac{1}{x^\eta}\frac{\partial}{\partial x}\left(x^\eta \mu \frac{\partial v}{\partial x}\right) + 2\frac{\partial}{\partial y}\left(\mu \frac{\partial v}{\partial y}\right)\right.$$
$$\left. -\frac{2}{3}\frac{\partial}{\partial y}\left(\frac{\mu}{x^\eta}\frac{\partial (x^\eta u)}{\partial x}\right) - \frac{2}{3}\frac{\partial}{\partial y}\left(\mu \frac{\partial v}{\partial y}\right) + \frac{1}{x^\eta}\frac{\partial}{\partial x}\left(x^\eta \mu \frac{\partial u}{\partial y}\right)\right] + \frac{1}{Fr^2}(1-\rho)\mathbf{e}_y \quad (4.12)$$

$$\frac{\partial \rho T}{\partial t} + \frac{1}{x^\eta}\frac{\partial x^\eta \rho u T}{\partial x} + \frac{\partial \rho v T}{\partial y} =$$
$$\frac{1}{Pe}\left[\frac{1}{x^\eta}\frac{\partial}{\partial x}\left(x^\eta \rho \alpha \frac{\partial T}{\partial x}\right) + \frac{\partial}{\partial y}\left(\rho \alpha \frac{\partial T}{\partial y}\right)\right] + Q\dot{w} \quad (4.13)$$

$$\frac{\partial \rho Y_i}{\partial t} + \frac{1}{x^\eta}\frac{\partial x^\eta \rho u Y_i}{\partial x} + \frac{\partial \rho v Y_i}{\partial y} =$$
$$\frac{1}{PeLe_i}\left[\frac{1}{x^\eta}\frac{\partial}{\partial x}\left(x^\eta \rho \alpha \frac{\partial Y_i}{\partial x}\right) + \frac{\partial}{\partial y}\left(\rho \alpha \frac{\partial Y_i}{\partial y}\right)\right] + Q\dot{w} \quad (4.14)$$

5 ELEMENTARY ASPECTS OF DIFFUSION FLAMES

We begin by introducing some essential aspects of diffusion flames, including the thermochemical parameters that plays the key role of determining the flame position and flame temperature when the irreversible chemical reaction is infinitely fast. This chemical reaction is addressed in this section, along with the parameters and variables that rises by introducing this consideration.

In the broadest sense, a diffusion flame may be defined as any flame in which the fuel and oxidizer initially are separated. With this usage, the term is synonymous with nonpremixed combustion . In a restricted sense, a diffusion flame may be defined as a non- premixed, quasisteady, nearly isobaric flame in which most of the reaction occurs in a narrow zone that can be approximated as a surface. This surface is a reaction sheet where the reaction occurs infinitely fast (WILLIAMS, 1985).

Figure 5.1 shows a typical configuration of diffusion flame with the reaction sheet assumption. As the fuel and oxidant are transported toward each other by diffusion and any convective motion of the system, they are heated and eventually meet at the reaction sheet. Fuel and oxidizer are each confined to their respective regions of supply, and reach vanishing concentrations at the reaction sheet. Consequently no leakage occurs. The reaction sheet acts as a sink for the reactants and a source of combustion heat and products (LAW, 2006).

Figure 5.1 - Diffusion flame temperature and concentration profiles with reaction-sheet assumption.

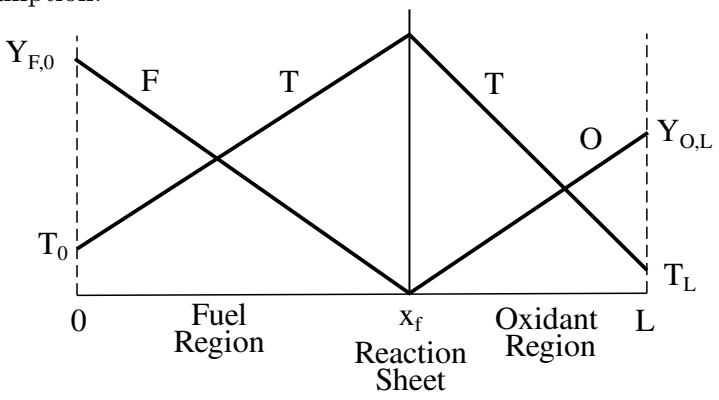

SOURCE: The Author.

5.1 The thermochemical parameters

For the totality of this study, focused on the fluid mechanics aspects of nonpremixed combustion, it is adopted the overall reaction

$$C_nH_{2n+2} + \frac{3n+1}{2}O_2 \rightarrow nCO_2 + (n+1)H_2O \tag{5.1}$$

as a description of the underlying stoichiometry for the oxidation a given hydrocarbon of the generic formula C_nH_{2n+2}. From Equation 5.1, the unit mass of fuel reacts with a mass $s = 8(3n+1)/(7n+1)$ of oxygen to give a mass $s_{CO_2} = 22n/(7n+1)$ and $s_{H_2O} = 9(n+1)/(7n+1)$ of CO_2 and s_{H2O}, respectively, releasing in the process an amount of energy given by $q = \frac{1}{2}(b^o_{C_nH_{2n+2}} - nb^o_{CO_2} - (n+1)b^o_{H_2O})/(7n+1)$, where b^o_i represents the enthalpy of formation per mole of species i. For all the combustion related cases studied in this thesis, the selected fuel is methane (CH_4), thereby, $s = 4$ and $\hat{Q} = 50.15kJ/g$. For other hydrocarbons that share the same molecular structure, the combustion properties, s and Q, differs by a small amount.

As showed in Figure 5.1, the streams that provide the air and the fuel in a diffusion-controlled combustion system are different. A fundamental thermochemical parameter plays an important role in nonpremixed combustion and is extensively remarked throughout this thesis, namely

$$s_O = s\frac{\hat{Y}_{F0}}{\hat{Y}_{O\infty}} \tag{5.2}$$

the mass of air that one needs to mix with unit mass of the gaseous fuel stream to generate a stoichiometric mixture. For air, $Y_{O\infty} \simeq 0.232$ and Y_{F0} stand for the mass fractions of oxygen and fuel in their respective streams. Diluted fuel-stream takes values $Y_{F0} < 1$, which is frequently admitted in experiments and numerical computations. Common values for S in a hydrocarbon-air flame with undiluted fuel stream, i.e. $Y_{F0} = 1$, initially at normal ambient temperature is $s_O = s/Y_{O\infty} \simeq 15$.

5.2 The limit of infinitely fast reaction and the Shvab-Zel'dovich formulation

A major difficulty in the solution of chemically reacting flows is the presence of the reaction term, which is not only nonlinear but also couples the energy and species equations, Equation 4.7 and 4.8. However, recognizing that the concentrations of

Y_F and Y_O species and the system enthalpy are related through stoichiometry, it is reasonable to expect that under suitable situations these quantities can be stoichiometrically combined such that the resulting term is not affected by chemical reactions in the flow. Such a combined quantity is called a coupling function (LAW, 2006).

To couple the energy and species equations, the Shvab-Zel'dovich formulation is applied and the assumption of an " infinitely fast chemical reaction rate" is considered. In this model the flame zone is of infinitesimal thickness and is represented by a surface rather than an extended reaction zone. In this model the Lewis number of i species is considered equal to unity. The goal of this formulation is to transform the system of three equations, Equation 4.7 for energy and Equation 4.8 for fuel and oxidant, in two linear equations as functions of Z and H, representing the mixture fraction and excess enthalpy, respectively. Neglecting the terms $Ec\mathbf{v}\cdot\nabla p+(Ec/Re)\Phi$ and combining Equation 4.7 and 4.8:

$$\frac{\partial}{\partial t}\begin{Bmatrix}\rho T\\ \rho Y_O\\ \rho Y_F\end{Bmatrix}+\nabla\cdot\begin{Bmatrix}\rho\mathbf{v}T\\ \rho\mathbf{v}Y_O\\ \rho\mathbf{v}Y_F\end{Bmatrix}= \nabla\cdot\begin{Bmatrix}\rho\alpha\nabla T/Pe\\ \rho\alpha\nabla Y_O/(PeLe_O)\\ \rho\alpha\nabla Y_F/(PeLe_F)\end{Bmatrix}+\begin{Bmatrix}Q\\ -s_O\\ -s_F\end{Bmatrix}\dot{w} \quad (5.3)$$

Knowing that $s_F = 1$, multiplying the second line by Le_O and the third by Le_F in Equation 5.3:

$$\frac{\partial}{\partial t}\begin{Bmatrix}\rho T\\ \rho Le_O Y_O\\ \rho Le_F Y_F\end{Bmatrix}+\nabla\cdot\begin{Bmatrix}\rho\mathbf{v}T\\ \rho\mathbf{v}Le_O Y_O\\ \rho\mathbf{v}Le_F Y_F\end{Bmatrix}= \frac{1}{Pe}\nabla\cdot\begin{Bmatrix}\rho\alpha\nabla T\\ \rho\alpha\nabla Y_O\\ \rho\alpha\nabla Y_F\end{Bmatrix}+\begin{Bmatrix}Q/Le_F\\ -Le_O s_O/Le_F\\ -1\end{Bmatrix}Le_F\dot{w}$$

Multiplying the third line by $S = s_O Le_O/Le_F$ and subtracting the second line:

$$\frac{\partial}{\partial t}\rho\left(Le_F SY_F - Le_O Y_O\right) + \nabla\cdot\rho\mathbf{v}\left(Le_F SY_F - Le_O Y_O\right) = \frac{1}{Pe}\nabla\cdot\left[\rho\alpha\nabla(SY_F - Y_O)\right]$$

Adding a unitary constant on the terms inside the derivatives:

$$\frac{\partial}{\partial t}\rho\left(Le_F SY_F - Le_O Y_O + 1\right) + \nabla\cdot\rho\mathbf{v}\left(Le_F SY_F - Le_O Y_O + 1\right) = \frac{1}{Pe}\nabla\cdot\left[\rho\nabla(SY_F - Y_O + 1)\right]$$

Defining mixture fraction by $Z = SY_F - Y_O + 1$ and $Le_O = Le_F = 1$:

$$\frac{\partial\rho Z}{\partial t} + \nabla\cdot\rho\mathbf{v}Z = \frac{1}{Pe}\nabla\cdot(\rho\alpha\nabla Z) \tag{5.4}$$

where the thermochemical parameter S is definded by Equation 5.2. Applying the Del operator (Equation 4.9) into the Equation 5.4, we have the final mixture fraction governing equation

$$\frac{\partial\rho Z}{\partial t} + \frac{1}{x^\eta}\frac{\partial x^\eta\rho uZ}{\partial x} + \frac{\partial\rho vZ}{\partial y} = \frac{1}{Pe}\left[\frac{1}{x^\eta}\frac{\partial}{\partial x}\left(x^\eta\rho D_T\frac{\partial Z}{\partial x}\right) + \frac{\partial}{\partial y}\left(\rho\alpha\frac{\partial Z}{\partial y}\right)\right] \tag{5.5}$$

Multiplying the first line in Equation 5.3 for $((S+1)Le_F/Q)$ and adding to the second and third line:

$$\frac{\partial}{\partial t}\rho\left(\frac{(S+1)Le_F}{Q}T + Le_F Y_F + Le_O Y_O\right) + \nabla\cdot\rho\mathbf{v}\left(\frac{(S+1)Le_F}{Q}T + Le_F Y_F + Le_O Y_O\right) = \frac{1}{Pe}\nabla\cdot\left[\rho\alpha\nabla\left(\frac{(S+1)Le_F}{Q}T + Y_F + Y_O\right)\right]$$

Defining the enthalpy excess $H = (S+1)Le_F T/Q + Y_F + Y_O$:

$$\frac{\partial \rho H}{\partial t} + \nabla \cdot \rho \mathbf{v} H = \frac{1}{Pe} \nabla \cdot (\rho \alpha \nabla H) \tag{5.6}$$

Again, applying the Del operator (Equation 4.9) into the Equation 5.6, we have the final enthalpy excess governing equation

$$\frac{\partial \rho H}{\partial t} + \frac{1}{x^\eta} \frac{\partial x^\eta \rho u H}{\partial x} + \frac{\partial \rho v H}{\partial y} = \frac{1}{Pe} \left[\frac{1}{x^\eta} \frac{\partial}{\partial x} \left(x^\eta \rho \alpha \frac{\partial H}{\partial x} \right) + \frac{\partial}{\partial y} \left(\rho \alpha \frac{\partial H}{\partial y} \right) \right] \tag{5.7}$$

The general Shvab-Zel'dovich formulation (Equations 5.4 and 5.6) describes the temperature and the oxygen and fuel mass fractions by determining the mixture fraction and the enthalpy excess functions in the fuel region and in the oxygen region. In the present model, is assumed that the combustion process occurs under condition of Damköhler number infinitely large ($D_a \gg 1$). In other words, the reaction characteristic time is infinitely smaller than any mechanical characteristic time. Thus, the reactants can not coexist, i.e., the flow field is divided in two domains separated by a reaction sheet. In the fuel region $Y_O = 0$ the oxygen concentration is zero. In the oxygen domain, $Y_F = 0$. Both reactants have zero concentration at the flame, where the chemical reaction takes place.

In order to obtain an equation to describe the temperature profile, the enthalpy excess and mixture fraction were combined resulting the following expression:

$$T(Z,H) = \begin{cases} Q[H - (Z-1)/S]/[(S+1)Le_F], & \text{for} \quad Z > 1 \\ \\ Q(H - Z - 1)/[(S+1)Le_F], & \text{for} \quad Z \leq 1 \end{cases} \tag{5.8}$$

In a similar way, the mass fraction is obtained through the mixture fraction distribution:

$$Y_i(Z) = \begin{cases} (Z-1)/S, & \text{for} \quad Z > 1 \\ \\ 1 - Z, & \text{for} \quad Z \leq 1 \end{cases} \tag{5.9}$$

6 PRESENTATION OF THE NUMERICAL METHOD

6.1 Numerical difficulties (zero and low Mach number flows)

The flow around the Tsuji Burner discussed at Part I of this thesis can be characterised as a low speed chemically reacting flow. This configuration is one example of cases that frequently pose difficulties for numerical simulation. The characteristic features of these flows are that the fluid velocity is much smaller than the acoustic speed in all or part of the domain, yet the variations in density are significant to restrain an incompressible formulation (WITHINGTON et al., 1991). For such flows characterised by a zero Mach number (i.e. $Ma << 1$), the pressure, supposed to be thermodynamically constant, is affecting the flow motion only through its spatial derivatives present in the momentum equations. Thus, the fact that the pressure field cannot be obtained from the equation of state indicates that a specific procedure has to be derived to accurately calculate this pressure field (CORVELLEC et al., 1999).

Another way of perceiving the problem of solving low speed reacting flows is by the investigation of the disparity among the system's eigenvalues (stiffness), that rises by the mathematical nature of the governing equations. At high Mach numbers, the conservation equations (specifically mass, momentum and energy) are closely linked, and conventional numerical algorithms for compressible flows normally show their best performance over this Mach number range. However, when the Mach number becomes very small, the inviscid compressible form of the conservation equations becomes poorly coupled and stiff. This can be understood physically in that, as the Mach number approaches zero, the sensible part of the fluid energy manifests itself in the form of pressure, with the energy equation effectively decoupled from the rest of the equations.

In extension to the eigenvalue stiffness problem, zero Mach number flows pose a numerical problem with a truncating error that can restrict the solution from reaching satisfactory accuracy. This error occurs in the estimation of the pressure and convective momentum flux terms in the momentum equation when the computer is forced to truncate relevant digits. Since these two terms differ greatly in magnitude when approximating zero Mach numbers (ratio being equivalent to the inverse of Mach number squared), significant errors are introduced that contaminate consequently the numerical solution (WITHINGTON et al., 1991).

In view of the above difficulties, the method to deal with the low speed reacting

flow problems applied in the present thesis is the Artificial Compressibility (AC) method. Originally introduced by Chorin (1967) for steady flows simulations, in this work is employed for unsteady variable-density flows. The next section discusses comprehensively the numerical and physical aspects of the AC method.

6.2 The artificial compressibility scheme

The artificial compressibility (AC) method is quite a well-established numerical approach for solving the (constant-density) incompressible Navier-Stokes equations. This method consists of modifying the continuity equation by adding a non-stationary pressure term. For the analysis in this section only, the continuity equation is used in its incompressible form, namely:

$$\frac{1}{\beta}\frac{\partial p}{\partial \tau} = -\nabla \cdot \mathbf{u} \tag{6.1}$$

in which p is the pressure, τ is an artificial non-physical time, $\mathbf{u}$ is the flow velocity vector and β is the artificial compressibility factor which scales as a velocity square.

Physically, this modification in the continuity equation means that waves of finite speed are introduced into the incompressible flow field as a way to distribute the pressure. For a truly incompressible flow, the wave speed is infinite, whereas the speed of propagation of the pseudo waves introduced by this formulation depends on the magnitude of the artificial compressibility parameter. In a true incompressible flow, the pressure field is affected instantaneously by a disturbance in the flow, but with artificial compressibility, there will be a time lag between the flow disturbance and its effect on the pressure field. Ideally, the value of artificial compressibility can be chosen as high as the particular algorithm allows, so that incompressibility is quickly restored, i.e., the artificial pressure waves are fully propagated.

The results are physically meaningful only when a steady-state solution in τ is reached and the original continuity equation is recovered automatically (BRUEL et al., 1996). The ongoing popularity and relative success of the artificial compressibility method to deal with constant density flow simulations are mainly due to its simplicity and clear physical interpretation. To obtain a time-accurate solution, a dual time-step technique can be employed (SOH; GOODRICH, 1988; ROGERS; KWAK, 1989; CORVELLEC et al., 1999; CHANG; KWAK, 1984). Accordingly, in addition to the aforementioned modification of the continuity equation, the non-physical time derivative of the velocity field is introduced in the momentum equation, namely

(dimensionless form):

$$\frac{\partial \mathbf{u}}{\partial t} + \frac{\partial \mathbf{u}^{\tau}}{\partial \tau} = -\nabla \cdot (\mathbf{u}\mathbf{u}) - \nabla p + \frac{1}{Re}\nabla^2 \mathbf{u} \tag{6.2}$$

where t is the physical time and Re the Reynolds number. These equations are iteratively solved such that the velocity field approaches its new value in physical time as its divergence goes towards zero. Thus, for each physical time step, the flow field has to go through one complete sub-iteration cycle in artificial-time.

The existence of the artificial-wave propagation phenomenon associated with the convergence towards the physically meaningful solution of the above set of equations can be evidenced by writing the momentum equation under a characteristics-like form (neglecting the viscous term and the physical time derivative and considering a one-dimensional configuration), namely:

$$\left[\frac{\partial u}{\partial \tau} + \frac{1}{(u \pm c)}\frac{\partial p}{\partial \tau}\right] + (u \pm c)\left[\frac{\partial u}{\partial x} + \frac{1}{(u \pm c)}\frac{\partial p}{\partial x}\right] = 0 \tag{6.3}$$

The artificial sound speed, c, and the corresponding artificial Mach number, M, are related to β by

$$c = \sqrt{u^2 + \beta}, \qquad M = \frac{u}{c} = \frac{u}{\sqrt{u^2 + \beta}} < 1 \tag{6.4}$$

Thus, artificial waves of finite speed are introduced to distribute the static pressure throughout the whole computational domain. The rate of convergence of the solution during the pseudo-time integration loop heavily depends on the value of β, and this can be thought of as a weak point of the method. Indeed, in order to converge to the steady-state solution during the course of each sub-iterations cycle in artificial-time, the waves associated to the hyperbolic nature of the artificial compressibility based system of equations have to undergo at least a one round-trip propagation to ensure the proper built-up of the pressure field (more precisely, of its gradient field) over the whole computational domain. Based on this representation, Chang and Kwak (1984) estimated the number N of artificial time-steps $\Delta\tau$ required to reach convergence in artificial time. By considering a characteristic length L of the computational domain over which the artificial waves must travel once forth and back, they obtained a lower bound for N expressed as:

$$N > \frac{\sqrt{1+\beta}}{\beta}\frac{2L}{\Delta\tau} \tag{6.5}$$

Compared to the numerous AC based simulations of constant density flows that can be found in the literature (quite a significant number of them have been recently recalled by Hodges (2020)), much less examples of AC based simulations of non-constant density flows have been reported or are discussed in CFD textbooks, to the noticeable exception of Oran and Boris (2005). In such cases featuring a non-constant density field (in space and/or in time), one can distinguish between configurations still featuring a divergence free velocity field (Bassi et al. (2018), Shapiro and Drikakis (2005)) from those which did not. For the latter, they are mostly related to the simulation of Mach zero reacting flows such as steady turbulent premixed flames (Bruel et al. (1996)), unsteady turbulent premixed flames (Corvellec et al. (1999), Dourado et al. (2004)), laminar confined and unconfined diffusion flames (Azarkhavarani et al. (2017), Bianchin et al. (2019), Donini et al. (2020)).

6.3 Method of solution and temporal discretization

The numerical solution of the Mach zero system of equations relies on a dual-step time-accurate artificial compressibility method. An explicit second-order Runge-Kutta Ralston's method was adopted for the artificial-time integration and the second-order Euler method was selected for the physical-time integration due to its simplicity of implementation in a dual-time step approach. By replacing the derivative terms with their numerical approximations, the resulting set of equations can be written in compact form as:

$$\frac{dq^{(ac)}}{d\tau} + \frac{dq}{dt} = RHS(q)_{i,j} \tag{6.6}$$

where $q = [\rho, u, \mathrm{v}, T]^T$ and $q^{(ac)} = [p/\beta, u, \mathrm{v}, T]^T$ are the vector of primitive variables for non reacting flows, and $q = [\rho, u, \mathrm{v}, Z, H]^T$ and $q^{(ac)} = [p/\beta, u, \mathrm{v}, Z, H]^T$ are those for reacting flows cases. $RHS(q)_{i,j}$ is the right-hand side of the discretized equation. Then, introducing the residual value for the artificial time step as:

$$Res\left(q^{n+1,\nu}\right)_{i,j} = \frac{-3q^{n+1,\nu} + 4q^n - q^{n-1}}{2\Delta t} + RHS\left(q^{n+1,\nu}\right)_{i,j} \tag{6.7}$$

permits to rewrite Equation 6.6 at times' step $(n+1, \nu+1)$ as:

$$\left.\frac{dq^{(ac)}}{d\tau}\right|^{n+1,\nu+1} = Res\left(q^{n+1,\nu}\right)_{i,j} \tag{6.8}$$

The integration steps in artificial-time are finally given by:

$$\begin{aligned} q^{(1)} &= \alpha_1 q^{n+1,\nu} + \phi_1 \Delta\tau \left[Res\left(q^{n+1,\nu}\right)/\Delta\Omega\right] \\ q^{(2)} &= \alpha_2 q^{n+1,\nu} + \phi_2 \left[q^{(1)} + \Delta\tau Res\left(q^{(1)}\right)/\Delta\Omega\right] \\ q^{n+1,\nu+1} &= \alpha_3 q^{n+1,\nu} + \phi_3 \left[q^{(2)} + \Delta\tau Res\left(q^{(2)}\right)/\Delta\Omega\right] \end{aligned} \tag{6.9}$$

where $(\alpha_1, \alpha_2, \alpha_3) = (1, 3/4, 1/3)$, $(\phi_1, \phi_2, \phi_3) = (1, 1/4, 1/3)$ and $\Delta\Omega$ is the cell volume.

To advance the solution by one physical time-step, the equations are iteratively solved in a segregated way such that $q^{n+1,\nu+1}$ approaches the new value q^{n+1} as the artificial time derivative approaches zero. For satisfying this constraint, the residual value $Res(q)_{i,j}$ of Equation 6.8 is set to reach values below $\varepsilon = 10^{-5}$. The flow chart of the algorithm to solve the system is presented in Figure 6.1.

Figure 6.1 - Flow chart of the algorithm.

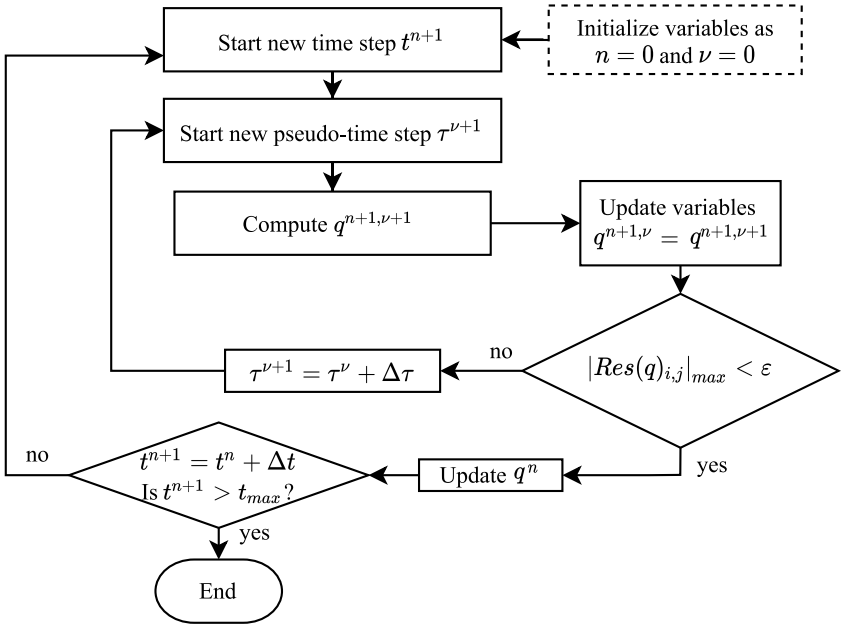

SOURCE: The Author.

6.4 Spatial discretization

6.4.1 The finite volume framework

Consider the generic transport equation for the property ϕ and assume that the velocity field and the fluid properties are known. The Finite Volume Method (FVM) has a start point the integral form of the balance equation:

$$\int_t \int_\Omega \frac{\partial(\rho\phi)}{\partial t} d\Omega dt + \int_t \int_A \rho\phi \mathbf{v} \cdot \mathbf{n} dA dt = \int_t \int_A \Gamma_\phi \nabla\phi \cdot \mathbf{n} dA dt + \int_t \int_\Omega S_\phi d\Omega dt \quad (6.10)$$

It is worth to note that both steady and unsteady systems have the same treatment of the finite volume integration of Equation 6.10 over a grid volume.

At this point the computational domain is subdivided into a finite number of small grid cell volumes by a grid which defines both the grid cell volume boundaries and the computational nodes, as shown in Figure 6.2, views as a cell-centred scheme. In this figure is also sketched the general 2D cell containing the central node P and four neighboring nodes identified as west, east, south and north nodes (W,E,S,N).

The notation, w,e,s and n are used to refer to the west, east, south and north cell faces, respectivelly. In each control volume, the scalar variable ϕ is defined at the cell centre, i.e. (i, j), whereas the fluxes are defined at the cell boundaries.

Figure 6.2 - A Finite Volume Grid cell and the notation used for a Cartesian 2D structured grid.

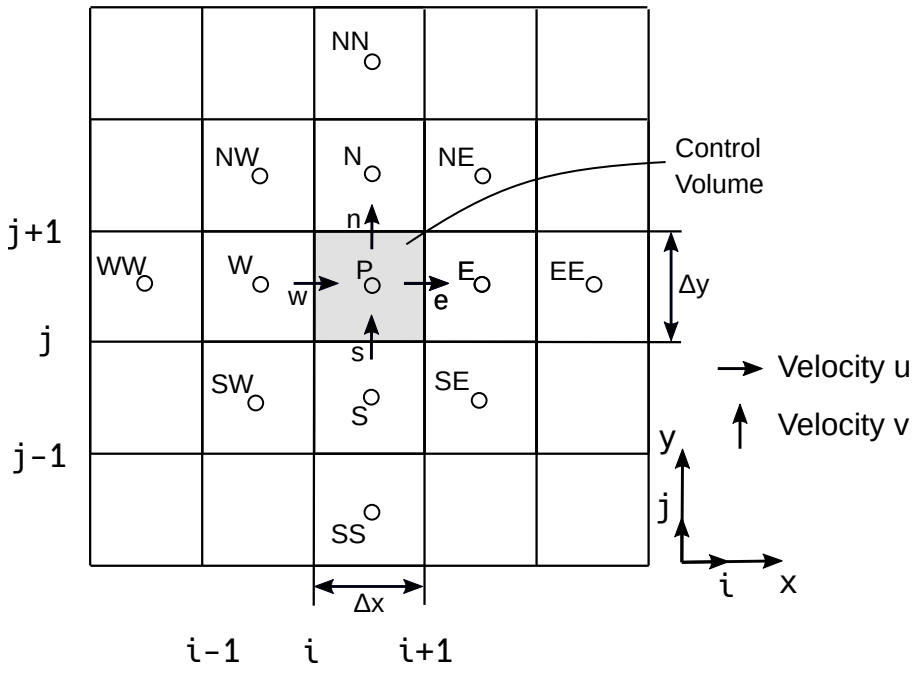

SOURCE: The Author.

The 2D grid cell volume surface is subdivided into four plane surfaces (e, w, n and s), thus the net flux trough the grid cell volume boundary is the sum of integrals over the volume faces, as

$$\int_A f dA = \sum_k \int_{A_k} f dA \tag{6.11}$$

in which f is the component of the convective or diffusive vector in the direction normal to the volume face. The integral in Equation 6.11 is calculated by a integral approximation in terms of the variable values at one location on the grid cell face. These cell face values are approximated by interpolation of the nodal grid cell volume centre values.

The midpoint rule is applied as approximation of the surface integrals. Thus, the surface integral is an approximation of the product of the mean value over the surface an the cell face area. Equation 6.12 shows the surface integral at the south face of the Figure 6.2. Analogous expressions can be derived for all faces by making appropriate index substitutions.

$$F_s = \int_{A_s} f dA = \bar{f} A_e \approx f_e A_e \tag{6.12}$$

The terms in the transport equations that require integration over the the volume of a grid cell, e.g source terms, again the midpoint rule approximations is applied. The mean value is approximated as the value at the grid cell volume centre, thus

$$S_P = \int_{\Omega} s d\Omega = \bar{s} \Delta\Omega \approx s_P \Delta\Omega \tag{6.13}$$

where s_P is the value of s at the grid cell volume centre and since all the variables are available at node P, no interpolation is necessary.

6.4.2 Discretization of diffusive terms

In order to demonstrate the principles of the spatial discretization of diffusive transport terms , it is considereted the steady state diffusion of a property ϕ in a one dimensional domain as sketched in Figure 6.3. In Cartesian coordinates the process is governed by:

$$\frac{d}{dx}\left(\Gamma_\phi \frac{d\phi}{dx}\right) + S_\phi = 0 \tag{6.14}$$

where Γ_ϕ is a diffusion coefficient and S_ϕ a source term.

As shown in Figure 6.3, the west side face of the grid volume is referred to by w and the east side grid volume face by e. The distances between the nodes W and P, and between nodes P and E, are identified by δx_{WP} and δx_{PE}, respectively. By the use of the Gauss theorem and the midpoint formula, it finds

$$\int_{\Delta\Omega} \frac{d}{dx}\left(\Gamma \frac{d\phi}{dx}\right) d\Omega + \int_{\Delta\Omega} S_\phi d\Omega = \left(\Gamma_\phi A \frac{d\phi}{dx}\right)_e - \left(\Gamma_\phi A \frac{d\phi}{dx}\right)_w + \bar{S_\phi} \Delta\Omega \tag{6.15}$$

Figure 6.3 - A Finite Volume Grid cell and the grid spacing notation.

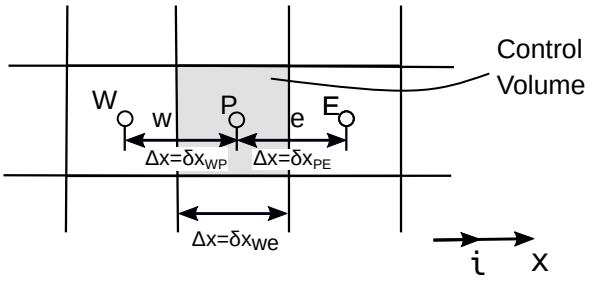

SOURCE: The Author.

where A is the cross section area of the grid cell volume face, $\Delta\Omega$ is the grid cell volume and $\bar{S_\phi}$ is the average value of S_ϕ over the grid cell volume.

The linear profile is used to approximate the variable gradient, thus for the diffusive flux at position e, the approximation is defined as

$$\Gamma_{\phi,e}\left(\frac{\partial\phi}{\partial x}\right)_e \approx \Gamma_{\phi,e}\frac{(\phi_E-\phi_P)}{x_E-x_P} \tag{6.16}$$

The interface e is midway between the grid node points, than the parameter $\Gamma_{\phi,e}$ is approximated as the arithmetic mean of $\Gamma_{\phi,P}$ and $\Gamma_{\phi,E}$.

The final discretized equation can be written on the following algebraic form

$$a_P\phi_P = a_W\phi_W + a_E\phi_E + S_\phi\Delta\Omega \tag{6.17}$$

where the coefficients are

$$a_W = \frac{\Gamma_{\phi,w}}{\delta x_{WP}}A_w \tag{6.18}$$

$$a_E = \frac{\Gamma_{\phi,e}}{\delta x_{PE}}A_e \tag{6.19}$$

$$a_P = a_W + a_E - S_{\phi,p}\Delta\Omega \tag{6.20}$$

6.4.3 Discretization of convective terms: the QUICK scheme

The momentum equations were discretized by the quadratic upstream interpolation for convective kinetics (QUICK) scheme. This high order differencing scheme, presented by Leonard (1979), uses a three-point upstream-weighted quadratic interpolation for cell face values in the convection term. This scheme was selected for its stability, sensitivity to the flow direction, third-order truncation error and effectiveness for steady or quasi-steady flows (FLETCHER, 2012).

Since the classical upwind scheme is only first-order accurate in time and space, researchers have proposed higher order upwind schemes to improve the accuracy of the scheme and to preserve the advantage of the scheme in suppressing numerical oscillations. QUICK is one of such schemes (e.g., Leonard (1979), Hayase et al. (1992)). The scheme is based on the local upwind-weighted quadratic interpolation for the convection term. The scheme is often used to solve the convection-diffusion equation with the employment of second-order central difference for the diffusion term. For the convection term, the scheme is third-order accurate in space, and thus, it is sometimes called third-order upwinding.

Considering the two-dimensional control volume schematised on Figure 6.2, and taking the horizontal direction solely the discretization of the Cartesian one-dimensional Equation 6.10 can be summarised as

$$\frac{\partial(\rho\phi)}{\partial t} + a_P\phi_P = a_W\phi_W + a_E\phi_E + a_{WW}\phi_{WW} + a_{EE}\phi_{EE} + S_M \tag{6.21}$$

with central coefficient

$$a_P = a_W + a_E + a_{WW} + a_{EE} + F_e - F_w \tag{6.22}$$

and neighbour coefficients

$$a_W = D_w + \frac{6}{8}\alpha_w F_w + \frac{1}{8}\alpha_e F_e + \frac{3}{8}(1-\alpha_w)F_w \tag{6.23}$$

$$a_{WW} = -\frac{1}{8}\alpha_w F_w \tag{6.24}$$

$$a_E = D_e - \frac{3}{8}\alpha_e F_e - \frac{6}{8}(1-\alpha_e)F_e - \frac{1}{8}(1-\alpha_w)F_w \tag{6.25}$$

$$a_{EE} = \frac{1}{8}(1-\alpha_e)F_e \tag{6.26}$$

where

$$\alpha_w = 1 \quad for \quad F_w > 0, \quad \alpha_e = 1 \quad for \quad F_e > 0$$
$$\alpha_w = 0 \quad for \quad F_w < 0, \quad \alpha_e = 0 \quad for \quad F_e < 0$$

The variable F represents the convective mass flux per unit area and D the diffusion conductance at cell faces. The term S_M represents the source term of buoyancy and pressure and the cross derivatives of the diffusive terms.

Since the QUICK scheme as presented above may be unstable due to the occurrence of negative principal coefficients, it has been reformulated in different ways that alleviate the stability problems. These formulations all involve placing perturbative negative coefficients in the source term to obtain positive main coefficients. The contributing part is weighted accordingly to obtain better stability and as positive coefficients as possible (VERSTEEG; MALALASEKERA, 2007).

Hayase et al. (1992) rearranged the QUICK scheme and derived a stable and fast converging variant that can be summarised as

$$\frac{\partial(\rho\phi)}{\partial t} + a_P\phi_P = a_W\phi_W + a_E\phi_E + \bar{S} + S_M \tag{6.27}$$

with central coefficient

$$a_P = a_W + a_E + F_e - F_w \tag{6.28}$$

and neighbouring coefficients

$$a_W = D_w + \alpha_w F_w \tag{6.29}$$

$$a_E = D_e - (1 - \alpha_e) F_e \tag{6.30}$$

The source is

$$\begin{aligned} \bar{S} = \frac{1}{8}(3\phi_P - 2\phi_W - \phi_{WW})\alpha_w F_w + \frac{1}{8}(\phi_W - 2\phi_P - 3\phi_E)\alpha_e F_e \\ + \frac{1}{8}(3\phi_W - 2\phi_P - \phi_E)(1 - \alpha_w)F_w + \frac{1}{8}(2\phi_E - \phi_{EE} - 3\phi_P)(1 - \alpha_e)F_e \end{aligned} \tag{6.31}$$

where

$$\alpha_w = 1 \quad for \quad F_w > 0, \quad \alpha_e = 1 \quad for \quad F_e > 0$$

$$\alpha_w = 0 \quad for \quad F_w < 0, \quad \alpha_e = 0 \quad for \quad F_e < 0$$

The advantage of this approach is that the main coefficients are positive and satisfy the requirements of conservativeness, boundedness and transportiveness. The assignment of the part of the discretization containing negative coefficients to the source term is called deferred correction and is based on the fact that the scheme is applied as part of an iterative loop structure. At the νth iteration, the source term is evaluated with the values known at the end of the previous $(\nu - 1)$th iteration, i.e. the "correction" of the main coefficients is "deferred" by one iteration.

6.4.4 Numerical grid

To avoid possible pressure oscillations, a uniformly structured backward staggered grid was used in which the pressure p is located at the cell centres, the horizontal velocity u is located at the midpoints of the vertical cell edges, and the vertical velocity v is located at the midpoints of the horizontal cell edges, as shown in Figure 6.4. Consequently, not all extreme grid points lie on the boundaries of the domain. The vertical boundaries, for instance, carry no v-values, just as the horizontal boundaries carry no u-values. For this reason, an extra boundary strip of grid cells is introduced, so that the boundary conditions may be applied by averaging the nearest grid points on either side.

There is no need to prescribe boundary conditions for the pressure, thanks to the recourse of the fully staggered grid, as shown in Figure 6.4.

Figure 6.4 - Sketch of the fully staggered mesh used for the space discretization.

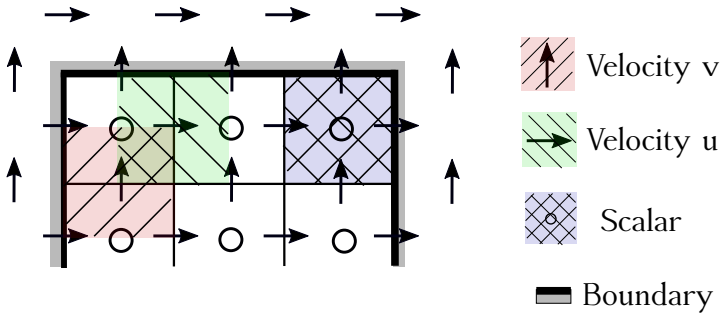

SOURCE: The Author.

The non-uniform structured grid is refined (hyperbolic tangent distribution), on a case by case basis, in zones where high gradients are expected.

For the one-dimensional stretching function, the normalised independent variable is defined as

$$\eta^* = \frac{\eta - \eta_A}{\eta_E - \eta_A} \tag{6.32}$$

so that $0 \leq \eta^* \leq 1$ as $\eta_A \leq \eta \leq \eta_E$.

The stretching function applied is due to Roberts (1971), and modified by Eiseman (1979), is

$$s = P\eta^* + (1 - P)\left(1 - \frac{tanh[Q(1 - \eta^*)]}{tanhQ}\right) \tag{6.33}$$

where P and Q are parameters to provide grid point control. P effectively provides the slope of the distribution, $s \approx P\eta^*$, close to $\eta^* = 0$. Q is a damping factor and controls the departure from the linear s versus η^* behaviour.

Once s is obtained it is used to specify the distribution of x and y, then defining

$$\frac{x - x_A}{x_A - x_E} = f(s), \quad \frac{y - y_A}{y_A - y_E} = g(s), \tag{6.34}$$

generates $x(s)$ and $y(s)$ directly. A simple choice is $f(s) = g(s) = s$, so that Equations 6.34 gives

$$x = x_A + s(x_A - x_E), \quad y = y_A + s(y_A - y_E) \tag{6.35}$$

7 VERIFICATION OF THE NUMERICAL METHOD

7.1 The oscillating plate (Stokes' second problem)

The flow motion over an infinite flat plate that oscillates parallel to itself is investigated. The coordinate system is 2D Cartesian, where x is the coordinate along the plate and y is the coordinate normal to it. The plate oscillates in the $y = 0$ plane with a velocity given by:

$$\hat{y} = 0: \quad \hat{u}_{\text{plate}}\left(0, \hat{t}\right) = \hat{u}_{\max} \cos\left(2\pi \hat{f}\, \hat{t}\right) \tag{7.1}$$

$\hat{f}$ designates the plate oscillation frequency and $\hat{t}$ the time. The fluid is air and the reference kinematic viscosity is taken at ambient temperature e.g. $\hat{\nu}_{\text{ref}} = 1.55 \times 10^{-4} m^2/s$. The maximum plate velocity is taken as the reference velocity e.g. $\hat{u}_{\max} \equiv \hat{u}_{\text{ref}} = 2{\times}10^{-2} m/s$ and the reference length is chosen equal to eight times the depth of penetration of the viscous wave is defined by $L_{\text{ref}} = 8 \times 6.25 \times 10^{-3} m = 5 \times 10^{-2} m$. Thus, the Reynolds number is such that $Re = 64$. The fluid velocity is given by (SCHLICHTING; GERSTEN, 2016):

$$\hat{u}_{\text{fluid}}\left(y, t\right) = \hat{u}_{\max} e^{-\hat{k}\hat{y}} \cos\left(2\pi \hat{f}\, \hat{t} - \hat{k}\hat{y}\right) \tag{7.2}$$

where $\hat{k} = \sqrt{\pi \hat{f} Re}$. The global error at time level n will be denoted by $\mathbf{E^n}{=}\mathbb{Q}^{\mathbf{n}}{-}\xi^{\mathbf{n}}$, where $\mathbb{Q}_{i,j}$ is the computed value at each point of the grid and $\xi_{i,j}$ represents the exact value.

To quantify the error, the commonly used p-norm is chosen in order to estimate the error at a given physical time level n, namely:

$$\left\|\mathbf{E^n}\right\|_p = \left((\Delta t, \Delta y) \sum_{i=1,\ j=1}^{i=imax,\ j=jmax} |{E^n}_{i,j}|^p \right)^{1/p} \tag{7.3}$$

Let's assume the method has an order of accuracy s, then the error is expected to behave like $\left\|\mathbf{E^n}\right\|_p = C\left(\Delta t, \Delta y\right)^s +$ high-order-terms, as the time step or grid spacing are decreased and $(\Delta t, \Delta y) \to 0$.

Figure 3 shows the results of the mesh refinement influence study for the Stokes'

second problem using the p-norm with $p = 1$. The exact and computed solutions are compared on a sequence of time steps and grid spacing, and the norm of the error is plotted as a function ofΔt and Δy. These are shown on a log-log scale, e.g. $\log \|\mathbf{E^n}\|_1 \approx log\,|C| + s \log |(\Delta t, \Delta y)|$ so that a linear behaviour is expected in this plot, with the slope providing the effective order of accuracy s. When decreasing Δt, the mesh refinement is adapted in order to keep constant the Courant–Friedrichs–Lewy number at the value $\mathrm{CFL}_t = 0.5$.

Figure 7.1 - (a) velocity profile for one snapshot and (b) spatial order of accuracy.

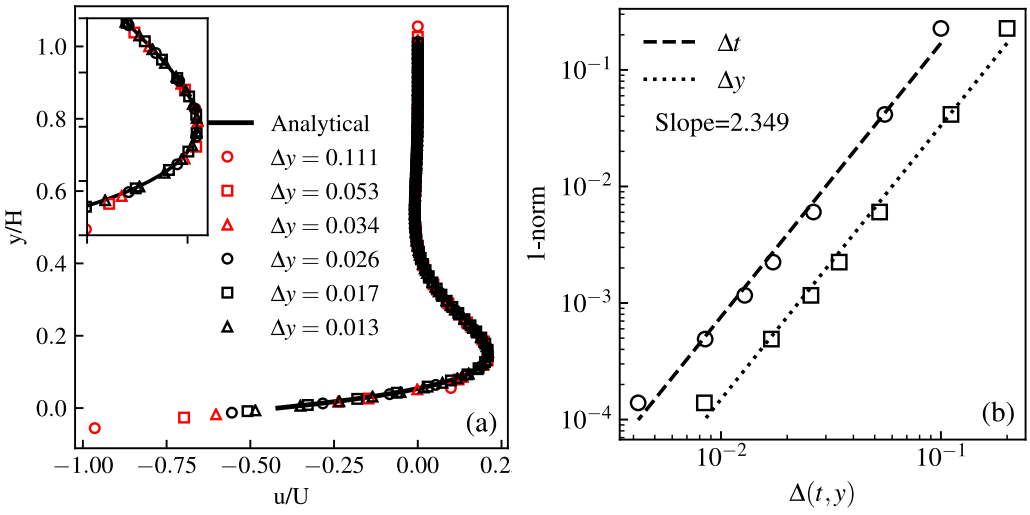

SOURCE: The Author.

7.2 General Couette flow

The so-called Couette flow is a flow between two parallel flat walls, which one is at rest and the other moving in its own plane with a velocity U, as shown in Figure 7.2. The size in the z direction is very large compared with their separation distance h.

The flow between these walls is taken to be in the x direction, and since there is no flow in the y direction, the pressure will be a function of x only. Using the fact that $u = u(y)$ only and $v = w = 0$ together with the fact that $p = p(x)$ only, and with the boundary conditions $u(0) = 0$ and $u(h) = U$, using the Equation 4.11, the velocity is

Figure 7.2 - General Couette flow.

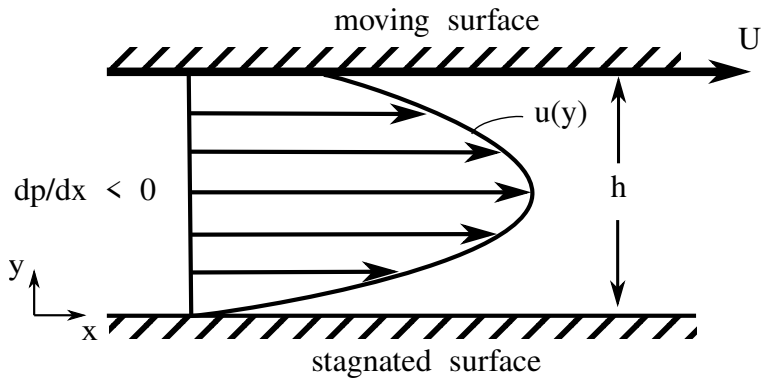

SOURCE: The Author.

$$u(y) = \frac{y}{h}U - \frac{h^2 Re}{2}\frac{dp}{dx}\frac{y}{h}\left(1 - \frac{y}{h}\right) \tag{7.4}$$

In the case selected the fluid is air with $\hat{\nu} = 1.55 \times 10^{-5} m^2/s$, the characteristic lenght $\hat{h} = \hat{L}_c = 5cm$ and the characteristic velocity $\hat{V}_c = 1cm/s$, resulting in $Re = 32$. The top wall velocity is $U = 1$ and the pressure gradient is $dp/dx = -1$.

Figure 7.3 shows the comparison between the numerical results and the analytical solution from Equation 7.4. It is seen that the pressure gradient ($dp/dx < 0$) assists the viscously induced motion to overcome the shear force at the lower surface and the numerical results agrees well with the analytical solution.

7.3 Plane Poiseuille flow

The steady flow of a viscous fluid in a channel with two parallel stagnated flat walls, as shown in Figure 7.4, is referred to as Poiseuille flow.

Since $\partial p/\partial y = 0$, the pressure gradient in the direction of flow is constant, then $dp/dx = const$. Let the distance between the walls be denoted by h, and the boundary conditions $u(y) = 0$ for $y = -h/2$ and $h/2$. Solving Equation 4.11, the velocity can be written as

$$u(y) = -\frac{Re}{2}\frac{dp}{dx}\left[\left(\frac{h}{2}\right)^2 - y^2\right] \tag{7.5}$$

Figure 7.3 - Comparison of velocity profile for the Couette flow.

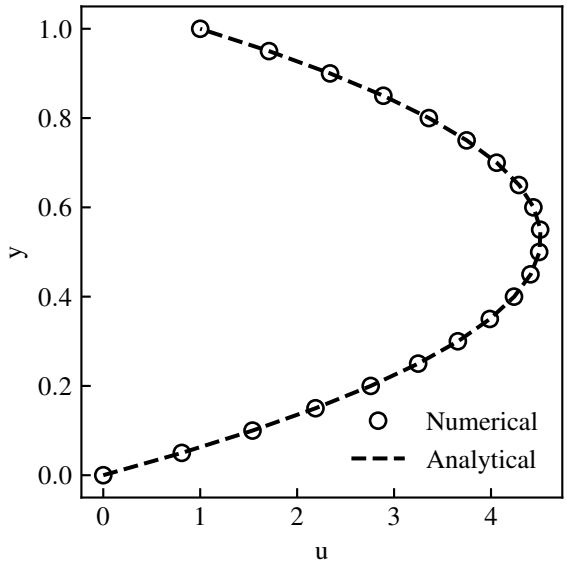

SOURCE: The Author.

Figure 7.4 - Parallel flow with parabolic velocity distribution.

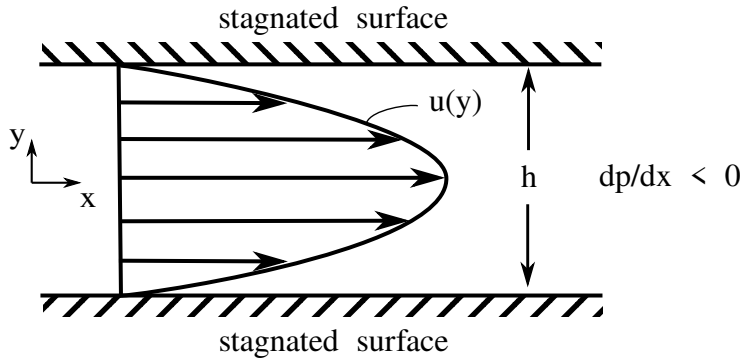

SOURCE: The Author.

The flow depends upon the external pressure for its existence, and the resultant velocity profile is parabolic. The case selected for this verification study is the same of the general Couette flow in the last subsection, therefore, $Re = 32$ and $dp/dx = -1$. Figure 7.5 shows a good agreement between the numerical and the analytical solution provided by Equation 7.5.

Figure 7.5 - Comparison of velocity profile for the Poiseuille flow.

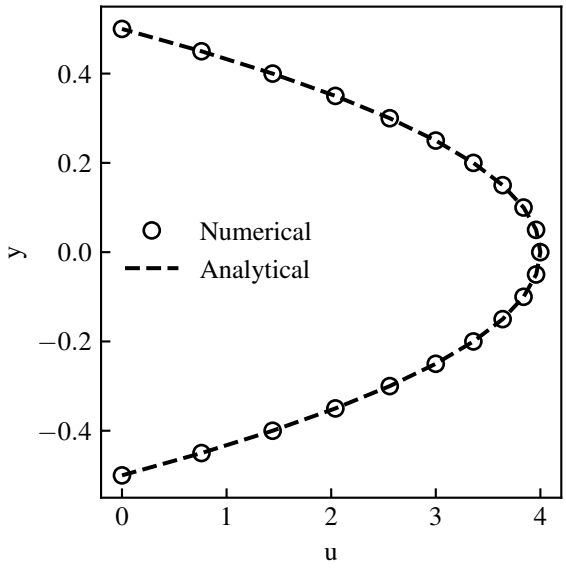

SOURCE: The Author.

8 VALIDATION OF THE NUMERICAL METHOD

A set of validation cases was gattered to show the full abillity of the present numerical code to describe many applications. Table 8.1 shows the validation cases selected and their charactristics. The comparison of the results obtained are shown in the next sections.

Table 8.1 - Set of numerical validation test cases.

Case	Temporal	Reaction
Lid-driven Cavity	Steady	Non-reactive
Enclosure with a Heated Cylinder	Steady	Non-reactive
Excentric Flow Past a Circular Cylinder	Unsteady	Non-reactive
Confined Tsuji Flame	Steady	Reactive
Coflow Diffusion Flame	Steady/Unsteady	Reactive

8.1 Lid-driven cavity

The first validation problem is the classical lid-driven cavity. A laminar incompressible flow in a isotherm square cavity whose top wall moves with a uniform velocity in its own plane. The case configuration is depicted in the Figure 8.1. The cavity has equal sides lenght of $\hat{L} = \hat{L}_c = 1.55 \times 10^{-2} m$ and the top wall velocity is $\hat{U} = \hat{v}_c = 0.1 m/s$. The case selected here corresponds to $Re = 100$ and $Pe = 70.4$.

Figure 8.1 - Lid driven cavity configuration.

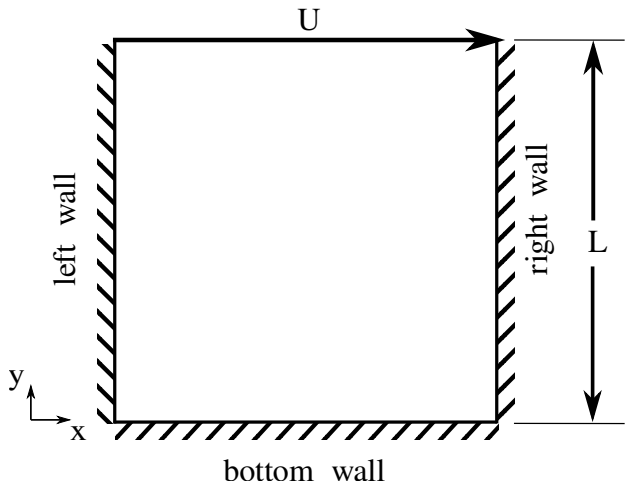

SOURCE: The Author.

The streamlines patterns for the lid-driven cavity flow configuration with a 61×61 grid is shown in Figure 8.2. Although a comparison is not shown here, the presence of the secondary vortices in the present results, as reported by the literature for $Re = 100$, shows the agreement of the results and that the grid is adequate for this value of Re.

Figure 8.2 - Streamlines of the lid-driven Cavity case with 61×61 grid.

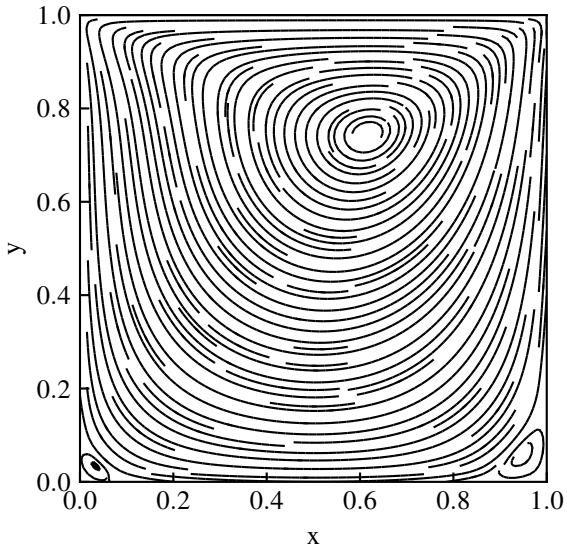

SOURCE: The Author.

The lid-driven cavity was explored experimentally by Nallasamy and Prasad (1977) and numerically by Ghia et al. (1982). Figure 8.3a and 8.3b show the velocity profiles for u along vertical lines and Fig 8.3c and 8.3d for v along horizontal lines, both passing through the geometric centre of the cavity. Figure 8.3 also shows the available results from literature (NALLASAMY; PRASAD, 1977; GHIA et al., 1982). For the case selected of $Re = 100$, all the present results agree well with the experimental and numerical results. With the exception of the coarser case, that presents a bit of discrepancies for the vertical velocity pic, as shown in Figure 8.3c. Even though, with a little refinement of plus 40 points, the preset code was able to reproduce the literature results. The present results demanded around half the number of the points in the mesh to represent the experimental results, when compared with the computations of Ghia et al. (1982). It is important to notice that this coarse meshes could gradually become inadequate as Re increases.

Figure 8.3 - Lid driven cavity comparison for different mesh sizes and $Re = 100$. The '$\circ$' marker corresponds to the present code numerical results, the dashed line represents the numerical results of Ghia et al. (1982) with mesh (129×129) and the '$\times$' marker the experimental results of Nallasamy and Prasad (1977).

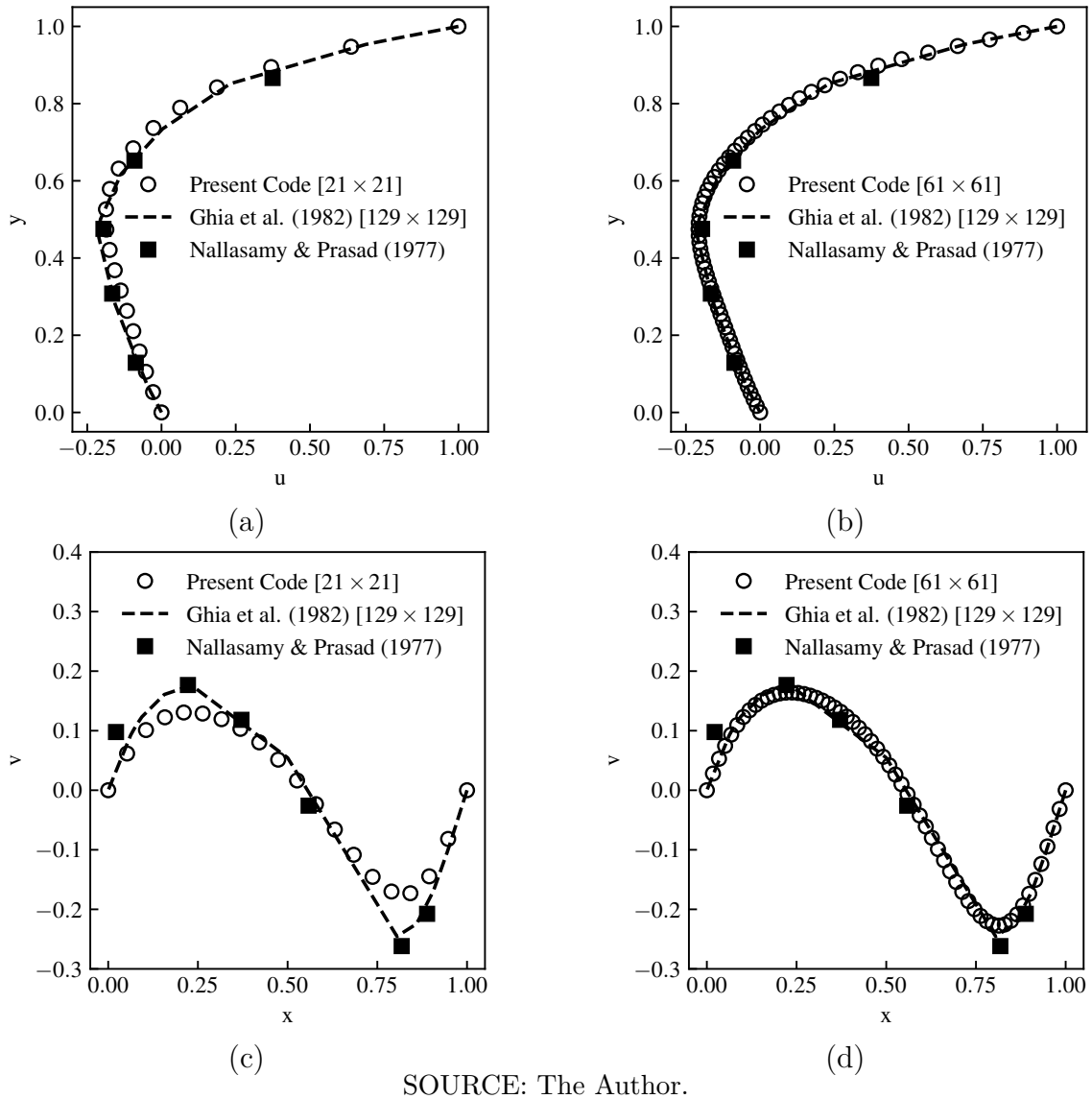

SOURCE: The Author.

8.2 Square enclosure with a heated circular cylinder

This case consists of a cooled square enclosure kept at a constant temperature T_c, with sides of length L, within which a heated circular cylinder at constant temperature T_h, with a radius $R(= 0.2L)$, is located in the centre of the enclosure. This configuration was studied by Kim et al. (2008) to examine the natural convection phenomena by changing the location of the circular cylinder. The case selected

here corresponds to $Fr = 0.2$, $Re = 6.7$ and $Pe = 4.9$. This case corresponds to $Ra = 10^3$, where Ra is the Rayleigh number defined as $Ra = (g\Delta T L^3)/(\nu\alpha)$ and $\Delta T = 2(T_h - T_c)/(T_h + T_c)$. The hot cylinder and cold wall temperatures are $T_h = 1200K$ and $T_c = 300K$, respectively.

Figure 8.4 - Lid driven cavity configuration.

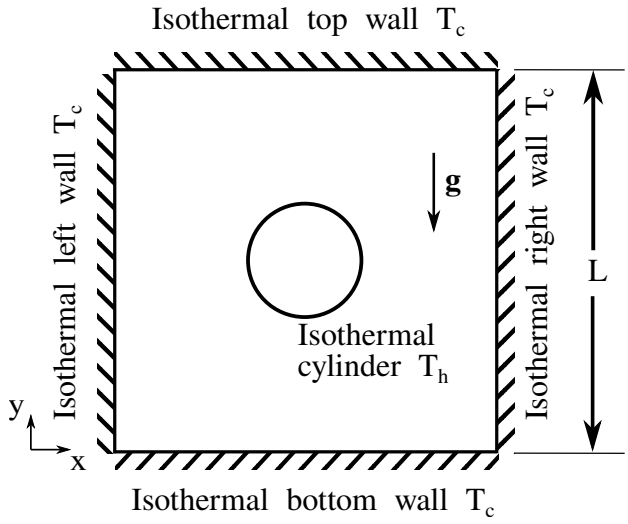

SOURCE: The Author.

Once the velocity and temperature fields are obtained, the local, surface-averaged, time-averaged, and time-and-surface-averaged Nusselt numbers are defined as

$$Nu = \left.\frac{\partial\theta}{\partial n}\right|_{wall}, \qquad \overline{Nu} = \frac{1}{K}\int_0^K Nu\, dS \tag{8.1}$$

where $\theta = (T - T_c)/(T_h - T_c)$, n is the normal direction with respect to the walls, K is the surface area of walls. The Nusselt numbers results presented by Kim et al. (2008) were used to evaluate the applicability of the present solution approach.

Figure 8.5 shows the streamlines and comparison of the distribution of local Nusselt numbers along the cold walls of the enclosure at $Ra = 10^3$. Because the problem presented symmetry about the vertical centre line at $x = 0$, only the right half of the enclosure is shown.

The surface-averaged Nusselt number defined by the Equation 8.1 is evaluated at

the top wall, $\overline{Nu}_T$, the present approach obtained $\overline{Nu}_T = 1.73$, while from Kim et al. (2008) the value obtained is 1.67, difference of 3.59%.

Figure 8.5 - Streamlines (a) and Local Nusselt number distribution along the walls of the enclosure (b). Grid resolution of 201 x 201 for Kim et al. (2008) and 101 x 101 for the present study.

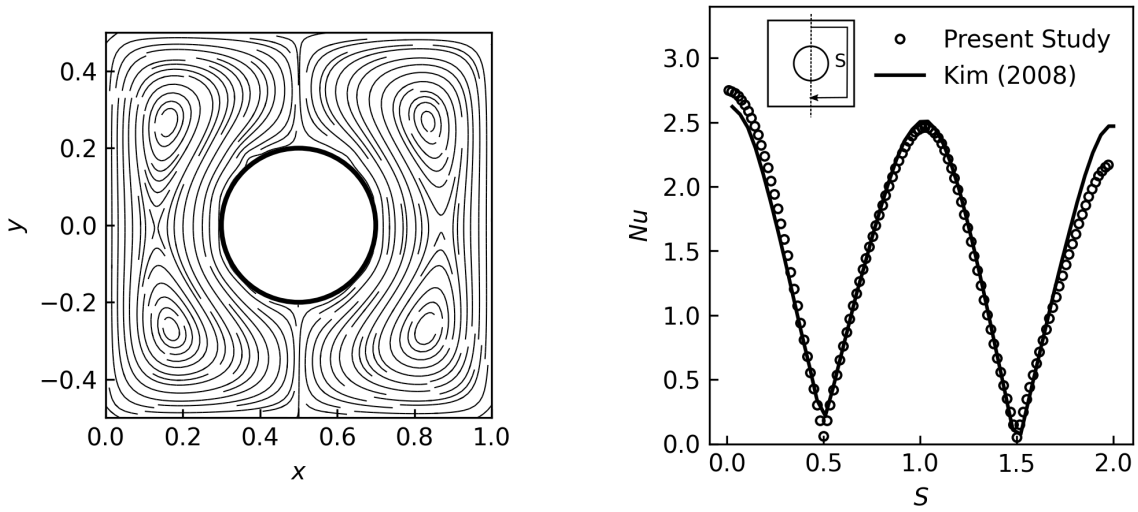

(a) (b)

SOURCE: The Author.

8.3 Unsteady wake of a flow past a circular cylinder

The incompressible unsteady laminar flow around a cylinder with a circular cross section of diameter $d = L_c$ placed eccentrically in a channel of height $h = 4.1d$ is considered (see Figure 8.6). The coordinate system is 2D Cartesian, with y being the streamwise coordinate and x the coordinate normal to the channel walls. This configuration corresponds to one of those used by Schäfer et al. (1996) for a benchmark of different solution approaches for solving the incompressible Navier-Stokes equations. The distances between the cylinder centre and the bottom and top walls are $2.1d$ and $2d$, respectively. The Reynolds number is defined by $Re = v_{bulk}d/\nu_{air}$, where $\nu_{air} \equiv \nu_c$ is the kinematic viscosity and $v_{bulk} \equiv v_c$ denotes the bulk velocity. The case selected here corresponds to $Re = 100$. As illustrated in Figure 8.6, the governing equations are integrated with the following boundary conditions: on the top ($x = x/d = 2.1$) and bottom ($x = x/d = 2$) walls and at the cylinder surface ($r^2 = x^2 + y^2$) the no-slip condition is imposed for velocities. At the inlet section located at ($y = y/d = 4$), a parabolic profile is prescribed for the velocity streamwise

component (with a maximum value $v(x = h/2) = v_{max} = 3v_{bulk}$) and the normal component is set to 0.

Figure 8.6 - Unsteady cylinder wake: flow configuration and related boundary conditions.

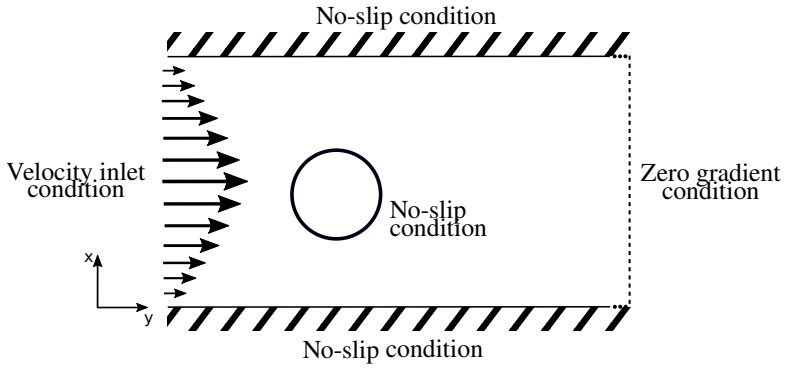

SOURCE: The Author.

Among all the characteristics of this type of problem (lift, drag, and pressure coefficients), the correct prediction of the periodic vortex-shedding, illustrated by the isocontour of velocity in Figure 8.7c was the target chosen to validate the present solution approach. In particular, the Strouhal number is computed to measure the ability of the method to produce quantitatively accurate unsteady results. Figure 8.7a presents the time evolution of the non-dimensional normal component of the velocity at $(x, y) = (0.5, 0.5)$ observed when the periodic regime of shedding is established. For $Re = 100$, the experimentally obtained Strouhal number is $St = 0.287 \pm 0.003$ (SCHÄFER et al., 1996). The power spectrum of the fluctuations of the streamwise component of the computed velocity is shown in Figure 5b. The numerically obtained Strouhal number value is $St = 0.289$ which agrees well (relative error of 1.35%) with its experimentally obtained counterpart.

For the present case, Figure 8.8 shows, for a given physical time-step, an evolution of the maxima of the residuals $Res(v)_{i,j}$ (Equation 6.8) during the artificial-time iteration cycle. It can be seen that calculations for $\beta = 40$ become unstable and within 40 steps starts to diverge, whereas other cases converge to a stable solution. For low values of β, it takes only 10 iterations for the solution to reach almost constant residual values but then, further iterations do not improve the solution and so the accuracy constraint cannot be met.

Figure 8.7 - Unsteady cylinder wake (Mesh size of 43×246): (a) Velocity history signal at $(x, y) = (0.5, 0.5)$, (b) Corresponding power spectrum of such velocity signal, and (c) Snapshot of the contour of the velocity norm (The marker $\times$ indicates the location at which the data in (a) are recorded).

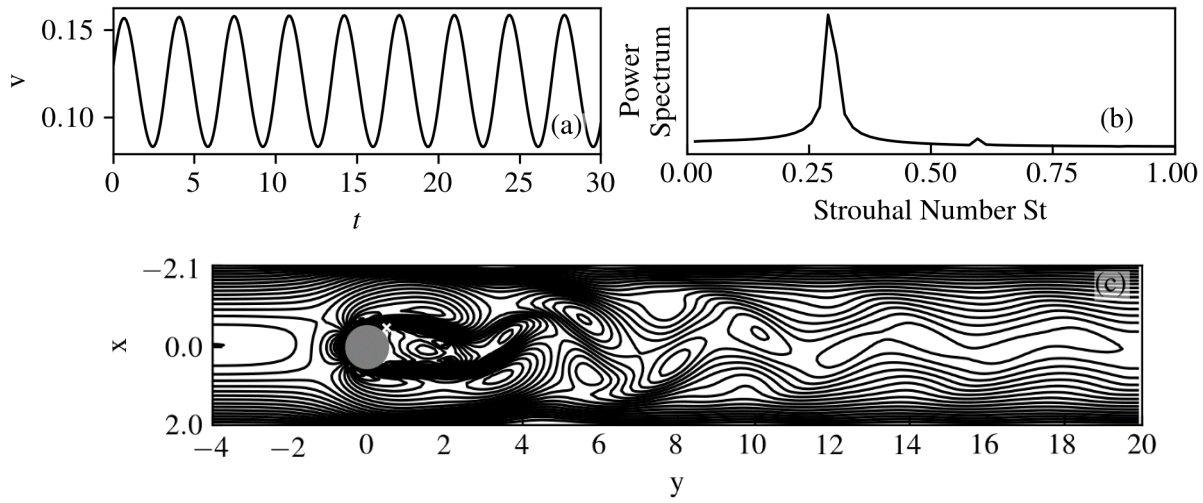

SOURCE: The Author.

Figure 8.8 - Unsteady cylinder wake (Mesh size of 43×246): (a) Convergence history as a function of the dimensionless artificial compressibility factor β.

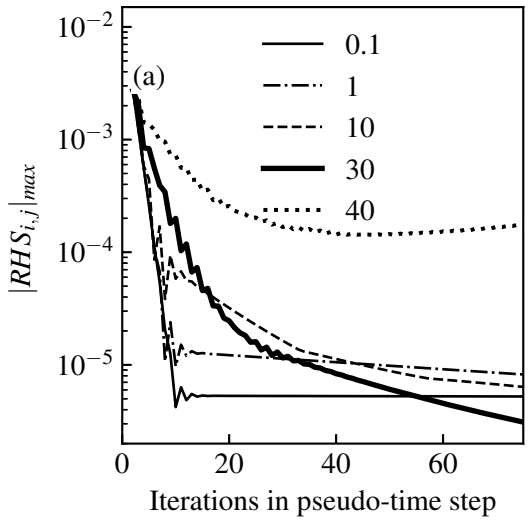

SOURCE: The Author.

The effect of the artificial compressibility factor β on the number of artificial-time steps necessary to achieve convergence to the physical time step following that corresponding to the snapshot of Figure 8.7c is illustrated in Figure 8.9. L is defined as the channel length and $\Delta\tau = 0.14$. The optimum value of $\beta_{opt} \approx 34$ is higher than the expected value of $\beta_{opt} \approx 8$ reported in the literature (BRUEL et al., 1996; SHAPIRO; DRIKAKIS, 2005). By using Equation 6.5, the dashed line in Figure 8.9 represents the number of minimum time-steps to achieve convergence of the artificial-time integration for each value of β. Considering the convergence criteria of $Res(v)_{max} < \varepsilon$, it is possible to see a good agreement between the computation iterations and the iterations described by Equation 6.5 until β_{opt}. For $\beta > \beta_{opt}$, the convergence rate begins to degrade gradually until $\beta \approx 38$, above which convergence is lost.

Figure 8.9 - Unsteady cylinder wake (Mesh size of 43×246): influence of the dimensionless artificial compressibility factor β on the number of time steps required to obtain an artificial-time converged solution. Comparison with the lower bound proposed by Chang and Kwak (1984).

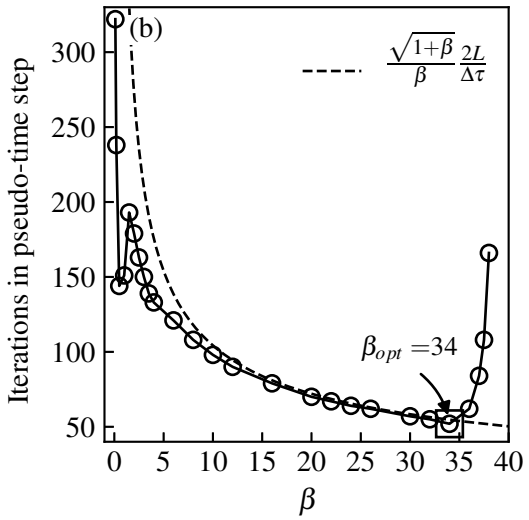

SOURCE: The Author.

8.4 Steady Tsuji flame

This configuration is concerned with the flame stabilization over a porous cylindrical burner with radius $\hat{r} \equiv \hat{L}_{\text{ref}}$ inside a channel. The geometry is 2D Cartesian. As shown in Figure 8.10, the gaseous fuel is injected from the forward half part of the burner with velocity $\hat{u}_b \equiv \hat{u}_{\text{ref}}$ into the incoming airflow of velocity $\hat{u}_{\text{air}}$.

Figure 8.10 - Tsuji diffusion flame: flow configuration and boundary conditions.

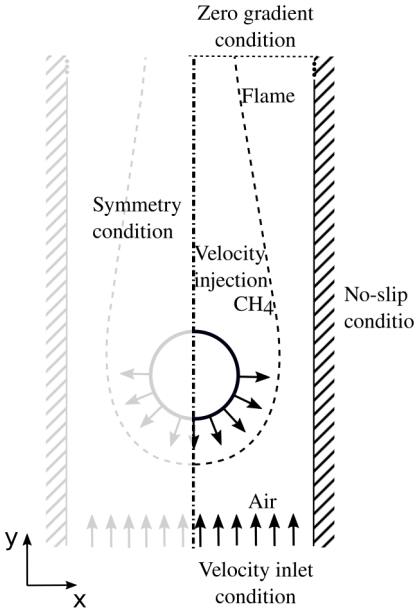

SOURCE: The Author.

This configuration reproduces the experimental set-up of the Tsuji Burner, where the rear side of the burner surface was coated to avoid the ejection of fuel into the wake region (TSUJI; YAMAOKA, 1967). In such a configuration characterized by a low incoming flow velocity, an envelope steady flame is found. The flame is described by the set of Equations 4.10-4.12 and 5.5-5.7 where the other reference quantities are chosen as $\hat{Y}_{F_c} \equiv \hat{Y}_{F_b}$, $\hat{Y}_{O_{2c}} \equiv \hat{Y}_{O_{2\infty}}$, $\hat{c}_{p_{\text{ref}}} \equiv \hat{c}_{p_\infty}$, $\hat{T}_{\text{ref}} \equiv \hat{T}_\infty$ and $\hat{\rho}_{\text{ref}} \equiv \hat{\rho}_\infty$ where the index b and ∞ denote quantities taken at the burner exit and in the ambient atmosphere, respectively.

Equations 4.10 to 4.12 and 5.5 to 5.7 are integrated with the following boundary conditions: On the symmetry axis ($x = 0$), $\partial_x u = \partial_x v = \partial_x Z = \partial_x H = 0$; at the burner boundary surface ($r^2|^+ = x^2 + y^2 = 1^+$), $u - x = v - y = 0$, $Z_s - Pe^{-1}\partial_n Z = S_Z$, $H_s - Pe^{-1}\partial_n H = S_H$ (Robin's like boundary type for Z and H) where $Z_s \equiv S\ Y_{F_s} - 1$, $H_s \equiv (S+1)\ T_s/Q + Y_{F_s}$ and the subscript n stands for the normal to the burner surface. The terms S_Z and S_H are the Z and H fluxes which are imposed at the burner injection surface $r^2|^- = x^2 + y^2 = 1^-$ as function of $\hat{Y}_{F_b}$, $\hat{T}_b$ and $\hat{u}_b$, namely $S_Z \equiv S + 1$ and $S_H \equiv (S+1)\ T_b/Q + 1$. Note that Y_{F_s} and T_s are found as part of the solution of the problem and this holds only in the forward part of the cylinder. The boundary conditions at the inlet ($y = -7.5$) are $v = 1$, $u = Z = 0$ and

$H = (S+1)\ T_\infty/Q+1$. At the outlet ($y = 13$), they are $\partial_y u = \partial_y v = \partial_y Z = \partial_y H = 0$ and at the channel wall ($x = 4$), they read $u = v = \partial_x Z = \partial_x H = 0$. According to the definition of the mixture fraction function Z, the flame position (x_f, y_f) is given by the isoline $Z(x, y) = 1$ where the flame temperature T_f is determined by $H(x_f, y_f) = (S + 1)\ T_f/Q$.

The steady diffusion flame results are presented in Figure 8.11 for different values of fuel-ejection rate $-$fw and $\hat{u}_{\text{air}}$, in which $-fw = (\hat{u}_b/\hat{u}_{\text{air}})\,(\text{Re}/2)^{0.5}$. This figure depicts the temperature profile along the forward stagnation streamline. Figure 8.11 compares the predictions obtained in this study to the numerical finite-rate chemistry and experimental results of Tsa and Chen (2003) and Dreier et al. (1986), respectively.

Figure 8.11 - Tsuji diffusion flame (Mesh size of 82 × 446): Temperature distribution through the flame front of a Tsuji burner with $Re = 38$, $Fr = 2.6$, $\hat{r} = 0.02m$, $\hat{u}_{\text{air}} = 1.15m/s$, *and* $-fw = 0.318$. The continuous line and its corresponding circles are the numerical result of the current study, the dashed line and its corresponding squares are the numerical results of Tsa and Chen (2003) and the dash-dot line and its corresponding triangles are the experimental measurements of Dreier et al. (1986).

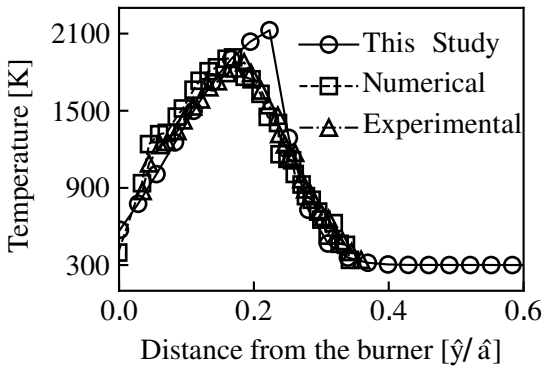

SOURCE: The Author.

The presented infinite-reaction-rate combustion model reproduces the data measured in both numerical and experimental studies, except in a small, but important, region around the maximum temperature. The profiles show that, for this study, the maximum temperature is approximately 2200 K (adiabatic flame temperature for methane) with a sharp temperature profile, while it is about 1900 K in the experimental study with a rounded distribution. This is due to the limitation of

infinite-rate chemistry to describe the coexistence of reactants in the reaction layer that is approximated as a flame-sheet, i.e., the reactants must reach the flame in stoichiometric proportions.

Figure 8.12 directly compares the flame-sheet obtained in this study with the flame boundary computed from fuel reaction-rate contours by Tsa and Chen (2003) represented as the dashed -line. The flame-sheet shape obtained (solid-line) is similar to that given by the reaction-rate contours of the finite-rate computation, except in the wake distant from the cylindrical burner, at which the recirculation zone is affected by the thermal expansion.

Figure 8.12 - Tsuji diffusion flame (Mesh size of 82×446): streamlines and flame shape with $Re = 18$, $Fr = 1.95$, $\hat{r} = 0.015m$, $\hat{u}_{\text{air}} = 0.75\,m/s$, and $-fw = 0.5$.

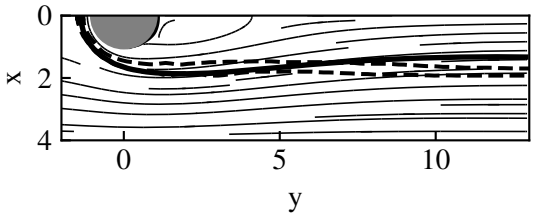

SOURCE: The Author.

8.5 Coflow diffusion flame

The unconfined flickering jet diffusion flame case was chosen to validate the full transient implementation of the present numerical code. The geometry of this case is 2D axisymmetric. As shown in Figure 8.13, the burner is composed by a fuel jet with a radius $\hat{L}_c \equiv \hat{r}_F = 1.3 \times 10^{-2} m$ surrounded by a annular air stream with radius $\hat{r}_{air} = 13 \times 10^{-2} m$. The fuel is methane diluted by 50%, $Y_{F_c} \equiv Y_{F_b} = 0.5$. The fuel and air burner inlet velocities are $\hat{v}_F = 10 \times 10^{-2} m/s$ and $\hat{v}_c \equiv v_{air} = 15 \times 10^{-2} m/s$, respectively. The resulted Reynolds number, Péclet number and Froude number for this case are $Re = 122$, $Pe = 86$, and $Fr = 0.42$. Also, the Figure 8.13 shows the following boundary conditions: on the top ($y = \hat{y}/\hat{r} = 40$) and right ($x = \hat{x}/\hat{r} = 10$) boundaries, free-slip condition is imposed for velocities along with zero fluxes for the temperature, mixture fraction and excess enthalpy. At the inlet section located at ($y = \hat{y}/\hat{r} = 0$), a prescribed velocity streamwise component for fuel and air, $v(x \leq 1) = \hat{v}_F/\hat{v}_c = 0.66$ and $v(x < 1) = v_a ir/v_c = 1$, respectively. The mesh dependency tests showed no significant differences in the large-

scale flame features, such as flicker frequency and points of fuel pocket detachment. The Courant–Friedrichs–Lewy condition was the base reference for the choice of the numerical parameters. For the present case, the CFL numbers for the physical and artificial-time integration, were chosen as $CFL_t = 0.27$ and $CFL_\tau = 0.2$, respectively. Another key parameter of choice was the ability of the physical time-step to describe sufficiently well one cycle of flame flickering.

Figure 8.13 - Flickering diffusion flame: flow configuration and boundary conditions.

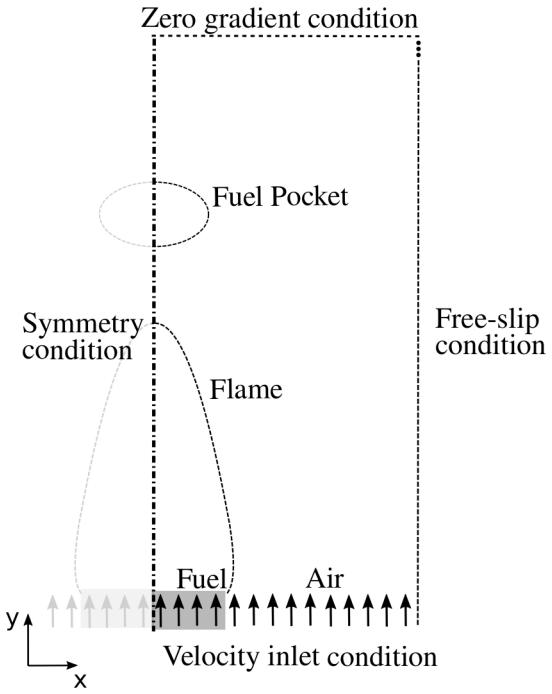

SOURCE: The Author.

The resulting times steps were $\Delta\hat{t} = 4.3\times10^3 s$ and $\Delta\hat{\tau} = 3.9\times10^4 s$, for physical and artificial times, respectively. The value of $\beta = 8$ led to a suitable convergence rate for this set of time steps. The case introduced above reproduces the computations done by Davis et al. (1994) who also used the flame sheet model, unit Lewis number hypothesis, and validated their results against the experimental data by Chen et al. (1988). One strong motivation behind the choice of this case was to assess the ability of the present code to describe the temporal behavior and the formation of vortical structures due to large density gradients and buoyancy effects. The low frequencies of flame oscillations (flame flickering) were in the range 5 Hz 15 Hz and independent of the fuel type, the geometry of the source of fuel and the flow field in the wake

(TOONG et al., 1965). The coupling within the flow field between the accelerations around the flame and decelerations in the plume above it due to the buoyant force dramatically impacts the temperature and species field dynamics and is at the origin of the formation of large vortices outside of the flame. As a vortex ascends along the flame in direction of the tip, it is forced against the flame. Close to the flame tip, the vortex strangles the flame, a bottleneck appears featuring a large strain rate which leads to the local extinction of the flame ending up in the separation of part of the flame tip (fuel pockets) which is carried away by the flow (CHEN et al., 1988). The frequency analysis of this behaviour of the flickering jet diffusion flame is shown in Figure 8.14.

Figure 8.14 - Flickering diffusion flame (Mesh size of 41 × 101): (a) Mixture Fraction history at $(x, y) = (1.3 \times 10^2 m, 10^1 m)$, (b) power spectrum for the flame fluctuation.

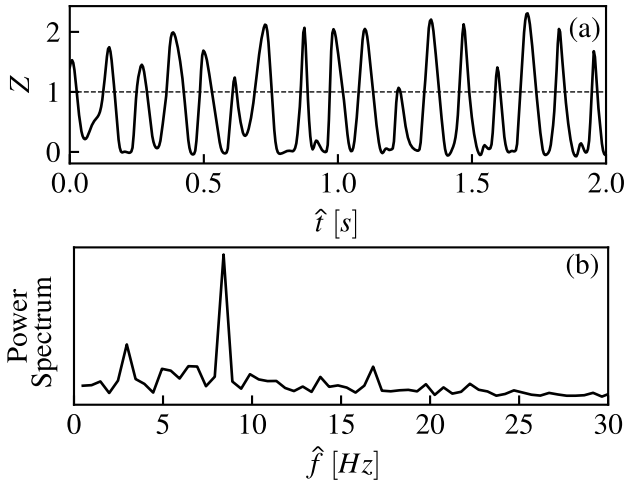

SOURCE: The Author.

The mixture fraction history was chosen to represent the flame fluctuations at $(\hat{x}, \hat{y}) = (1.3 \times 10^2 m, 10^1 m)$, as shown in Figure 8.14a. The dashed line represents the stoichiometric value, thus, when the continuous line crosses this line, it means that the detachment of a hot pocket of fuel occurred. The power spectrum derived from the flame fluctuations are presented in Figure 8.14b. The numerically computed predominant frequency at the probe location of $St/\hat{t}_c = 8.4Hz$ agrees well (relative error of 5.5%) with the value predicted by the correlation $\hat{f} - Fr = \hat{t}_c 0.29 Fr^{-1} = 7.96Hz$, suggested by Sato et al. (2000). Since the large-scale instability is produced mainly by buoyancy, its frequency is an increasing function of the buoyancy strength as

observed when plotting the Strouhal number as a function of the Froude number. The weaker secondary frequency peak visible in Figure 8.14b probably results from the preceding flame bulge interaction with the trailing one and is categorized here as a sub-harmonic. The flame evolution between $\hat{t} = 1.3s$ and $\hat{t} = 1.52s$ is illustrated by Figure 8.15 which displays the temperatures isocontours and vorticity contours where the dimensional vorticity is defined by:

$$\omega = \frac{\partial v}{\partial x} - \frac{\partial u}{\partial y} \tag{8.2}$$

The bluish regions indicate the clockwise vortex structures and the reddish regions the counter clockwise vortex ones. The flame bulge is prominent by the isocontour of temperature. Meanwhile, the red isoline represents the flame sheet and evidences the detachment of fuel pockets. As previously described, these pockets are regions of hot gas enclosed by a flame that travels upward. The effective entrainment of oxidizer in the region of the axis of symmetry is found to be the main mechanism of the flame local extinction and release of this secondary flame. Detached fuel pockets can be observed in Figures 8.15c and 8.15f. Also, Figure 8.15 displays the probe location where the data from Figure 8.14 were acquired. This location was chosen for illustrating the passage of the large vortical structure formed by the buoyant effect, a key feature for the correct flame flickering frequency analysis. Beyond the correct prediction of the flickering frequency, the unsteady flame structure appeared to be in line with the results presented in the literature (not shown here).

Figure 8.15 - (a) $\hat{t} = 1.3s$, (b) $\hat{t} = 1.35s$, (c) $\hat{t} = 1.39s$, (d) $\hat{t} = 1.43s$, (e) $\hat{t} = 1.47s$, (f) $\hat{t} = 1.52s$. The red isoline represents the flame sheet ($Z = 1$) and the blue X marker represents the location of the probe from Figure 8.14a.

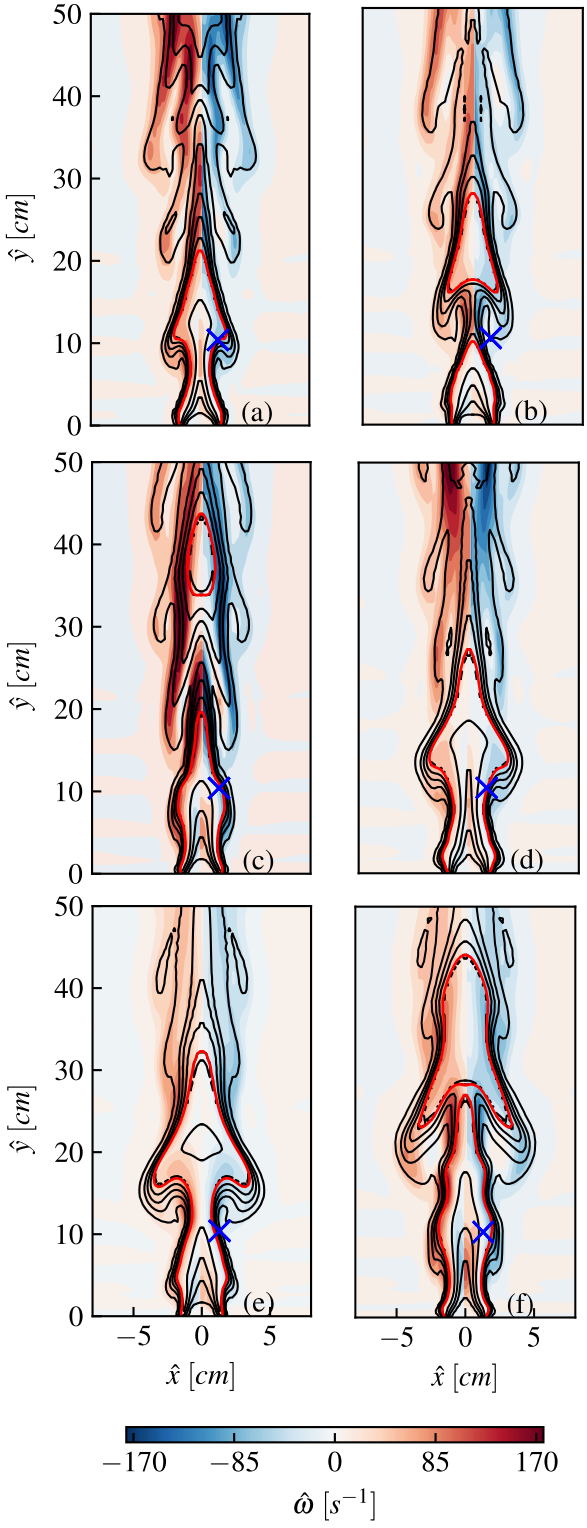

SOURCE: The Author.

Part III

Numerical Study

9 NUMERICAL STUDY

In this section, the Tsuji Burner configuration is going to be analysed through a set of scenarios. In Figure 9.1 is presented the schematic view of the three main Tsuji burner configurations investigated here. These cases share the same particularity of a two-dimensional geometry, thereby an infinite cylinder.

The particularity of the first case (presented in Figure 9.1a and namely Case A) is the absence of gravity and the presence of an inlet velocity of oxidant from upstream the cylinder. The Case A is referenced as "Classical Tsuji Flame" because is the one that resembles the most the experimental setup proposed by Tsuji and Yamaoka (1969). At the contrary, the second case, namely Case B and shown in Figure 9.1b, the gravity effect is present, but the main distinction is that the ambient temperature varies from two to five times the burner temperature. Finally, the third case, namely Case C, is the buoyant case with regular ambient temperature and parameters that allows the cyclic transient behaviour of the flame.

On this section, the dimensionless independent and dependent variables for (time, spatial coordinates, velocities, temperature and pressure) for all cases are defined as $\tau \equiv \hat{\tau}(\hat{u}_b/\hat{a})$, $x \equiv \hat{x}/\hat{a}$, $y \equiv \hat{y}/\hat{a}$, $u \equiv \hat{u}/\hat{u}_b$, $v \equiv \hat{v}/\hat{u}_b$, $T \equiv \hat{T}/\hat{T}_\infty$ and $p \equiv \hat{p}/\hat{\rho}_\infty \hat{u}_b^2$. The fuel and oxidant mass fractions are normalized according to $Y_F \equiv \hat{Y}_F/\hat{Y}_{F_b}$ and $Y_O \equiv \hat{Y}_O/\hat{Y}_{O_\infty}$, respectively.

The independent variables are nondimensionalized with the burner radius for the Cases A and B, and the burner diameter for the Case C, but as seen in the Section 11, the appropriated characteristic length scales are imposed not only by the burner geometry but also by the buoyant force and the combustion process.

Figure 9.1 - Schematic view of (a) Case A (classical Tsuji burner), (b) Case B (buoyant Tsuji burner with heated atmosphere) and (c) Case C (puffing Tsuji burner).

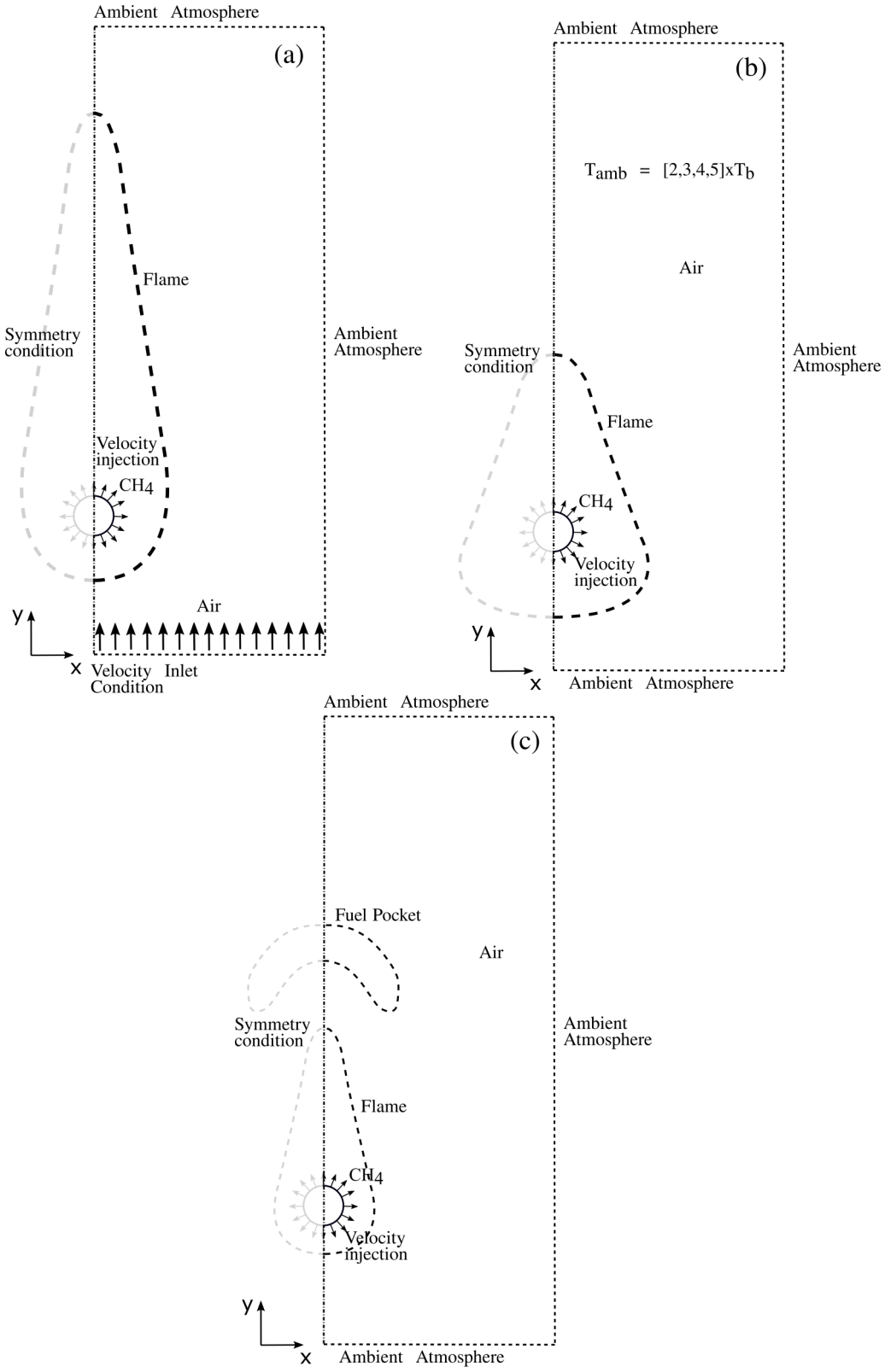

SOURCE: The Author.

9.1 Boundary conditions

Equations 4.10-4.12 and 5.5-5.7 are integrated with the following boundary conditions: on the symmetry axis ($x = 0$),

$$u = \partial_x v = \partial_x p = \partial_x Z = \partial_x H = 0, \tag{9.1}$$

at the burner surface ($r^2|_+ = x^2 + y^2 = 1^+$),

$$u - x = v - y = \partial_n p = 0, \quad Z_s - Pe^{-1}\partial_n Z = S_Z, \quad H_s - Pe^{-1}\partial_n H = S_H, \tag{9.2}$$

(Robin's like boundary type for Z and H) where $Z_s \equiv SY_{Fs} - 1$, $H_s \equiv (S+1)T_s/Q + Y_{Fs}$ and the subscript n stands for the normal coordinate. The terms S_Z and S_H are Z and H fluxes at the burner injection surface $r^2|_- = x^2 + y^2 = 1^-$ as function of $\hat{Y}_b$, $\hat{T}_b$ and $\hat{u}_b$, namely $S_Z \equiv S + 1$ and $S_H \equiv (S+1)T_b/Q + 1$. Note that Y_{Fs} and T_s will be found as part of the solution of the problem.

The boundary conditions for the limits of the computational domain, h_y and l_x, the height and length, respectively, are dependent on the particular case:

- For Case A, for $-y \to h_y \gg 1$:

$$v - 1 = u = Z = H - H_\infty = 0 \tag{9.3}$$

  for $(x, y) \to (l_x, h_y)$, with $l_x \gg 1$ and $h_y \gg 1$:

$$\partial_n u = \partial_n v = Z = H - H_\infty = 0 \tag{9.4}$$

  in which $H_\infty \equiv (S+1)/Q + 1$.

- For Case B, for $(x, |y|) \to (l_x, h_y)$, with $l_x \gg 1$ and $h_y \gg 1$:

$$\partial_n u = \partial_n v = Z = H - H_\infty = 0 \tag{9.5}$$

- For Case C, for $(x, |y|) \to (l_x, h_y)$, with $l_x \gg 1$ and $h_y \gg 1$

$$\partial_n u = \partial_n v = \partial_n Z = \partial H = 0 \tag{9.6}$$

According to the definition of the mixture fraction Z, the flame position (x_f, y_f) is determined by the isoline $Z(x, y) = 1$. The subscript f stands for flame condition.

On the isoline $Z = 1$, the flame temperature T_f is determined by $H(x_f, y_f) = (S + 1)T_f/Q$.

There is no need to prescribe boundary conditions for the pressure, due to the recourse of the fully staggered grid, as shown in Figure 6.4. However, the combination of the mesh type and the artificial compressibility method demands a prescribed value of pressure at one point of the mesh. This point sets the pressure level but retains the freedom of getting the pressure gradient from the artificial continuity equation.

10 CASE A: CLASSICAL TSUJI FLAME

10.1 Asymptotic analysis

Far from the burner, the velocity field is given approximately by $(u, v) = (0, V)$, and the burner can be seen as a line source of Z.

In that case, Equation 5.5 can be simplified to $V\partial_y Z = Pe^{-1}\partial_{xx} Z$, whose solution, which is analogous to the classical problem of the point source of heat in transient heat conduction, is given by (CARSLAW; JAEGER, 1959)

$$Z = (y_f/y)^{1/2} exp[-(VPe/4)x^2/y] \tag{10.1}$$

in which the condition of $Z = 1$ at $(x, y) = (0, y_f)$ (i.e., at the flame tip) was used. The boundary conditions far from the burner are automatically satisfied by the solution, and the boundary condition at the burner can not be used, since the solution fails to describe the distribution of Z close to it. Therefore, the flame height can not be found through analytical means.

An approximate expression for the flame shape is found substituting $Z = 1$ on Equation 10.1, leading to

$$(VPe/2y_f)x^2 = -(y/y_f)ln(y/y_f) \tag{10.2}$$

and the maximum flame width is $x_f = (2y_f/eVPe)^{1/2}$ at $y = y_f/e$.

10.2 Navier-Stokes vs potential flow

Figure 10.1 exhibits the flame shape and the streamlines obtained by the solution of the Navier- Stokes flow, (10.1a), and by the potential flow, (10.1b), given by

$$\begin{aligned} u &= -2Vxy/(x^2+y^2)^2 + x/(x^2+y^2), \\ v &= V[1 + (x^2-y^2)/(x^2+y^2)^2] + y/(x^2+y^2). \end{aligned} \tag{10.3}$$

for the case $V = 3$ and $Pe = 1$. In addition, the analytical flame shape, from Equation 10.2, is presented for both cases with the value of y_f given by each solution. It can be seen that there is relatively good agreement in the flame shape between the analytical solution and that found from the potential flow (right side). This

agreement is also observed for the flame shape found by the Navier–Stokes flow on the upper part of the flame, but the agreement fails in the lower part of the flame. Due to the absence of viscous effects, the potential flow underestimates the influence of the burner on the flow and the streamlines confirm this statement. On the other hand, the Navier–Stokes model describes well the streamlines in the bottom part of the flame, showing an important contribution of the burner in the x direction velocity, and consequently on the flame shape. Then, the fuel convective transport in x direction pushes the flame farther from the burner. The behavior of the flame in that region of the flow establishes the shape for the whole flame.

Precisely, Figure 10.1 shows the isoline $Z = 1$, the stoichiometric surface. The stoichiometric surface represents the flame in the regions in which the stability conditions are satisfied. For $y_f >> 1$, the velocity field returns to uniform configuration, i.e. unstrained flow field. Indeed the fuel concentration is low but the temperature inside the stoichiometric surface is very close to the flame temperature, which create conditions for stable flame, according to the large activation energy asymptotics.

Figure 10.1 - Flame shapes (dashed line: numerical calculation; dotted line: analytical model, Equation 10.2) and streamlines in the numerical domain are presented: (a) flow described by numerical solution of the Navier–Stokes equations and (b) flow described by the potential flow approximation. The conditions addressed lead to $V = 3$ and $Pe = 1$. The fitting constant y_f in analytical solution is different in the two cases: (a) for Navier–Stokes flow $y_f = 204.6$ and (b) for potential flow $y_f = 270.1$.

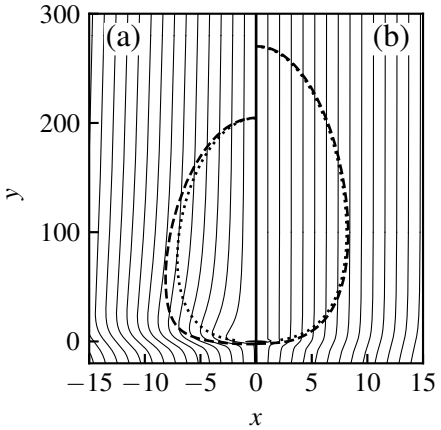

SOURCE: The Author.

To check with a higher degree of precision the existence of flame far from the burner, it would be necessary to include radiative heat loss and to employ other asymptotic method considering a more complex chemical mechanism (rate-ratio asymptotics) (PETERS; WILLIAMS, 1987; SESHADRI; PETERS, 1988; FACHINI; SESHADRI, 2003) or through numerical simulation with detailed chemical mechanism.

Figure 10.2 - The analytical distribution of Z along x and those obtained by Navier–Stokes and potential flow in terms of the similarity variables of Equation 10.1 at $y = 20, 100$, for $V = 1$ and $Pe = 3$.

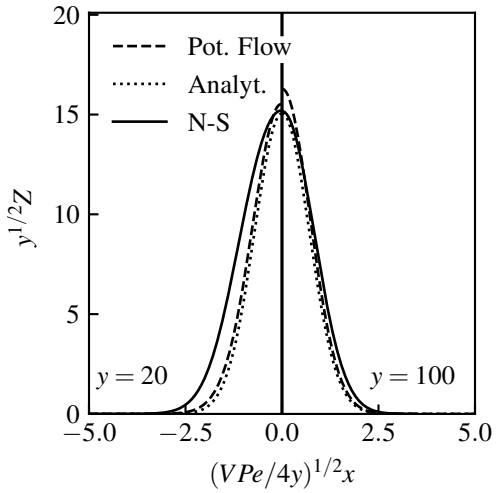

SOURCE: The Author.

Figure 10.2 shows the distribution of Z along the x direction for the numerical solutions and the analytical solution given by Equation 10.1. In order to put in evidence the similarity behavior of Z distribution, the ordinate represents $\sqrt{y}Z$ and the abscissa represents $(VPe/4y)^{1/2}x$. For $y = 20$, which is relatively close to the burner, there is good agreement between the solution from potential flow and the analytical one, since the flow is almost parallel in the potential flow, as shown in Figure 10.1. However, the Navier–Stokes flow is not parallel at $y = 20$, then the Z distribution is different from those found by potential flow and analytical model. For $y = 100$, however, all three solutions shows good agreement, because the flow is almost parallel, confirmed by Figure 10.1b. It can be observed a slightly overestimation in Z for the potential flow close to $x = 0$, Figure 10.2 right side, which causes a large overestimation in the flame height, confirmed by Figure 10.1, since the gradients of Z are weak far of the burner.

Figure 10.3 - Maximum flame width as a function of the free stream velocity V, keeping $Pe = 1$ (continuous line), and of the Peclet number Pe, keeping $V = 3$ (dashed line).

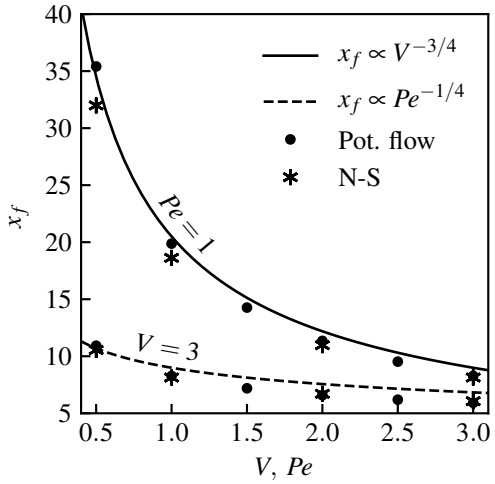

SOURCE: The Author.

Numerical results show that the dependence of x_f on Pe and V is given by $x_f \propto Pe^{-1/4}V^{-3/4}$, as exhibited in Figure 10.3. The decrease of x_f with V can be compared to the width of the wake generated by the fuel injection downstream of the burner, which is proportional to V^{-1} .

Making use of the behavior for the flame width x_f and the asymptotic solution, Equation 10.1, the behavior for the flame height is revealed to be $y_f \propto (Pe/V)^{1/2}$. This expression shows the reduction of y_f with the free stream velocity according to $V^{-1/2}$. Furthermore, imposing $Z \sim S + 1$ for $y \sim 1$ on Equation 10.1, one finds $y_f \sim (S + 1)^2$. Then, the dependence of the flame height y_f on the nondimensional parameters can be written as $y_f = A(S+1)^2(Pe/V)^{1/2}$, in which the fitting constant A is 3.8, as seen in Figure 10.4. Therefore, making use again of Equation 10.1 and the expression for y_f, the characteristic length scales of the problem (order of magnitude of flame width and flame height) are

$$L_x \sim (S + 1)/(Pe^{1/4}V^{3/4}), \tag{10.4}$$

$$L_y \sim (S + 1)^2(Pe/V)^{1/2} \tag{10.5}$$

Figure 10.4 - Flame height as a function of the free stream velocity V, keeping $Pe = 1$ (continuous line), and of the Peclet number Pe, keeping $V = 3$ (dashed line), obtained by Navier-Stokes flow.

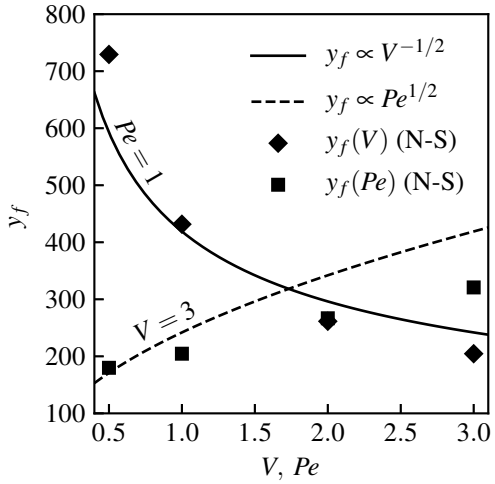

SOURCE: The Author.

The reduction on the flame width x_f with V causes an increase of fuel diffusive transport to the flame, which represents an increase of fuel consumption, leading to a decrease of flame height, as shown in y_f. Although the increase on Pe also decreases the flame width, this dependence is weaker than the dependence on V. This is the reason of the increase of y_f with Pe since, for fixed V, the increase on Pe decreases the intensity of the diffusion. Since diffusion is the only process that provides transport of the reactants far from the burner, it is required a larger distance (larger flame height) to the fuel to react with the oxidizer.

Another important result depicted by x_f and y_f is the dependence on S. For burning of pure hydrocarbon in air, it is generally found $S \leq 20$, then the terms $S + 1$ and $(S + 1)^2$ can be seen as order of magnitude for x_f and y_f, respectively.

Therefore, the asymptotic solution, Equation 10.1, captures the most important processes that control the flame shape under the condition of $(S + 1)^2 \gg 1$, because the major part of the flame is in a practically parallel flow field.

Based on these results, it is possible to affirm that the large value of y_f was the reason for covering the backward surface of the cylindrical burner, as presented by Tsuji and Yamaoka (1967). The covered surface reduces not only the fuel injection

but also creates recirculation in the wake, which help to diminish even more the flame height by increasing the total area of the flame.

11 CASE B: BUOYANT TSUJI FLAME

The cases presented and commented in this section are chosen to highlight the processes controlling the diffusion flame established around a horizontal cylindrical burner with a buoyancy-driven flow. In all cases, $\hat{a}$ and $\hat{u}_b$ are chosen to satisfy $Re \leq 30$, preventing any type of instabilities of the flame above the burner.

The temperature distribution exhibited in the figures is in dimensional form to facilitate the comparison between the plots. Since the dimensional temperature of the ambient atmosphere changes from case to case, the burner temperature is fixed and the flame temperature varies slightly among the cases, then, it was decided to present the dimensional temperature in the figures which leads to a minimal number of modifications from case to case. In all cases the burner temperature is $\hat{T}_b = 300K$ and the fuel is methane.

11.1 Analysis of order of magnitude

Tsuji diffusion flames around cylindrical porous burner considering natural convection are quite similar to those established considering forced convection. In the latter case, the x-component (across the flame) of the convective transport is negligible. However, in the former case, oxygen is transported by convection from the ambient atmosphere to near the flame, which imposes a higher oxygen flux to the flame. Therefore, the fuel consumption is also augmented and, consequently, the flame dimensions are reduced. To have a fundamental comprehension of Tsuji diffusion flames under the influence of natural convection, the characteristic spatial and velocity scales imposed by the buoyant force, fuel injection and combustion are determined.

The orders of magnitude of the flame width L_x ($\equiv \hat{L}_x/\hat{a}$), flame height L_y ($\equiv \hat{L}_y/\hat{a}$), variation of velocity in the x-direction U ($\equiv \hat{u}_\infty/\hat{u}_b$) and variation of velocity in the y-direction V ($\equiv \hat{v}_\infty/\hat{u}_b$) are defined. The order of magnitude L_x is set at $y = L_y/e$ and L_y at the flame tip $x = 0$. The characteristic velocities driven by the buoyancy are defined by $(\hat{u}_\infty, \hat{v}_\infty)$. From the mass conservation, the following relation is found $U/L_x \sim V/L_y$.

Balancing inertia and buoyant force terms in the y-component of the Navier-Stokes equation, the second and last terms of Equation 4.6, one finds the relation $V^2/L_y = \Delta^2/(Fr)^2$, in which $\Delta^2 \equiv 1 - 1/T_f$. In the same way, balancing the inertia and viscous terms of the Navier-Stokes equation, the second and the fourth terms of

Equation 4.6, a third relation among the properties is obtained, $U = 1/PeL_x$. In the order of magnitude analysis, the approximation $Re = Pe$ is justified since the Prandlt number Pr is the order of unity.

The fourth relation, necessary to close the system, is the flame width found in the Tsuji flame established by forced convection, $L_x = (S+1)Pe^{-1/4}V^{-3/4}$ (BIANCHIN et al., 2019). Although the flame width L_x is not explicitly dependent on the x-component of the velocity U, its dependence is through the y-component of the velocity V.

Then, the scales of the problem can be specified as a function of the Froude (Fr) and Péclet (Pe) numbers, the expansion parameter (Δ) and the combustion parameter (S) according to

$$L_x = Pe^{-2/5}(\Delta/Fr)^{-3/5}(S+1)^{2/5}, \tag{11.1}$$

$$L_y = Pe^{2/5}(\Delta/Fr)^{-2/5}(S+1)^{8/5}, \tag{11.2}$$

$$U = Pe^{-3/5}(\Delta/Fr)^{3/5}(S+1)^{-2/5}, \tag{11.3}$$

$$V = Pe^{1/5}(\Delta/Fr)^{4/5}(S+1)^{4/5}. \tag{11.4}$$

Note that, since the Péclet number is based on the burner properties, it determines qualitatively the effect of the fuel injection from the cylindrical burner on the flow field and on the flame. In the same way, the term Δ/Fr quantifies the effect of buoyancy on the flow field and on the flame. While $(S+1)$ term measures qualitatively the effect of the combustion process on the flow field. This simple analysis reveals also the dependence of the flame length on S, which is not as strong as in forced convection case because of the oxidant flux across the flame.

The set of Equations 11.1 to 11.4 is also consistent with the known behavior of flames i) in the micro-gravity regime $\Delta/Fr \to 0$ (QIAN; LAW, 1997), where $(L_x, L_y \to \infty)$ and ii) in the forced convection regime where the velocity component V is vanishing (BIANCHIN et al., 2019).

11.2 Influence of Δ/Fr, Pe and S on the flame

Figure 11.1 presents the behavior of the whole flame with reduction in the buoyancy through reduction in the density difference in the buoyant force, $(1-\rho)/Fr^2$, imposed by the increase of the ambient-atmosphere temperature.

Figure 11.1 - The colormap contour shows the temperature distribution and the dashed line shows the flame shape for different ambient temperature: a) $\hat{T}_\infty = 2\hat{T}_b$ ($1/T_b = 2$, $Pe = 7.83$, $Fr = 1$, $\Delta = 0.84$) and b) $\hat{T}_\infty = 4\hat{T}_b$ ($1/T_b = 4$, $Pe = 3.6$, $Fr = 1$, $\Delta = 0.63$). The cylindrical burner is represented here by the black area at the origin $(x, y) = (0, 0)$.

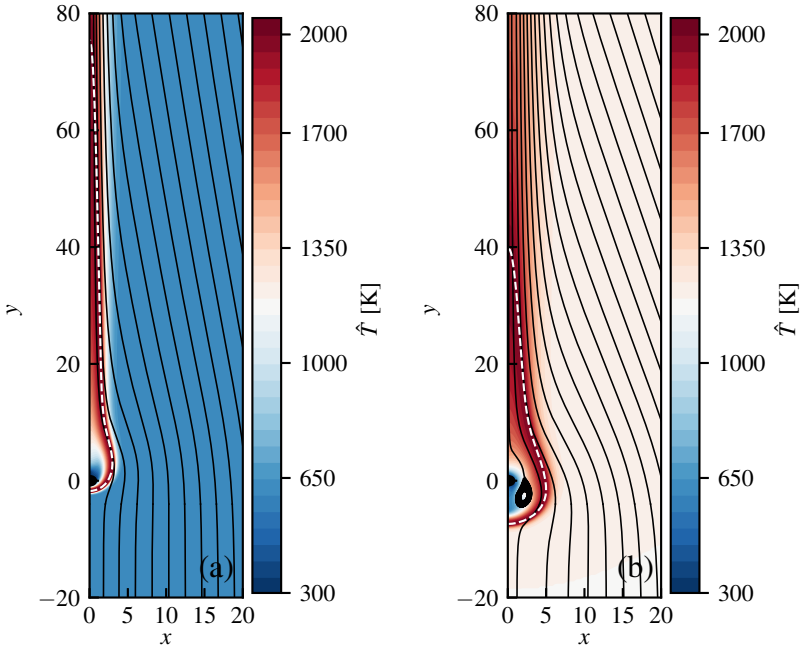

SOURCE: The Author.

From an analysis of Equations 11.1 to 11.4, it is seen that a decrease of the buoyancy term Δ/Fr through an ambient-atmosphere temperature rise leads to a reduction of the velocity components (U, V). The consequence is a decrease of the oxygen and fuel convective fluxes to the flame. The decrease of the oxygen convective flux, which is almost perpendicular to the flame, forces the flame to move away from the symmetry axis, i.e., the flame width increases. This behavior is correctly captured by the expression for L_x, Equation 11.1, and confirmed by the numerical results shown in Figure 11.2a. However, the same arguments can not be used to describe the effects of the reduction of fuel convective transport on the length of the flame L_y. Since the fuel convective transport occurs mainly along the flame, its reduction results in a shortening of the flame associated to the fuel concentration decrease inside the flame. The proof of this conclusion is given by the dependency of the fuel flux on buoyancy. From Equations 11.1 and 11.4, it is seen that the fuel convective transport in a cross-section of the flame diminishes with the reduction of the buoyancy, according

to $L_y \sim L_x V \sim (\Delta/Fr)^{-1/5}$. As in jet flames, the fuel convective transport in the y direction determines the flame length, those results are confirmed by the numerical results presented in Figure 11.2b.

Figure 11.2 - a) Flame width x_f at $y = y_f^+/e$ and b) flame height y_f^+ as a functions of the Froude number, for $\hat{T}_\infty = 3\hat{T}_b$, $Pe = 5.2$, $\Delta = 0.74$, $S = 9.5$.

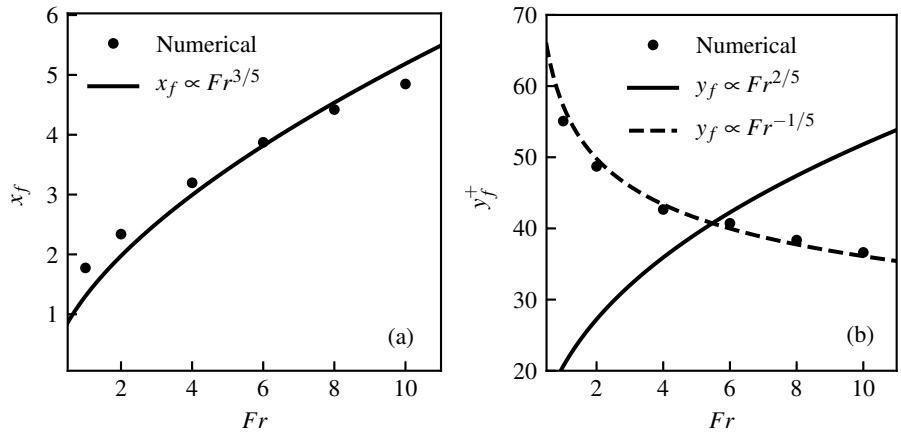

SOURCE: The Authors.

It is worth noticing that the expression for the flame length $L_y \sim (\Delta/Fr)^{-2/5}$, given by Equation 11.2, does not capture the flame shortening driven by the decrease of the buoyancy in the addressed conditions. Contrarily, the flame length increases with the reduction of the buoyancy. This behavior is found for a vanishing buoyant force (QIAN; LAW, 1997) and in forced convection Tsuji flames with incoming velocity approaching zero (BIANCHIN et al., 2019). Therefore, combining these two behaviors, it is possible to deduce that the reduction of the buoyancy initially shortens the flame length because of the decrease in the y-component of the fuel convective transport. After that, the reduction in the buoyancy extends the flame length because the y-component of the fuel diffusive and convective transport become of the same order. In such a condition, both processes control the behavior of the flame in the y direction. The condition $L_y \sim L_x$ (or from the mass conservation $V \sim U$) reflects the above statement and is derived from $(\Delta/Fr) \sim [Pe^4(S+1)^6]^{-1} \ll 1$. Taking this result into Equation 4.6 and re-scaling the time, spatial dimensions and velocity, it is seen that the transient period would be of the order of $\tau_c \sim (\Delta/Fr)^{-2} = [Pe^4(S+1)^6]^2 \gg 1$, the characteristic spatial dimensions of the flame would be $(x_c, y_c) \sim (\Delta/Fr)^{-1} = [Pe^4(S+1)^6] \gg 1$ and the characteristic velocity imposed by fuel injection and

buoyancy would be $(u_c, v_c) \sim (\Delta/Fr) = [Pe^4(S+1)^6]^{-1} \ll 1$.

Figure 11.3 - a) Flame width x_f at $y = y_f^+/e$ and b) flame height y_f^+ as a functions of the Péclet number, for $\hat{T}_\infty = 3\hat{T}_b$, $Fr = 1$, $\Delta = 0.74$, $S = 9.5$.

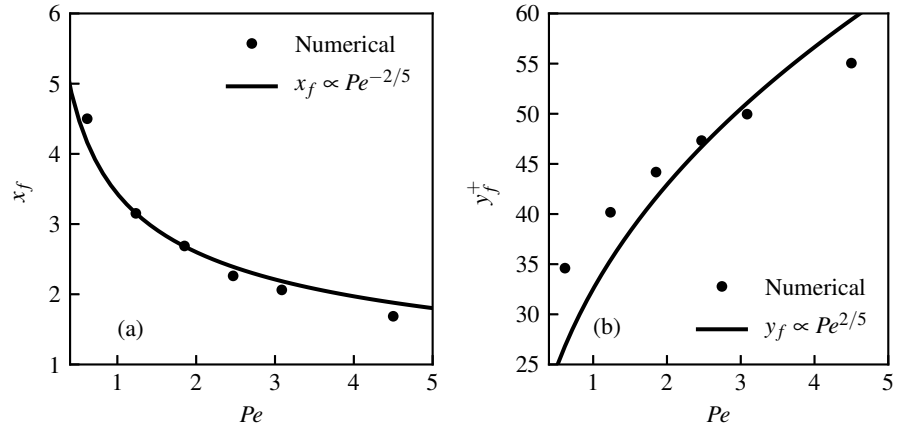

SOURCE: The Author.

Figure (11.3) exhibits the behavior of the flame dimensions (width and length) in terms of Péclet number Pe. The results from the order of magnitude analysis for the flame width $x_f \sim Pe^{-2/5}$ and flame height $y_f^+ \sim Pe^{2/5}$ are in line with the trend observed in the numerical results, as seen in plots (11.3.a) and (11.3.b). An increase in the Péclet number means that more fuel mass is injected by augmenting the velocity of injection and/or the surface area of the burner. The injection of more fuel leads to a longer flame for burning it, as seen in Figure 11.3b. Elongated flame represents buoyant force acting over a large distance which increases the velocity along the flame as $V \sim Pe^{1/5}$. However, as in forced convection Tsuji flames (BIANCHIN et al., 2019), the increase on the y-component of the velocity reduces the flame width, as depicted in Figure 11.3a.

Figure 11.4 shows the dependence of the width and length of the flame on the combustion parameter S. Since S influences the flame temperature, and hence the expansion parameter Δ, then the behavior of the flame width and length are compared with $\Delta^{-3/5}(S+1)^{2/5}$ and $\Delta^{-2/5}(S+1)^{8/5}$, respectively. As seen in both plots, Figures 11.4a and 11.4b, an increase in the fuel concentration of the fuel stream injected at the burner demands the flame dimensions to become larger for burning stoichiometrically the additional amount of fuel.

Figure 11.4 - a) Flame width x_f at $y = y_f^+/e$ and b) flame height Y_F as a functions of the combustion parameter S, for $\hat{T}_\infty = 3\hat{T}_b$, $Fr = 1$, $Pe = 4.5$, $0.735 \leq \Delta \leq 0.748$.

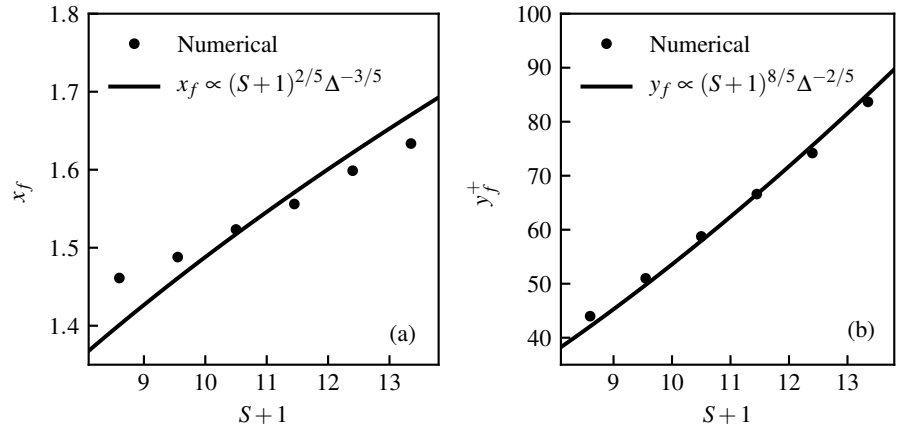

SOURCE: The Author.

Figure 11.5 shows the whole re-scaled flame for four ambient-atmosphere temperatures $\hat{T}_\infty = (2.5,\ 3,\ 3.5,\ 4) \times \hat{T}_b$ and all of them present practically the same dimensions. The concordance of these dimensions confirm that the spatial scales L_x and L_y are the proper scales to study flames established around a Tsuji burner. As can be easily noted, the flame shape for the case $1/T_b \equiv \hat{T}_\infty/\hat{T}_b = 4$ is displaced downward. The reason for that is the establishment of a second recirculation zone (second vortex) below the burner. The presence of this vortex changes substantially the flow field close to the burner and the flame as consequence. The discussion of the flow field under several ambient-atmosphere conditions is presented in detail below.

11.3 Influence of the ambient-atmosphere temperature on the flow field

The flow field above the burner is controlled only by the positive buoyancy of the hot gases. Under this force, the flow field can be described as parallel and is accelerated, like the flow field found in jet flames, as seen in Figure 11.1. However, the flow field changes drastically around to (above and below) the burner. The combination of the buoyant hot gases (around the flame) and the buoyant cold gases (around the burner) and the fuel injection imposes a different flow field morphology. This flow field resembles the one imposed by a forced flow around a cylinder, from which fluid is injected backward and forward in the direction of the forced flow (SEN et al., 2017).

Figure 11.5 - Re-scaled flame coordinates y_f/L_x and x_f/L_y for several value of the ambient-atmosphere temperatures $\hat{T}_\infty = 2.5\hat{T}_b,\ 3\hat{T}_b,\ 3.5\hat{T}_b,\ 4\hat{T}_b$. The values of the parameters are $Fr = 1$, $S = 9.5$, $Pe = 5.93,\ 5.2,\ 4.35,\ 3.6$ and $\Delta = 0.79,\ 0.74,\ 0.68,\ 0.63$, respectively.

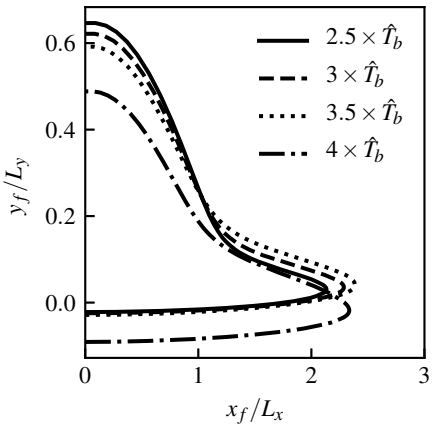

SOURCE: The Author.

Figure 11.6 - The plots show the streamlines and the temperature contour for different ambient temperature: a) $\hat{T}_\infty = 2\hat{T}_b$ ($Pe = 7.83$, $Fr = 1$, $\Delta = 0.84$), b) $3\hat{T}_b$ ($Pe = 5.2$, $Fr = 1$, $\Delta = 0.74$), c) $3.5\hat{T}_b$ ($Pe = 4.35$, $Fr = 1$, $\Delta = 0.68$) and d) $4\hat{T}_b$ ($Pe = 3.6$, $Fr = 1$, $\Delta = 0.63$). The color-scale contour shows the dimensional temperature distribution for all cases.

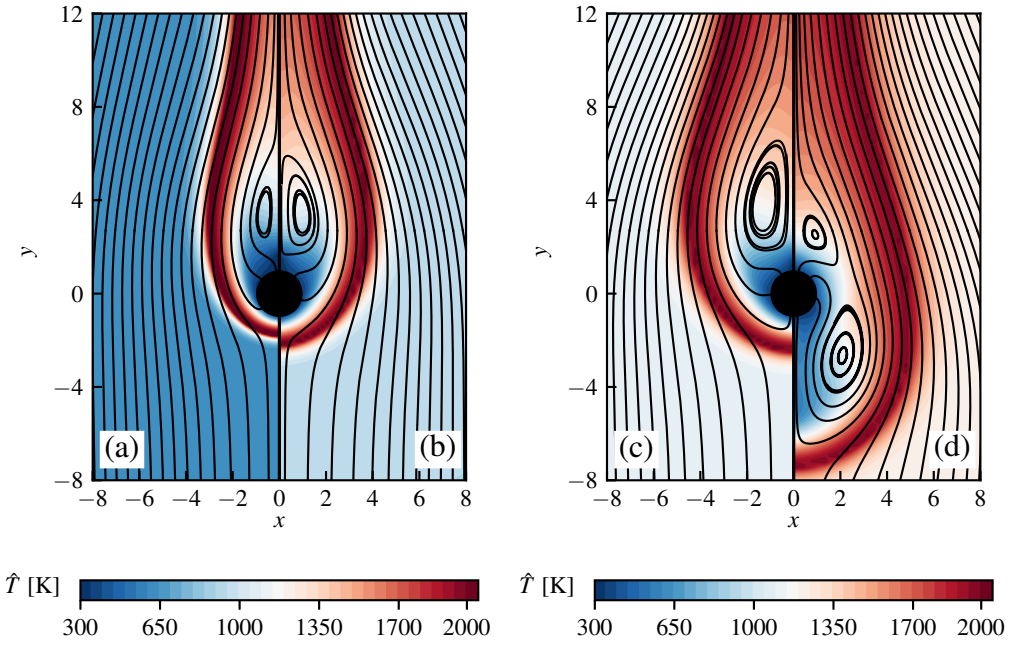

SOURCE: The Author.

The focus of this section is on the processes controlling the flow field around the burner, in which the forward counterflow (Tsuji) diffusion flame is established. As proposed in this analysis, the conditions of low strain rate for the Tsuji flame are sought.

Figure 11.6 presents the flow field and the temperature distribution close to the burner. in which the recirculation zones are established. For ambient-atmosphere temperatures such that $\hat{T}_\infty = 2\hat{T}_b,\ 3\hat{T}_b,$ and $3.5\hat{T}_b$, Figures 11.6a, 11.6b and 11.6c, the positive buoyant force overwhelms the negative one, even close to the burner. In this scenario, the positive y-component of velocity is high enough to maintain the recirculation zone above the burner, as well as the counterflow region close to the bottom side of the cylinder. The vortex above the burner is established at a certain distance from the burner because of the fuel injection. Unlike the recirculation zone generated in the forced convection regime whose width is of the order of the cylinder radius, in the present analysis, the vortex width depends not only on the burner radius but also on the flame width, in which the buoyant force accelerates the flow. Since the flame width increases with the reduction in the buoyant force, then the vortex becomes wider as buoyancy is reduced.

The backward recirculation zone is due to adverse pressure gradient generated by the buoyancy-driven flow field, which is imposed by the presence of the flame. The flow field close to the burner is comparable to the (frozen) flow past a cylinder with vortex shedding control through the blowing of the cylinder surface (LI et al., 2003). However, the main difference between the frozen and reacting flow is the x- component of the velocity generated by the buoyancy, which is responsible for keeping the vortex stable within the fuel zone/ wake, preventing the occurrence of vortex shedding. These changes in the flow field and temperature distribution are proportional to the variation of the ambient-atmosphere temperature.

As seen in Figure 11.6d, the flow field changes dramatically for an ambient-atmosphere temperature $1/T_b = \hat{T}_\infty/\hat{T}_b = 4$. An additional recirculation zone can be observed below the burner, about $y = -4$. This new recirculation zone modifies completely the flow field, which changes the flame shape and consequently the temperature distribution and the buoyant force field. The conditions addressed in that case are such that the negative buoyant force of the cold fuel, surrounding the cylindrical burner, overcomes the positive one, which imposes a negative y-component of velocity. In addition to that, the region in which negative buoyancy is found increases drastically, as shown by the blue region of Figure 11.6d. The consequences

are a wider flame and a stagnation point pushed away from the burner.

Figure 11.7 - Streamlines for different ambient-atmosphere temperature: a) $\hat{T}_\infty = 2.5\hat{T}_b$, b) $3.5\hat{T}_b$, c) $3.8\hat{T}_b$, d) $3.89\hat{T}_b$, e) $3.895\hat{T}_b$ and f) $4.5\hat{T}_b$.

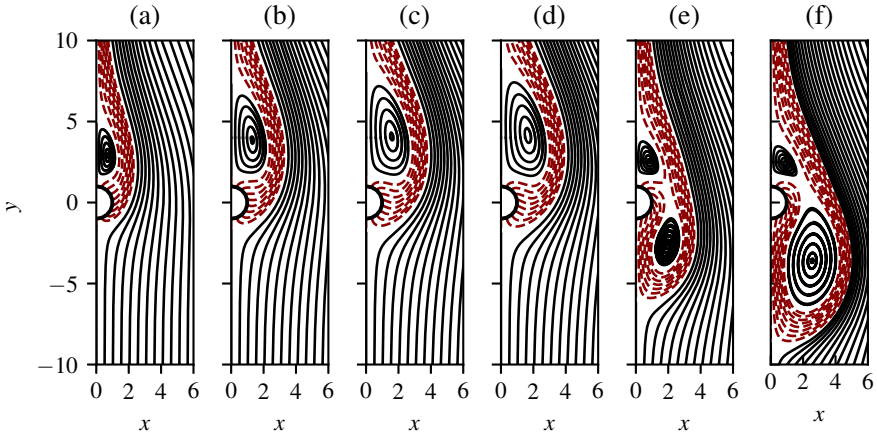

SOURCE: The Author.

Therefore, the increase of the ambient-atmosphere temperature has two opposed effects: a reduction of the positive buoyancy and an increase of the negative one. The latter drives the cold fuel more downwards below the burner, creating a cold gases pocket which deviates the inflow. The consequence is a wider flame.

The dramatic impact of the increase of the ambient-atmosphere temperature on the flow field is evident in Figure 11.7. The switch between a one-vortex to a two-vortex configuration is observed when $\hat{T}_\infty$ exceeds a critical value of $3.895\hat{T}_b$. Below that value, the one-vortex configuration prevails (Figures 11.7a to 11.7d) with a standalone upper vortex whose size is an increasing function of $\hat{T}_\infty$ and whose location is slightly shifted away from the cylinder as $\hat{T}_\infty$ increases. Above the critical value of $\hat{T}_\infty$, the two-vortex configuration takes over, Figs 11.7e,f. The change of the patterns of the streamlines originating from the injection surface of the burner (red colour and dashed lines) is clearly visible. This is caused by the fact that the negative buoyant force overwhelms the positive one. As a consequence, the descending cold gases and the ascending hot gases are energetic enough to create a circular anticlockwise motion corresponding to the observed lower vortex. It is worth mentioning the pattern of the streamlines in the recirculation zone does not represent the mass flow rate.

Figure 11.8 - Flame shape (dashed line) and nondimensional vorticity contour, scaled by $\Omega = V/L_x - U/L_y$, for different ambient temperature: a) $\hat{T}_\infty = 2\hat{T}_b$ ($Pe = 7.83$, $\Delta = 0.84$) and b) $\hat{T}_\infty = 4.5\hat{T}_b$ ($Pe = 3$, $\Delta = 0.58$). The colormap contour shows the vorticity ω/Ω distribution and the continuous line represents the isocontour of $\omega/\Omega = 0$.

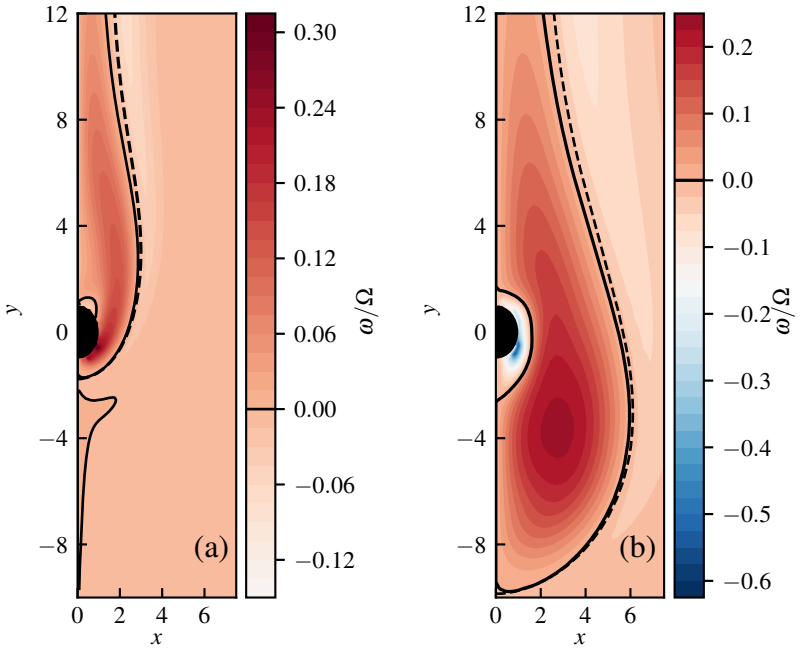

SOURCE: The Author.

As a consequence of the one and two-vortex configurations, the combustion-driven buoyancy creates two vortical structures close to the burner, as shown in Figure 11.8. The first structure presented by Figure 11.8a is quite similar to the configuration of a non-reactive flow past a cylinder without injection (FORNBERG, 1980). The vortex is found in the wake of the burner as the one-vortex configuration, but the maximum positive vorticity value is situated close to the surface of the burner where the injected fuel is highly deflected by the positive buoyant force.

As seen in Figure 11.8b, the second vortical structure appears due to the two-vortex configuration with high vorticity driven by the pair of negative and positive buoyant forces below the burner, which create a large vortex in the fuel-containing region, centred at $(x, y) = (3, -4)$. Increasing the ambient-atmosphere temperature, not only increases the intensity of the negative buoyant force but also the extension of the region in which this force is found. Therefore, the vorticity is spread below the

burner in a large region of the flow. This upstream vortical structure is similar to that found in a non-reactive flow past a cylinder, from which fluid is injected and aligned with the free stream flow (SEN et al., 2017). However, in that configuration the upstream vortex is unstable, i.e., the vortex position initially oscillates and after that is completely detached from the cylinder. On the other hand, the buoyancy-driven vortical structure analysed in the present work remains close to the cylinder, inside the fuel region and enclosed by the flame.

To quantify the overall effect of the ambient-atmosphere temperature $\hat{T}_\infty$ on the vorticity, it is defined the following vorticity integral

$$\omega_T = \int_{-L}^{L} \left(\int_{0}^{x_f(y)} |\omega| dx \right) dy$$

over the fuel-containing region (limited by the dashed line as seen in Figure 11.8). The dimensionless vorticity ω is $\omega = \partial_x v - \partial_y u$. This definition captures not only the changes of the vorticity intensity but also the changes on the extension of the flame, as can be seen in two cases exhibited in Figure 11.8. The total vorticity varies from $\omega_T = 2.16$ to $\omega_T = 16$, for $\hat{T}_\infty = 2\hat{T}_b$ and $4.5\hat{T}_b$, respectively.

Also, Figure 11.8 reveals that the vorticity is well scaled by the properties found in the order of magnitude analysis, i.e., $\Omega = V/L_x - U/L_y$. Since $L_y \gg L_x$ and $V \gg U$, then the estimate of the vorticity can be written as $\Omega = V/L_x$, which reveals the dependence of the vorticity on the problem parameters $\Omega = Pe^{3/5}(\Delta/Fr)^{7/5}(S+1)^{2/5}$.

11.4 Influence of the ambient-atmosphere temperature on the strain rate

In Appendix A.1, an estimate of the strain rate in the forward part of the Tsuji flame is obtained as a function of the Froude number Fr, temperatures of burner, ambient-atmosphere and flame along with the position of the flame, according to Equation A.7. Writing it in dimensional form, one finds

$$\left.\frac{d\hat{v}}{d\hat{y}}\right|_{y_f^-} \sim \frac{\Delta^2}{v_f}\frac{\hat{g}}{\hat{u}_b} \tag{11.5}$$

The expression for the estimate of the strain rate echoes the main idea of the present work, i.e., diminishing the strain rate by increasing the ambient-atmosphere temperature, such that Δ^2 decreases while the velocity v_f increases.

As presented in Appendix A.1, for the ambient-atmosphere temperature $\hat{T}_{\infty,c} = (\hat{T}_f - \hat{T}_b)/ln(\hat{T}_f/\hat{T}_b)$, the velocity at the flame is $v_f = 1$, then the strain rate is estimated as

$$\left.\frac{d\hat{v}}{d\hat{y}}\right|_{y_f^-} \sim \frac{\hat{g}}{\hat{u}_b}\frac{\hat{T}_f - \hat{T}_{\infty,c}}{\hat{T}_f}$$

For the cases in which $\hat{T}_\infty > \hat{T}_{\infty,c}$, the velocity $v_f > 1$, then strain rate decreases

$$\left.\frac{d\hat{v}}{d\hat{y}}\right|_{y_f^-} < \frac{\hat{g}}{\hat{u}_b}\frac{\hat{T}_f - \hat{T}_{\infty,c}}{\hat{T}_f}$$

For instance, for $Fr = 1$, $S = 9.5$, $\hat{T}_b = 300K$ and $\hat{T}_\infty = 1200K$, the flame temperature is $\hat{T}_f = 2050K$, the flame position is $y_f^- = -7.4$ (numerical), the velocity at the flame $v(y_f^-)$ is $(0.12,\ 1.74)$ (numerical and Equation A.6, respectively), the stagnation point y_{st} is $(-6.72,\ -4.29)$ (numerical and Equation A.4 , respectively) and the dimensionless strain-rate is $(0.1125,\ 0.2383)$ (numerical and Equation A.7, respectively).

Figure 11.9 - (a) Strain rate at the flame y_f^- and at the stagnation point y_{st} on the negative y axis as a function of several ambient-atmosphere temperatures: $\hat{T}_\infty = (2,\ 2.5,\ 3,\ 3.5,\ 4,\ 4.5,\ 5,\ 5.2)\hat{T}_b$, for which $Pe = 7.83,\ 5.93,\ 5.2,\ 3.6,\ 3,\ 2.22,\ 2.1$ and $\Delta = 0.84,\ 0.79,\ 0.74,\ 0.68,\ 0.63,\ 0.58,\ 0.52,\ 0.5$, respectively. (b) Strain rate at the flame y_f^- as a function of Péclet number. For all cases, $\hat{T}_\infty = 4.5\hat{T}_b$, $Fr = 1$ and $S = 9.5$ are considered.

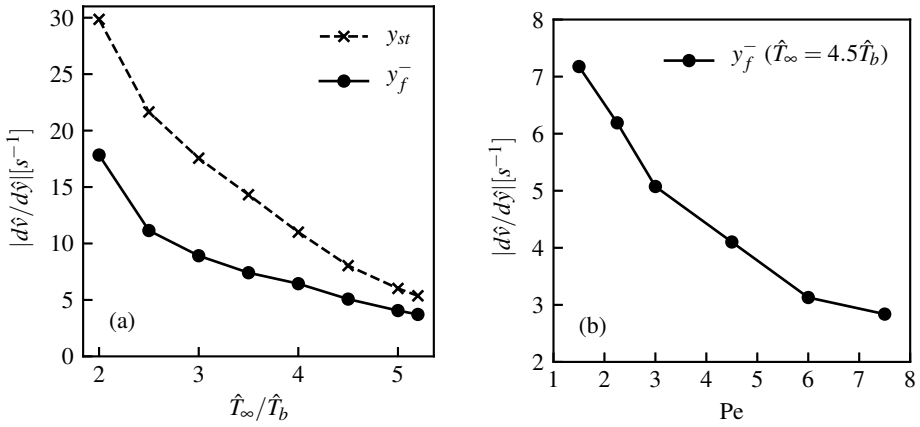

SOURCE: The Author.

Figure 11.10 - (a) flame tip y_f^+ and (b) flame bottom y_f^- as a function of the ration of ambient-atmosphere temperature to burner temperature $\hat{T}_\infty/\hat{T}_b$ ($Fr = 1$, $S = 9.5$).

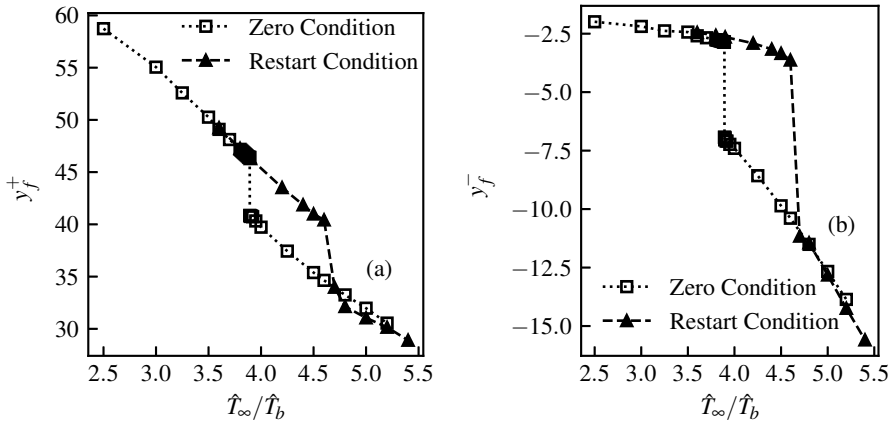

SOURCE: The Author.

The strain rate of the lower stagnation flow around the symmetry axis is influenced by the buoyancy-driven flow. With the increase of the ambient-atmosphere temperature, the positive buoyancy decreases and the buoyancy-driven flow has a lower y-component of the velocity, which results in counterflow flames with a low strain rate. Increasing the ambient temperature from 2 to 5.2 times the burner temperature, the strain rate on the lower counterflow diffusion flame reduces from 16 s^{-1} to 3.5 s^{-1} (see Figure 11.9a). As indicated by Equation 11.5, choosing an ambient temperature of $\hat{T}_\infty = 4.5\hat{T}_b$ and changing the Péclet number by an increase of $\hat{u}_b$, further reduction on the strain rate is achieved, with a minimum value of 2.8 s^{-1}, as shown in Figure 11.9b.

11.5 Dependence of the steady solution on the initial condition

As shown in Figures 11.7d and 11.7e, with changes of the ambient-atmosphere temperature, the flow field changes drastically. Moreover, as shown in Figure 11.10, with changes of the initial conditions, the flow field becomes unexpectedly sensitive to the initial conditions in a certain range of ambient-atmosphere temperature. The two limits of the flame on the y coordinate (flame tip y_f^+ and bottom y_f^-) are used to quantify the effects of the ambient-atmosphere temperature as well as of the initial-conditions on the steady solution, as seen in plots 11.10a and 11.10b, respectively.

Two configurations of initial conditions are considered. The first one is a cylindrical flame starting close to the burner with a uniform flow field, named as zero condition. The second one is a known solution for a different ambient-atmosphere temperature, named as restart condition. If the ambient-atmosphere temperature of the known solution, used as initial condition, is close to the one of the searched new solution, the simulations can be seen as a continuous change on the far field conditions. Using these two types of initial conditions, a jump on the steady solution is identified, but not in the same ambient-atmosphere temperature, according to Figure 11.10. The jump in the solutions shows the strong nonlinearity of the problem and jumps for different ambient-atmosphere temperatures for different initial conditions reveal a hysteresis of the steady solutions.

The results show no initial-conditions dependency in the ranges $2.5 \leq \hat{T}_\infty/\hat{T}_b \leq 3.89$ and $4.6 < \hat{T}_\infty/\hat{T}_b \leq 5.2$. In the first range, the positive buoyancy overwhelms the negative one everywhere and the presence of the burner imposes the establishment of a vortex in the wake of the burner, as discussed previously. In the second range, the negative buoyancy overwhelms the positive one below the burner and a second vortex is established in this region, as discussed previously. However, the balance between the positive and negative buoyancy below the burner for $3.8925 \leq \hat{T}_\infty/\hat{T}_b \leq 4.6$ and the geometric factor imposed by the burner as an immersed body lead to the dependency of the solution on the type of the initial conditions, as exhibited in plots 11.10a and 11.10b.

The drastic change on the solutions at the ambient-atmosphere temperature $\hat{T}_\infty/\hat{T}_b = 4.6$ occurs when the negative buoyancy overwhelms the positive one and vice-versa at the ambient-atmosphere temperatures $\hat{T}_\infty/\hat{T}_b = 3.8925$. For the former case, the cold flow pushes further away the flame from the burner. The descending cold gases flow from the burner and the ascending hot gases flow around the flame create a second recirculation zone (vortex) forward the burner. Once the flow field with two vortices is established, a large decrease of the negative buoyancy is necessary for the flow to return to its previous state (i.e., for flame close to the burner, only one vortex is found and its location is in the burner wake). The condition to the return is found in the latter case, i.e., $\hat{T}_\infty/\hat{T}_b = 3.8925$. The different behavior of the steady solutions for the two used initial conditions in the analyzed range of ambient-atmosphere temperature $2.5 \leq \hat{T}_\infty/\hat{T}_b \leq 5.2$ shows the hysteresis of the buoyancy-driven Tsuji diffusion flame.

12 CASE C: PUFFING TSUJI FLAME

It is evident that the essence of the flickering flame lies in the dynamics of the toroidal vortices (XIA; P.ZHANG, 2018). Several experimental works have reported flickering frequencies that presents the toroidal structures and remain independent of the Reynolds number, the burner geometry and of the fuel considered, at least while the flow remains laminar (SATO et al., 2000). This means that the Strouhal-Froude number correlation, $St \propto Fr^{-1}$, viewed as a scaling law for the frequency of the puffing flames must be valid for different geometries, such as jet diffusion flames or pool flames. This scaling law is equivalent to the Frequency-fuel injection diameter correlation, $f \propto (g/D)^{1/2}$. The lack of dependency of frequency from the fuel injection geometry is valid mainly for the cases in which buoyancy dominates over the jet flow.

The Tsuji geometry, has some main features that greatly differs of the geometries cited above. One of them is the formation of a tubular vortices array, instead of toroidal vortices structures found in the axisymmetrical geometries cited above. From the rectangular symmetry employed in the present numerical study, the tubular vortices has infinite length, then the vortical structure in the Tsuji burner has a two-dimensional configuration. Another feature is the existence of a counterflow diffusion flame in the upstream region of the burner when the envelope flame configuration is found. The envelope flame regime is found by the analysis of two properties, $\hat{k}_s$ and $-f_w$, the flame stretch rate and fuel-ejection rate, respectively (TSA; CHEN, 2003). The flame stretch rate is defined as $\hat{k}_s = 2\hat{u}_\infty/\hat{R}$ by Tsuji and Yamaoka (1967) and the fuel-ejection rate $-f_w$ is defined in Section 8.4 as introduced by Chen and WENG (1990). The parameter $\hat{u}_\infty$ is the oxidiser velocity approaching the cylinder from upstream.

For preventing the blow-off and changing the regime from envelope flame to wake flame, the pair *Re-Fr* must be sufficiently low. This constrain rises a disparity of length scales at the problem, e.g., when the counterflow region is well described by the characteristics parameters, the flame tip and/or puffing formation region far downstream is not well described. This multi-scale problem is dealt in part by the non-uniform computational mesh showed in Figure 12.1.

In terms of the grid, Case C is considered the most critical of the three by its dynamic and interactions in multiple scales. Then for the grid independence study, different mesh sizes have been tested as shown in Figure 12.1. For all considered meshes, the refinement parameters retain the same pattern of distribution of the grid points.

Figure 12.1 - Non-uniform structured coarse and fine meshes for the puffing Tsuji flame case with the burner located at $(x, y) = (0, 0)$, not shown here.

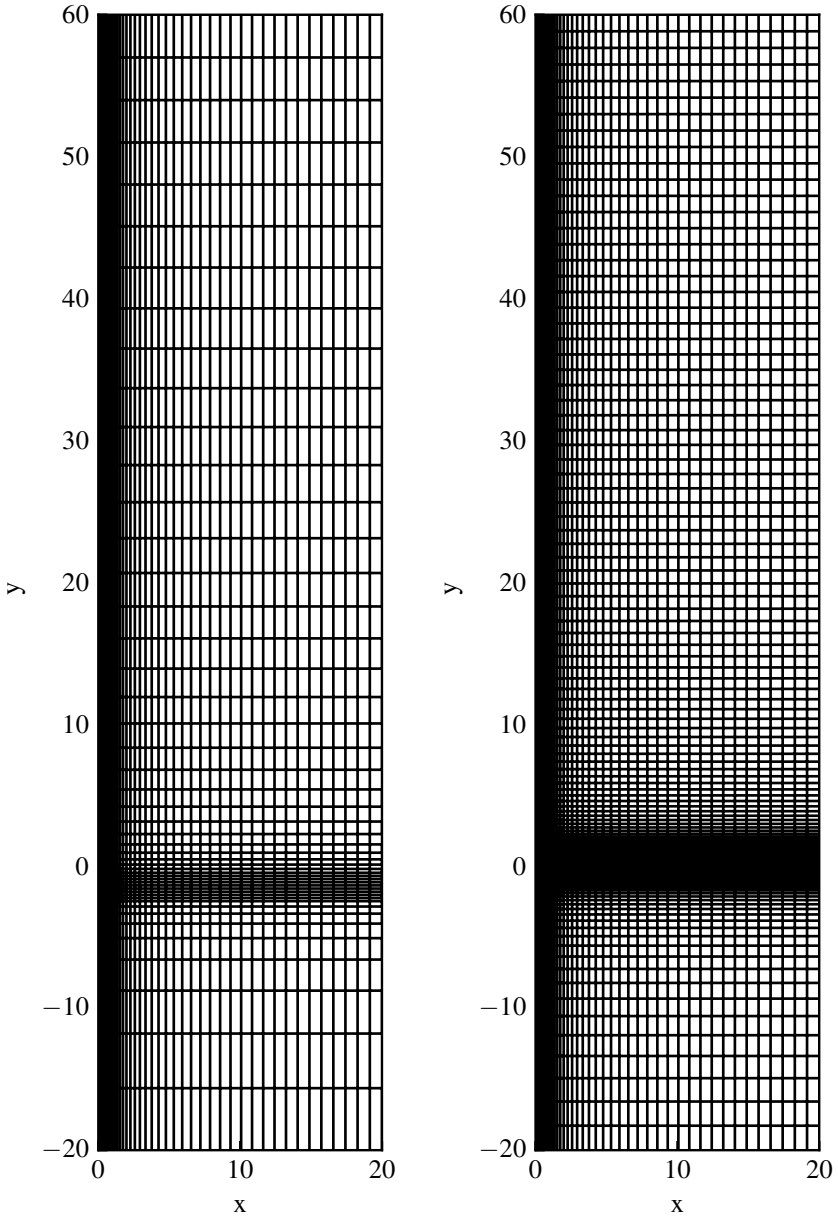

SOURCE: The Author.

The variations of temperature along the symmetry line and the flame position ($Z = 1$) for four different mesh sizes are shown in Figure 12.2. As is seen from the figure, there is very little difference between the results of the coarser grid and the finest one. This confirms the small dependence of the results on the mesh size, so an

intermediate size was selected.

Figure 12.2 - (a) flame position and (b) temperature distribution at the symmetry axis for time $t = 0.1s$ and burner size $d = 5mm$.

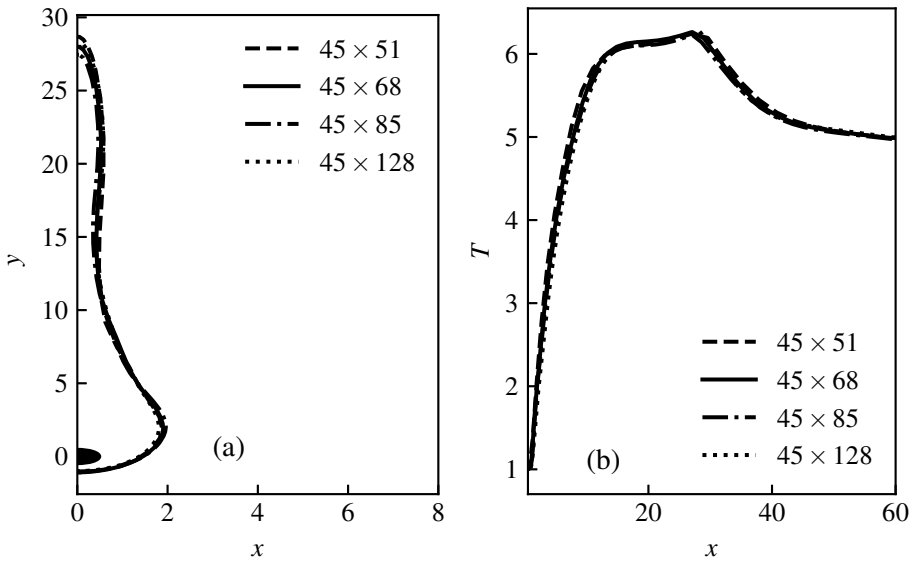

SOURCE: The Author.

For Case C, the burner is composed by a circular cylinder with different diameters and fuel injection, $\hat{L}_c \equiv \hat{d}_b = (0.40,\ 0.45,\ 0.50,\ 0.55,\ 0.60) \times 10^{-2}m$ and $\hat{v}_b = (0.159,\ 0.141,\ 0.127,\ 0.116,\ 0.100) \times 10^{-2}m/s$, respectively. The fuel is methane diluted by 20%, $Y_{F_c} \equiv Y_{F_b} = 0.2$ to prevent long flames as observed in Cases A and B. The resulted Reynolds number, Péclet number and Froude number for this case are $Re = 40$, $Pe = 28.4$, and $Fr = (0.8, 0.67, 0.57, 0.5, 0.43)$. Also, Figure 8.13 shows the following boundary conditions: on the top ($y = \hat{y}/\hat{r} = 40$) and right ($x = \hat{x}/\hat{r} = 10$) boundaries, free-slip condition is imposed for velocities along with zero fluxes for the temperature, mixture fraction and excess enthalpy. At the inlet section located at ($y = \hat{y}/\hat{r} = 0$), a prescribed velocity streamwise component for fuel and air, $v(x \leq 1) = \hat{v}_F/\hat{v}_c = 0.66$ and $v(x < 1) = v_a ir/v_c = 1$, respectively.

12.1 Vorticity generation

The results obtained using the constant density code are illustrated by Figure 12.3 which displays the mass fraction isocontours and vorticity contours. Starting from the initial conditions, the flow field is experiencing:

- A transient phase ($0 \leq t \leq 30$) characterized by the generation of a finite number of vortical tubular structures which are growing while being convected upwards (See in Figure 12.3b to Figure 12.3j, the bulged and rolled contour regions). These vortices are generated by buoyancy-driven shear flow, close to the burner, when the flame is progressively adapting its shape from the initial condition. The instability stops as soon as the last generated vortex structures leaves the computational domain (Figure 12.3j).

- A (non-physical) steady state ($t > 30$) characterized by the absence of any puffing and related vortical structures.

Figure 12.3 - **CONSTANT DENSITY CASE:** Mass fraction contours of several times with $Re = 40$ and $Fr = 0.8$. (a) $t = 3$, (b) $t = 6$, (c) $t = 9$, (d) $t = 12$, (e) $t = 15$, (f) $t = 18$, (g) $t = 21$, (h) $t = 24$, (i) $t = 27$, (j) $t = 30$, (l) $t = 33$ and (m) $t = 43$. Lines represent 10 contours between Y_{Fb}(dashed line) and $Y_{O\infty}$(continuous line). The contours represent the dimensionless vorticity defined as $\omega = \partial_x v - \partial_y u$. The gray area represents the cylindrical burner.

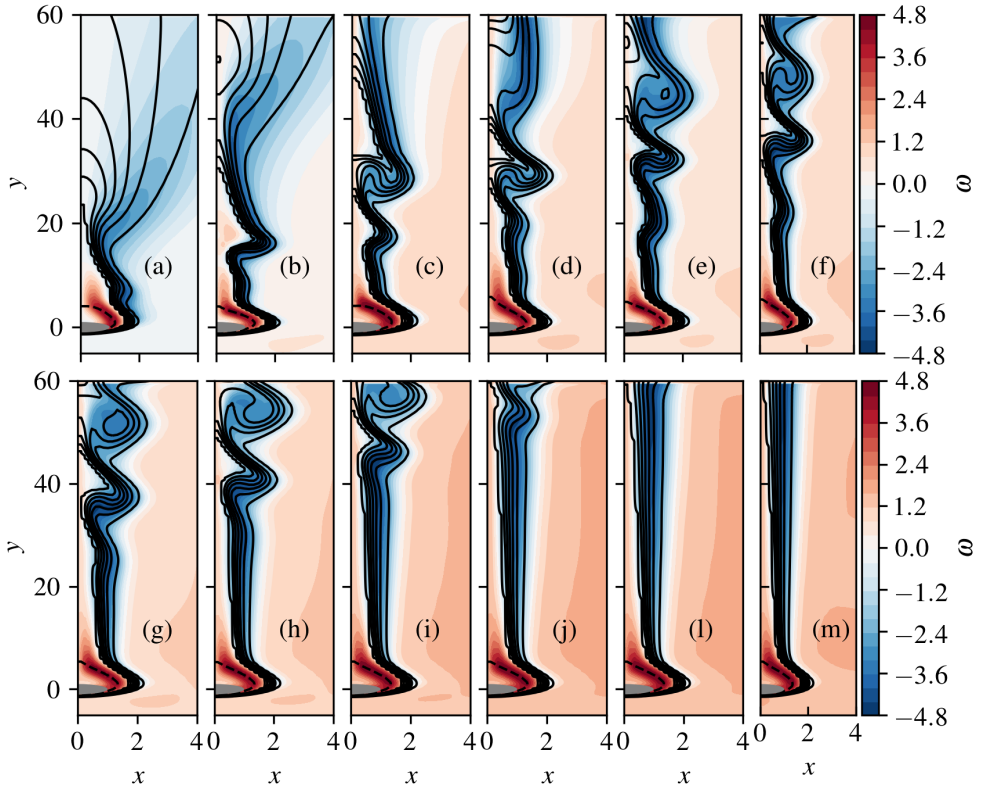

SOURCE: The Author.

Here, it can be guessed that due to the absence of density gradient related vorticity sources (constant density hypothesis) and vortex stretching mechanism (two-dimensional flow), the dynamics of the flow leading to the puffing regime cannot be sustained beyond the observed transient period.

An in-depth analysis of the vorticity governing equation, one can find the key role of each term:

$$\frac{D\omega}{Dt} = (\omega \cdot \nabla)\mathbf{u} - \omega(\nabla \cdot \mathbf{u}) + \frac{1}{\rho^2}(\nabla\rho \times \nabla p) + \nabla \times \frac{1}{\rho Fr^2}(1-\rho)\mathbf{e}_y + \frac{1}{\rho Re}\nabla^2\omega \quad (12.1)$$

where ω is the vorticity vector and is defined as $\omega = \partial_x \mathrm{v} - \partial_y u$.

The term on the left-hand side describes the rate of change of vorticity of the moving fluid particle and is characterized by the material derivative D/Dt. The definitions of right-hand side terms are:

- The first term is responsible for the vortex tilting or stretching and vanishes for either two-dimensional flows or axisymmetric flows without swirling.

- The second term is referenced as a dilatation term. This term is responsible for the stretching of vorticity due to flow compressibility and vanishes for incompressible flows.

- The third and fourth terms are defined as the baroclinic and gravitational terms, respectively. Both terms are responsible for the vorticity generation and require the presence of variable density.

- The fifth term is the diffusion term and is responsible for the redistribution of vorticity due to viscous effects.

Then, the third and fourth terms on the right-hand side of Equation 12.1, are responsible for sustaining the puffing phenomenon. To prove the importance of the variable density, the same case showed in Figure 12.3 was redone with the Zero-Mach Compressibility Method Code. The same nondimensional times are analyzed in Figure 12.4 and confirmed that the steady-state phase that appears in an incompressible framework was a non-physical one.

Figure 12.4 - **VARIABLE DENSITY CASE:** Mass fraction contours of several times with $Re = 40$ and $Fr = 0.8$. (a) $t = 3$, (b) $t = 6$, (c) $t = 9$, (d) $t = 12$, (e) $t = 15$, (f) $t = 18$, (g) $t = 21$, (h) $t = 24$, (i) $t = 27$, (j) $t = 30$, (l) $t = 33$ and (m) $t = 43$. Lines represent 10 contours between Y_{Fb}(dashed line) and $Y_{O\infty}$(continuous line). The contours represent the dimensionless vorticity defined as $\omega = \partial_x v - \partial_y u$. The gray area represents the cylindrical burner.

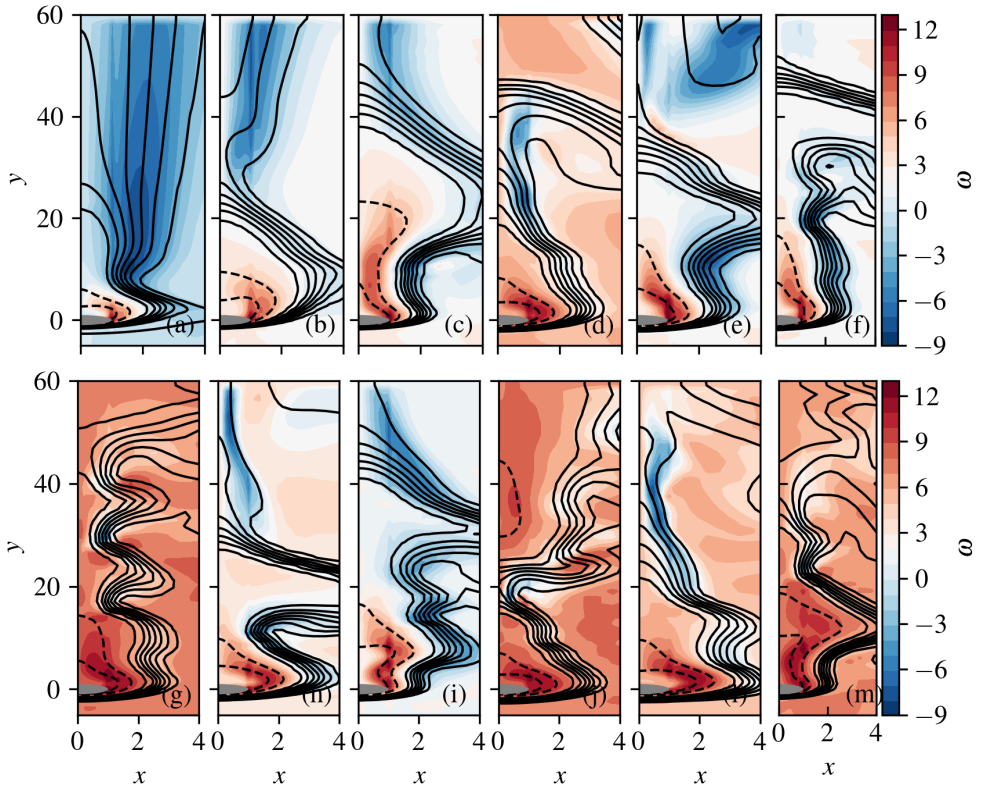

SOURCE: The Author.

Some key differences between the constant and variable density cases, Figures 12.3 and 12.4, respectively, can be spotted by analysing the distribution of vorticity. First, the vorticity magnitude outside the flame (oxidant part) for the constant density case remains constant ($\omega \sim 1.2$) for the most part of the flow, while in the variable density case the vorticity magnitude in this region varies between $\omega \approx 1$ and 6. This is consequence of the relation of the detachment of the puffing and the entrainment. By the mass conservation, each time the pocket of hot gas leaves the domain, a fresh oxidant stream is being carried from the sides. This mechanism obligates the entrainment velocity generated by the suction of ambient oxidant to varies on time, i.e. the entrainment variation is periodic and the frequency following that of the

puffing.

12.2 Puffing frequency

The frequencies of the Tsuji puffing flame was analysed by the case with a lower Froude number Fr than the previous case, changing from $Fr = 0.80$ to 0.43. This parameter was achieved by varying the diameter of the burner from $d = 4$ to $6 \times 10^{-3}m$, while varying $\hat{u}_b$ to achieve the same Re and Pe of 40 and 28.4, respectively. The flame evolution between $t = 1.3s$ and $t = 1.52s$ is illustrated by Figure 12.5 which displays the temperatures isocontours and dimensional vorticity contours.

Qualitative comparison with coflow jet flame for the case shown in Figure 12.5, highlights:

- Contrarily to coflow in which the generated vortex is in confined domain, in an unconfined one the vortex grows as is convected;
- Smaller structures for the coflow jet flame case with small fingers and/or mushrooms tips;
- In both cases, the red isoline that represents the flame ($Z = Z_{st}$) shows the break of the stoichiometric surface in two regions. The first one establishes the main flame and remains attached to the cylindrical burner. The second region is composed of a pocket of hot gas surrounded by a flame that moves downstream and disappears when the fuel inside the pocket is consumed. This event is exhibited in Figure 12.5.

Figure 12.6 shows in more detail the contribution of each source term in the vorticity equation for a snapshot at $\hat{t} = 1.505s$. The vorticity source term contours that represents the gravitational contribution to the generation of vorticity is shown in Figure 12.6b. By the 2D nature of the problem, the gravitational/buoyant source term becomes dependent on the gradient of density in the x-direction only. So, as shown in Figure 12.6b, the maximum/minimum value of this term is around the flame sheet and mainly when it is parallel to the y-direction.

Figure 12.5 - (a) $\hat{t} = 1.443s$, (b) $\hat{t} = 1.464s$, (c) $\hat{t} = 1.484s$, (d) $\hat{t} = 1.505s$, (e) $\hat{t} = 1.525s$, (f) $\hat{t} = 1.546s$. The red isoline represents the flame sheet ($Z = 1$).

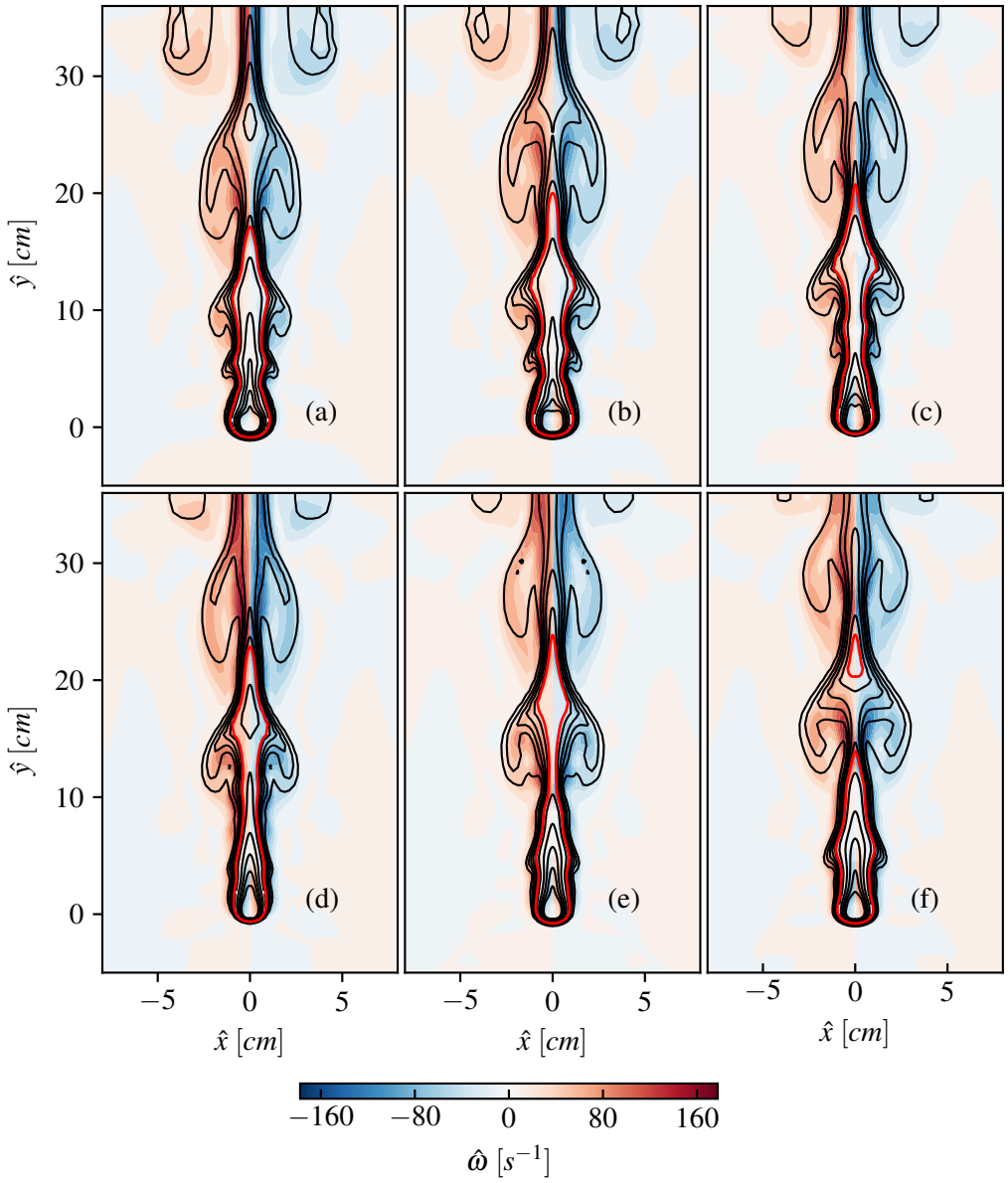

SOURCE: The Author.

Figure 12.6 - (a) Is the vorticity, (b) is the vorticity source term $\nabla \times 1/(\rho Fr^2)(1-\rho)\mathbf{e}$ and (c) is the source term $\nabla\rho \times \nabla p$ for the snapshot (d) in Figure 12.5, $t = 1.505s$. The results are at the axis x mirrored for better visualization only. And the continuous line represents the flame, is the isoline $Z(x, y) = 1$.

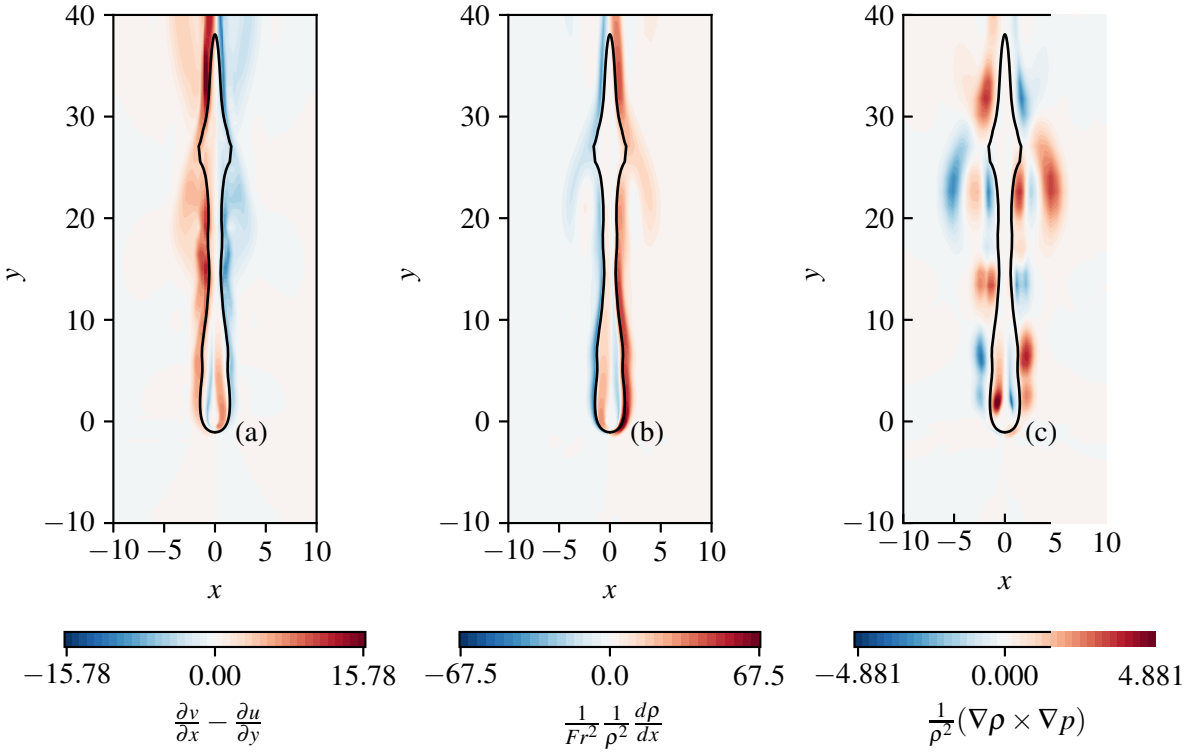

SOURCE: The Author.

The contours of the so-called baroclinic source term is presented in Figure 12.6c. As this source term depends on the pressure field and not only the density gradient, its maximum/minimum values does not correspond to the gravitational source term, Figure 12.6b. Then the distribution of the baroclinic term is not restricted to the surrounding of the flame sheet, but is encountered also at the vortex structure. Another key difference from the gravitational term, is that the baroclinic term presents an intermittent value in the y-direction around the flame, showing the presence of perturbations with a higher wavenumber. It is important to notice that the level of contribution of the gravitational term to the generation of vorticity is one order of magnitude higher than the contribution of the baroclinic term.

Figure 12.7 shows the temperature contours and flame sheet for the snapshot (d) in

Figure 12.5. The black line represents the y-plane at $x = 0.8$, the red $\times$ marker represents the location of the probe to analyse the time history of a certain variable, and the yellow rectangles represent the different regions of interest in the wavenumber analysis.

Figure 12.7 - Temperature contours with the y-plane located at $x = 0.8$ and the regions of interest.

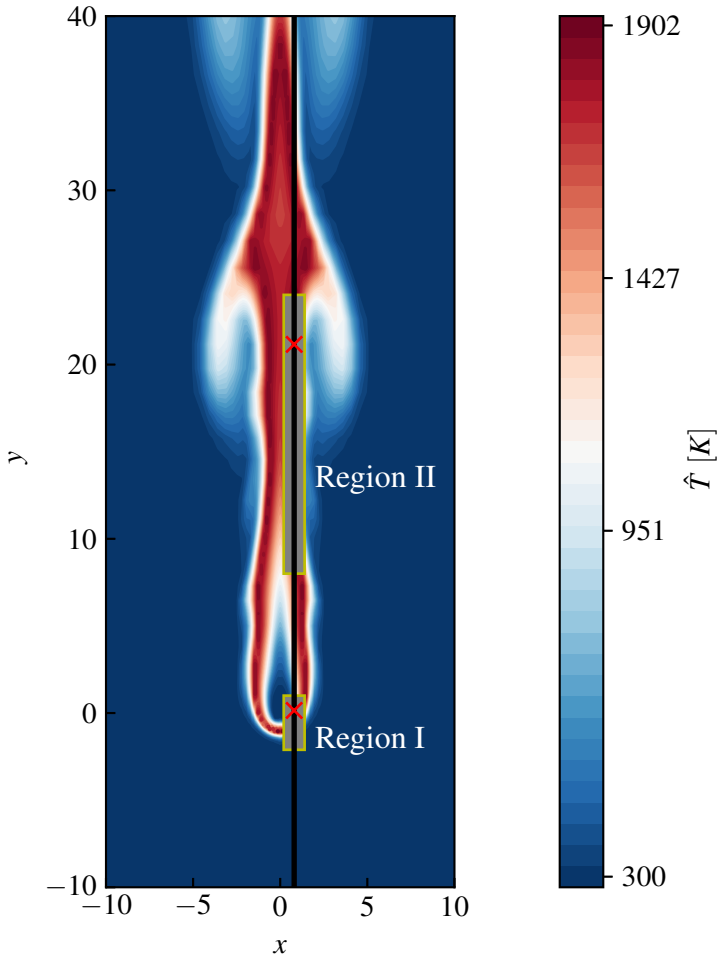

SOURCE: The Author.

Figure 12.8 shows the baroclinic source term distribution along the $(0.8, y)$ plane. This distribution is divided by two regions of interest. The first, Region I, is close to the burner and presents the small wavelengths section, the second, Region II, is far downstream the burner and presents the large wavelengths section.

Figure 12.8 - Baroclinic source term distribution at a y-plane located at $x = 0.8$ for the snapshot (c) in Figure 12.6, $\hat{t} = 1.505s$.

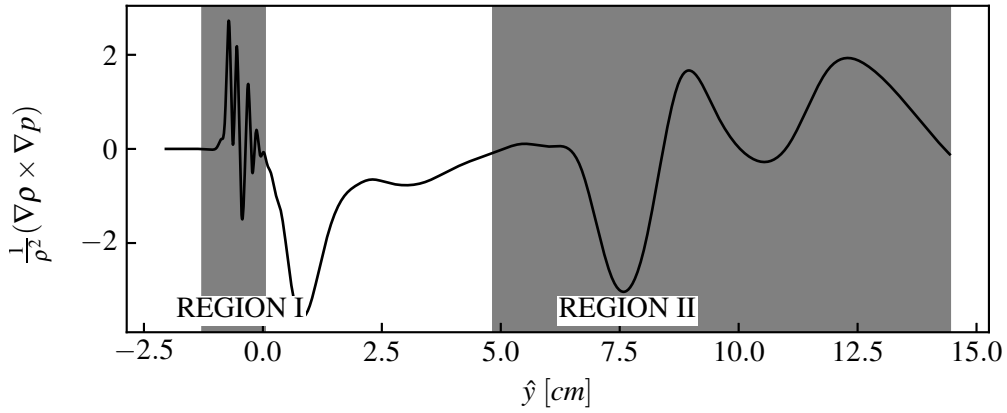

SOURCE: The Author.

Figure 12.9a presents the spatial behaviour of the baroclinic term for the Region I repeated eight times to enable the Fast Fourier Transform - FFT of the data. Defining the wavelength, λ, as the reciprocal of the wavenumber, k_c, from the power spectrum, Figure 12.9, one can find the wavelength of $\hat{\lambda} = 0.119 \times 10^{-2}m$ for the Region I from the dominant wavenumber. The other picks at the power spectrum represent the frequency of repetition of Region I, then is not a valuable result for the analysis of the perturbation frequency in the source terms. That is, they are frequencies that issue from the choice of analysis. This wavelength for the Region I indicates a high-frequency perturbation around the cylinder, initiated mainly by the interaction of the fuel injection and the inertial flow generated by the positive buoyancy of the flame.

In the same way, Figure 12.9c presents the spatial evolution of the baroclinic term for the Region II repeated eight times. As in the analysis of Region I, here, the first wavenumber at the power spectrum was not chosen to represent the perturbation of the source term. Again, from the power spectrum, Figure 12.9d, the resulting wavelength from the second wavenumber is $\hat{\lambda} = 3.94 \times 10^{-2}m$. This wavelength indicates a low frequency regime at the Region II. This is mainly generated by the interaction of the buoyant flow generated along the flame and the low temperature far-wake.

Figure 12.9 - (a) The baroclinic vorticity source term repeated spatial history (REGION I) at $x = 0.8$, (b) power spectrum for the term value fluctuation, $\hat{\lambda}_I = 0.119cm$, (c) The baroclinic vorticity source term repeated spatial history (REGION II) at $x = 0.8$, and (d) power spectrum for the term value fluctuation, $\hat{\lambda}_{II} = 3.95cm$.

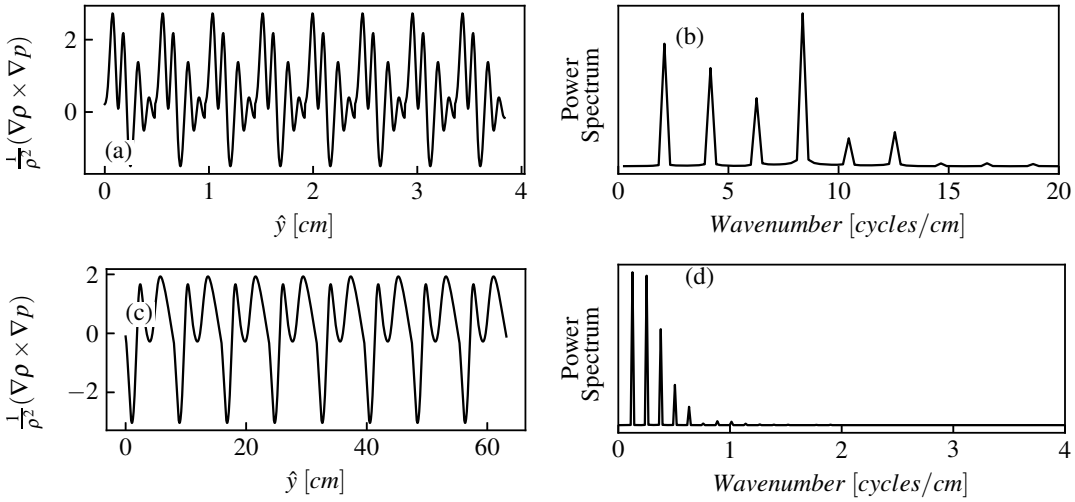

SOURCE: The Author.

The spatial analysis at a snapshot showed the wavenumber in different regions and gave a hint about the transient behaviour that arises from these fluctuations on the source terms of vorticity. The transient history of the source terms of Equation 12.1 are presented in Figure 12.10 and 12.11. The probe location is represented by the red $\times$ markers in Figure 12.7.

The unsteady behaviour of the vorticity source terms at different regions of the domain is compared in Figures 12.10 and 12.11. The unsteady frequency was obtained by performing a Fast Fourier Transform (FFT) of the signals in Figure 12.10a and c, that showed the time history for the baroclinic source term. Coherently with the above results of the wavelength, Region I presented a higher frequency than the one observed in Region II. The probe at Region I does not show a regular pattern of the fluctuations. The frequency extracted from the power spectrum, Figure12.10b, presented a dominant value at $\hat{f} = 9.25Hz$. This frequency is related to an instability of the Kelvin-Helmholtz type that arises from the flow field with inflection point resulting of the interaction from the cylinder fuel injection and the oxidant stream created by the buoyant forces.

At Region II, the dominant frequency value from Figure 12.10d is $\hat{f} = 4.89Hz$. In contrast to Region I, this frequency is related to a Rayleigh-Taylor type instability that arises from the interaction of the interface of different densities created at the large flame bulge. At Region II, fingers are found to grow from the flame interface and mushroom patterns are formed, in line with the structures formed in a Rayleigh-Taylor instability, as seen in Figure 12.5.

Figure 12.10 - (a) The baroclinic vorticity source term time history at $(x, y) = (0.8, 0.15)$, (b) power spectrum for the term value fluctuation, $\hat{f} = 9.25Hz$, (c) The baroclinic vorticity source term time history at $(x, y) = (0.8, 21.16)$, and (d) power spectrum for the term value fluctuation, $\hat{f} = 4.89Hz$.

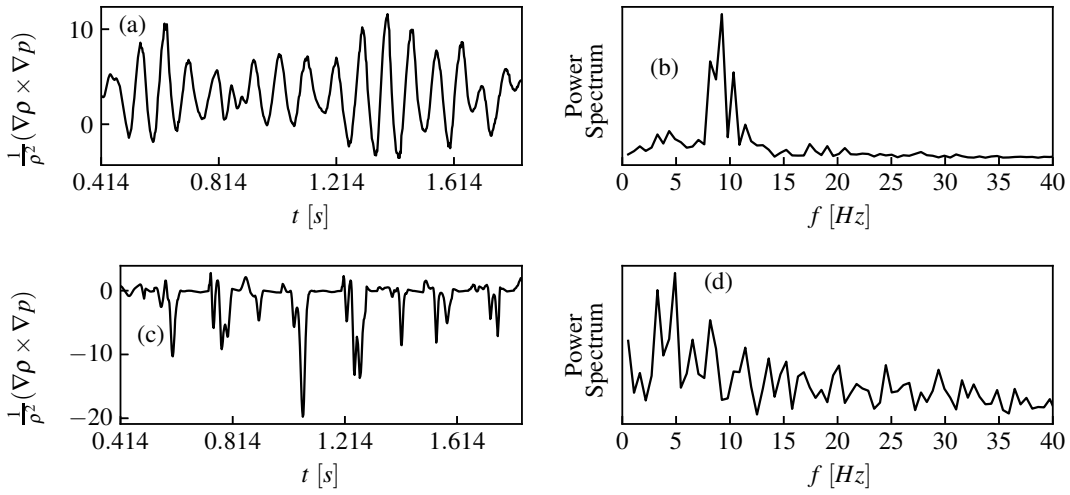

SOURCE: The Author.

Another feature that can be emphasised by the two regions is the difference in phase velocity v_λ. This velocity represents the rate at which a wave propagates through space, and is related to the wavelength λ and the frequency $\hat{f}$ or even the Strouhal number St for a non-dimensional analysis. Thus, with the information about the wavelength and frequency, it is possible to obtain the wave phase velocity in the two regions previously studied, leading to v_{λ_I} and $v_{\lambda_{II}}$. The results of the spatial and temporal analysis shows that the wave phase velocity is $v_{\lambda I} = \lambda_I \times f_I = 1.1$ and $v_{\lambda II} = \lambda_{II} \times f_{II} = 19.31$. The cusp velocity at the flame surface in region I and the puffing vortex velocity in region II can be related to the perturbation of the source terms of the vorticity equation.

Figure 12.11 - (a) The density vorticity source term history at $(x, y) = (0.80, 0.15)$, (b) power spectrum for the term value fluctuation, $\hat{f} = 9.25Hz$, (c) The density vorticity source term history at $(x, y) = (0.8, 21.16)$, (d) power spectrum for the term value fluctuation, $\hat{f} = 4.89Hz$.

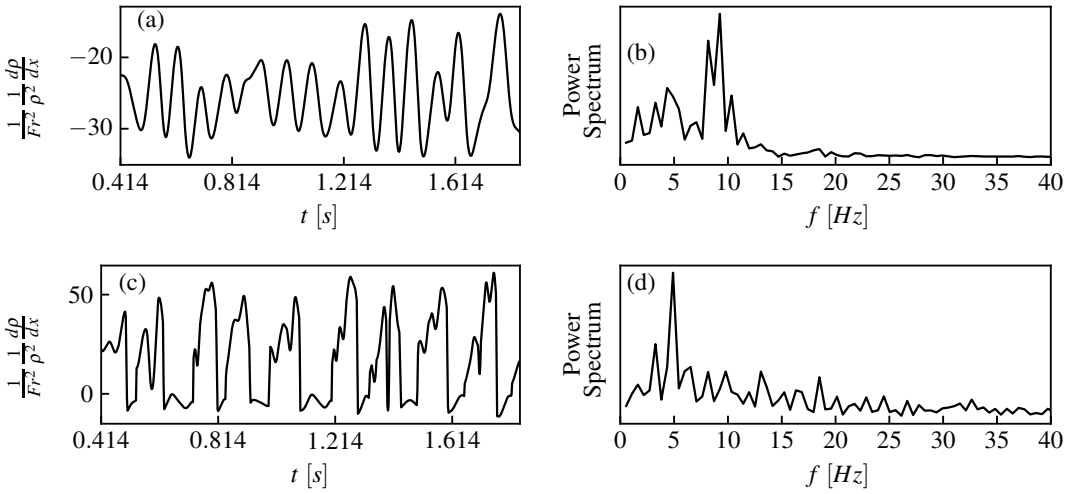

SOURCE: The Author.

Figure 12.12 indicates the source of the "merging" process of the flame bulge. This process is observed when a flame bulge moves up and outward (as seen in plot (a) and (b)) and its displacement velocity slows down (as seen in plots (c) and (d), allowing the next flame bulge to catch up. As a result, the preceding flame bulge interacts with the trailing one. The process occurred at every other flame bulge established near the Tsuji burner and when the entrainment becomes weak.

Figure 12.12 - (a) and (b) is the vortex's core positions x_λ and y_λ between the times $\hat{t} = 0.68s$ and $0.92s$, (c) is the vortex's core velocity v_λ and (c) is the vortex's core acceleration a_λ, both from minimum and maximum y_λ position.

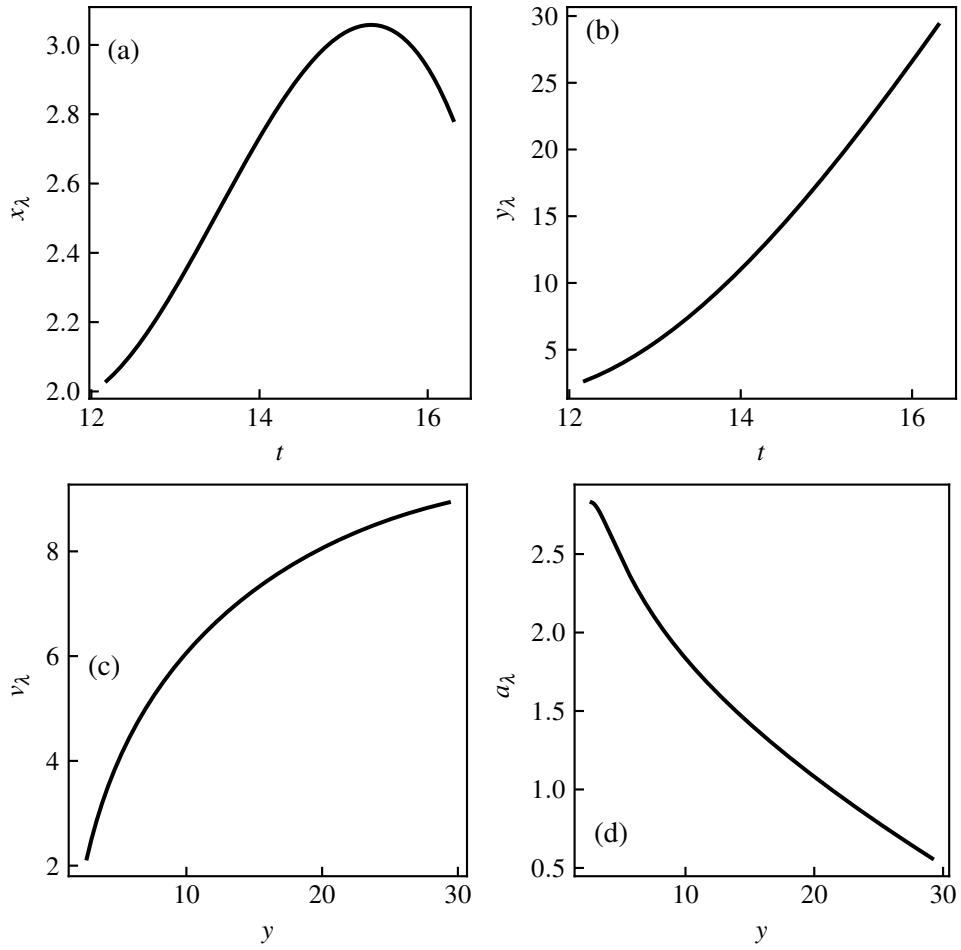

SOURCE: The Author.

12.3 Tsuji flame vs. jet and pool flames

Puffing frequencies which were analysed by FFT at various buoyancy levels were summarized using a relation between the Strouhal number, St, and the Froude number, Fr. As defined in Section 4.2, these dimensionless numbers are

$$St = \frac{\hat{f}\hat{L}_c}{\hat{v}_c}, \qquad Fr = \frac{\hat{v}_c}{\sqrt{\hat{g}\hat{L}_c}}$$

The range of the Froude numbers in the numerical experiment was $0.4 < Fr < 0.8$.

The selection of this narrow range prevents the transition from one type of puffing to another. The parameters of these cases are chosen so that Fr changes while Re and Pe remain constant.

The probe for $(x, y) = (0.80, 0.15)$ shows the same $St \approx 0.6687$. This behaviour indicates that the instability at Region I is closely linked with the Inertial effect by the Reynolds number. Keeping the Re number constant prevented the change in the shear stream generated between the fuel injection and the oxidant, and with that, the change in the instability frequency.

Figure 12.13 shows the change on Strouhal number at the probe located in $(x, y) = (0.8, 21.16)$. As stated before, the frequency of the oscillation is relatively insensitive to fuel velocity, fuel type, and diameter of the burner for a jet or pool flame. However, the magnitude of the flame puffing does depend on geometrical parameters. In the present case, the vortex does not present a toroidal geometry like jet flames, but an infinite tubular geometry. The geometry changes the frequency level, but keeps the dependence of Strouhal number by the Froude number. This consideration seems to be reasonable since the present result of $St = 0.1Fr^{-1.12}$ was close to the relation $St \propto Fr^{-1}$ reportedly by Sato et al. (2000).

Figure 12.13 - Comparison between the empirical equation from Sato et al. (2000) and the numerical results.

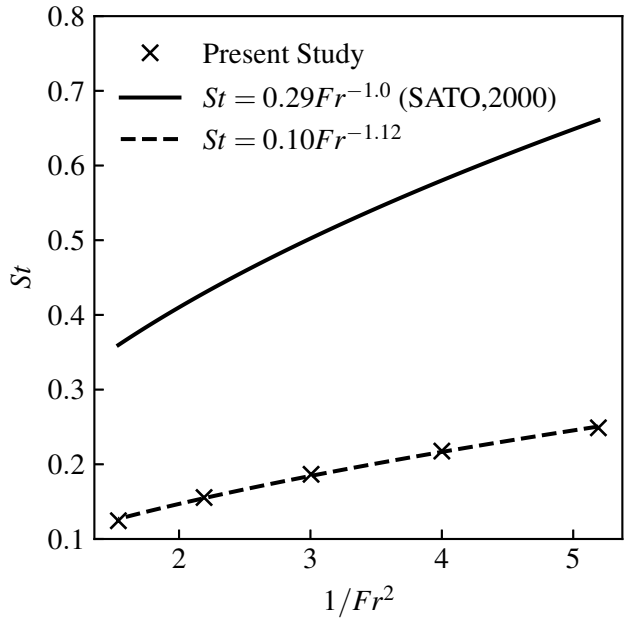

SOURCE: The Author.

13 CONCLUSIONS AND PERSPECTIVES

This work investigates the Tsuji Burner along with the implementation of the unsteady artificial compressibility approach in the limit of a zero Mach number. The resulting numerical code has been used to simulate the Tsuji Burner in three main cases: steady Tsuji flame with forced convection, namely Classical Tsuji flame (Case A), steady Tsuji flame with natural convection with heated ambient atmosphere, namely Buoyant Tsuji Flame (Case B), and finally the unsteady Tsuji flame with natural convection at low Froude number, namely Puffing Tsuji Flame (Case C).

Case A: Classical Tsuji Flame

In this case, the whole (forward and backward) Tsuji flame under forced convection is analysed. Due to the very large flame height, the flame shape in the upper part is slightly dependent on the lower part of the flame, close to the burner. Then, an asymptotic analysis of the flame far from the burner provides a good description of the flame shape and the characteristic length scales of the problem. The flame width is directly proportional to the stoichiometric coefficient and reciprocal of free stream velocity the 3/4 power and Peclet number the 1/4 power. The flame height is proportional to the square of the stoichiometric coefficient and to the square root of the ratio of Peclet number to free stream velocity. The numerical results from potential flow as well as the Navier-Stokes flow confirm those dependence on the problem parameters. Also, it is seen that the description of the lower part of the flame, despite its small influence, as done by Navier-Stokes flow, is essential to determine the flame height. Because of the fuel convective transport to the flame in that region, the consumption is higher, which imposes the flame height.

Case B: Buoyant Tsuji Flame

The aim of the present case was to investigate the possibility of reduction of the strain rate in Tsuji flames by varying the temperature of the ambient atmosphere. The model of this case considers the thermal expansion only in the buoyant force term of the Navier-Stokes equations. The variation of the ambient-atmosphere temperature modifies simultaneously the positive buoyancy of the hot gases and the negative one of the cold gases. Then, the reduction of the effects of the buoyancy on the whole flame established around the horizontal cylindrical porous burner is achieved by a proper combination of those two forces. For the cases in which the positive buoyancy overwhelms the negative one, the lower part of the Tsuji flame is close to the burner, the length of the upper part of the flame is about two order of

magnitude of the burner radius. In the flow field, there is one vortex in the wake of the burner. For the cases in which the negative buoyancy overwhelms the positive one, the lower part of the flame is farther from the burner, and the length of the upper part of the flame is reduced considerably. The flow field changes drastically because, besides the vortex in the burner wake, a second vortex is established below the burner. The systematic increase in the ambient-atmosphere temperature modifies not only the intensity of the buoyant forces, but also the domain in which each of them is found. Because of the change in these two properties with the ambient-atmosphere temperature, the transition of the negative buoyancy overwhelming the positive one and vice-versa are discontinuous. Moreover, since the flow fields for these two conditions are very different, then the ambient-atmosphere temperatures for the transitions are not the same. This behaviour causes a hysteresis on the buoyancy-driven Tsuji diffusion flame. The numerical results point out that the strategy of increasing the ambient-atmosphere temperature leads to low-strain-rate Tsuji diffusion flames.

Case C: Puffing Tsuji Flame

This case explores the buoyant Tsuji flame with low Froude number, a configuration that in some cases enables the appearance of puffing flames. Also, this case investigates the influence of the hypothesis of constant-density flow in the formation of an unsteady flame. The results showed that the low-frequency instability generated by the displacement of the flame's initial condition was damped and led ultimately to a non-physical stationary diffusion flame with constant density. This is attributed to the absence of vorticity source terms related to the underlying constant density assumption.

The mechanisms leading to the formation and transport of vortical structures in buoyant reactive flows were investigated by examining the vorticity transport equation. It was found that combustion-induced buoyancy generates large vortical structures in the plume near field mainly because of the gravitational term, which is due to the interaction between the gravity and the transverse density gradients. This generates a low-frequency puffing that is related to the Rayleigh-Taylor instability. Then, a transverse density inhomogeneity subjected to gravity is essential to the development of buoyancy instability in reactive flows. By the inspection of the temporal behaviour of the source terms of vorticity equation, another frequency was found. This frequency is related to the Kelvin-Helmholtz instability and was established in the region near the cylindrical burner. Finally, a parametric study varying

the Froude number showed that the puffing regime for Tsuji flames follows the same relationship as for jet flames, $St \propto Fr^{-1}$. However, it was found that the frequency level of the puffing Tsuji flames is not the same as reported in the literature for jet and pool flames.

REFERENCES

AZARKHAVARANI, M. F.; LESSANI, B.; TABEJAMAAT, S. Artificial compressibility method on half-staggered grid for laminar radiative diffusion flames in axisymmetric coordinates. **Numerical Heat Transfer, Part B: Fundamentals**, v. 72, n. 5, p. 392–407, 2017. 30

BASSI, F.; MASSA, F.; BOTTI, L.; COLOMBO, A. Artificial compressibility godunov fluxes for variable density incompressible flows. **Computers & Fluids**, v. 169, p. 186–200, 2018. 30

BIANCHIN, R. P.; DONINI, M. S.; CRISTALDO, C. F. C.; FACHINI, F. F. On stationary diffusion flames established around a cylindrical burner subject to forced convection. **Proceedings of Combustion Institute**, v. 37, p. 1903–1910, 2019. 8, 30, 76, 78, 79

BONNE, U. Radiative extinguishment of diffusion flames at zero gravity. **Combustion Flame**, v. 16, p. 147–159, 1971. 8

BRUEL, P.; KARMEO, O.; CHAMPION, M. A pseudo-compressibility method for reactive flows at zero mach number. **International Journal of Computational Fluid Dynamics**, v. 7, p. 291–310, 1996. 28, 30, 54

BUCKMASTER, J.; LUDFORD, G. **Theory of laminar flames**. [S.l.]: Cambridge University Press, 1982. 9

BUCKMASTER, J. D.; PETERS, N. The infinite candle and its stability - a paradigm for flickering diffusion flames. **Symposium (International) on Combustion**, v. 21, p. 1829–1836, 1986. 13, 14

CARPIO, J.; SáNCHEZ-SANZ, M.; FERNÁNDEZ-TARRAZO, E. Pinch-off in forced and non-forced, buoyant laminar jet diffusion flames. **Combustion Flame**, v. 159, p. 161–169, 2012. 14

CARSLAW, H. S.; JAEGER, J. C. **Conduction of heat in solids**. [S.l.], 1959. 69

CHAMBERLIN, D. S.; ROSE, A. The flicker of luminous flames. **Industrial and Engineering Chemistry**, v. 20, p. 1013–1016, 1928. 13

CHANG, J.; KWAK, D. On the method of pseudo compressibility for numerically solving incompressible flows. In: 22ND AEROSPACE SCIENCES MEETING. **AIAA Meeting Paper**. [S.l.], 1984. p. 252. xvi, 28, 29, 54

CHEN, C.-H.; WENG, F.-B. Flame stabilization and blowoff over a porous cylinder. **Combustion Science and Technology**, v. 73, n. 1-3, p. 427–446, 1990. 9, 89

CHEN, L. D.; ROQUEMORE, W. M. Visualization of jet flames. **Combustion Flame**, v. 66, p. 81–86, 1986. 13

CHEN, L. D.; SEARA, J. P.; ROQUEMORE, W. M.; GOSS, L. P. Buoyant diffusion flames. **Symposium (International) on Combustion**, v. 22, p. 677–684, 1988. 13, 58, 59

CHEN, L. D.; VILIMPOC, V.; GOSS, L. P.; DAVIS, R. W.; MOORE, E. F.; ROQUEMORE, W. M. Time evolution of a buoyant jet diffusion flame. **Symposium (International) on Combustion**, v. 24, p. 303–310, 1992. 14

CHORIN, A. A numerical method for solving incompressible viscous flow problems. **Journal of Computational Physics**, v. 2, p. 12–26, 1967. 28

CORVELLEC, C.; BRUEL, P.; SABEL'NIKOV, V. A time-accurate scheme for the calculations of unsteady reactive flows at low mach number. **International Journal for Numerical Methods in Fluids**, v. 29, p. 207–227, 1999. 27, 28, 30

DAVIS, R.; MOORE, E.; CHEN, L.-D.; ROQUEMORE, W.; VILIMPOC, V.; GOSS, L. A numerical/experimental study of the dynamic structure of a buoyant jet diffusion flame. **Theoretical and Computational Fluid Dynamics**, v. 6, n. 2, p. 113–123, 1994. 58

DAVIS, R. W.; MOORE, E. F.; ROQUEMORE, W. M.; CHEN, L. D.; VILIMPOC, V.; GOSS, L. P. Time evolution of a buoyant jet diffusion flame. **Symposium (International) on Combustion**, v. 24, p. 303–310, 1992. 14

DONINI, M. S.; CRISTALDO, C. F. C.; FACHINI, F. F. Buoyant tsuji diffusion flames: global flame structure and flow field. **Journal of Fluid Mechanics**, v. 895, p. A17, 2020. 8, 30

DOURADO, W. M.; BRUEL, P.; AZEVEDO, J. L. A time-accurate pseudo-compressibility approach based on an unstructured hybrid finite volume technique applied to unsteady turbulent premixed flame propagation. **International Journal for Numerical Methods in Fluids**, v. 44, n. 10, p. 1063–1091, 2004. 30

DREIER, T.; LANGE, B.; WOLFRUM, J.; ZAHN, M.; BEHRENDT, F.; WARNATZ, J. Comparison of cars measurements and calculations of the structure of laminar methane-air counterflow diffusion flames. **Berichte der Bunsengesellschaft für physikalische Chemie**, v. 90, n. 11, p. 1010–1015, 1986. xvi, 56

DUROX, D.; YUAN, T.; BAILLOT, F.; MOST, J. M. Premixed and diffusion dlames in a centrifuge. **Combustion Flame**, v. 102, p. 501–511, 1995. 14

DURãO, D. F. G.; WHITELAW, J. H. Instantaneous velocity and temperature measurements in oscillating diffusion flames. **Proceedings of the Royal Society London A**, v. 338, p. 479–501, 1974. 13

EICKHOFF, H.; WINANDY, A. Visualization of vortex formation in jet diffusion flame. **Combustion Flame**, v. 60, p. 99–101, 1985. 13

EISEMAN, P. R. A multi-surface method of coordinate generation. **Journal of Computational Physics**, v. 33, n. 1, p. 118–150, 1979. 39

ELLZEY, J. L.; ORAN, E. S. Effects of heat release and gravity on an unsteady diffusion flame. **Symposium (International) on Combustion**, v. 23, p. 1635–1640, 1990. 14

FACHINI, F. F.; SESHADRI, K. Rate-ratio asymptotic analysis of nonpremixed n-heptane flames. **Combustion Science and Technology**, v. 175, p. 125–155, 2003. 71

FLEMING, G. C. **Structure and stability of buoyant diffusion flames**. [S.l.]: California Institute of Technology, 1982. Thesis. 13

FLETCHER, C. **Computational techniques for fluid dynamics 2: specific techniques for different flow categories**. [S.l.: s.n.], 2012. 36

FORNBERG, B. A numerical study of steady viscous flow past a circular cylinder. **Journal of Fluid Mechanics**, v. 98, p. 819–855, 1980. 84

GHIA, U.; GHIA, K. N.; SHIN, C. High-re solutions for incompressible flow using the navier-stokes equations and a multigrid method. **Journal of Computational Physics**, v. 48, n. 3, p. 387–411, 1982. xv, 48, 49

GRANT, A. J.; JONES, J. M. Low-frequency diffusion flame oscillations. **Combustion and Flame**, v. 25, p. 153–160, 1975. 13

HAN, B.; IBARRETA, A.; SUNG, C.; T'IEN, J. S. Experimental low-stretch gaseous diffusion flames in buoyancy-induced flowfields. **Proceedings of Combustion Institution**, v. 30, p. 527–537, 2005. 7

HAYASE, T.; HUMPHREY, J.; GREIF, R. A consistently formulated quick scheme for fast and stable convergence using finite-volume iterative calculation procedures. **Journal of Computational Physics**, v. 98, n. 1, p. 108–118, 1992. 36, 37

HODGES, B. R. An artificial compressibility method for 1d simulation of open-channel and pressurized-pipe flow. **Water**, v. 12, n. 6, p. 1727, 2020. 30

JACONO, D. L.; PAPAS, P.; MATALON, M.; MONKEWITZ, P. An experimental realization of an unstrained planar diffusion flame. **Proceedings of Combustion Institution**, v. 30, p. 501–509, 2005. 7

KATTA, V. R.; ROQUEMORE, W. M. Role of inner and outer structures in transitional jet diffusion flame. **Combustion Flame**, v. 92, p. 274–282, 1993. 14

KIM, B.; LEE, D.; HA, M.; YOON, H. A numerical study of natural convection in a square enclosure with a circular cylinder at different vertical locations. **International Journal of Heat and Mass Transfer**, v. 51, n. 7-8, p. 1888–1906, 2008. xv, 49, 50, 51

KIMURA, I. Stability of laminar-jet flames. **Symposium (International) on Combustion**, v. 10, p. 1295–1300, 1965. 13

LAW, C. **Combustion physics**. [S.l.]: Cambridge University Press, 2006. 21, 23

LEONARD, B. P. A stable and accurate convective modelling procedure based on quadratic upstream interpolation. **Computer Methods in Applied Mechanics and Engineering**, v. 19, n. 1, p. 59–98, 1979. 36

LI, Z.; NAVON, I. M.; HUSSAINI, M. Y.; DIMET, F.-X. L. Optimal control of cylinder wakes via suction and blowing. **Computers & Fluids**, v. 32, p. 149–171, 2003. 82

MALALASEKERA, W. M. G.; VERSTEEG, H. K.; GILCHRIST, K. A review of research and an experimental study on the pulsation of buoyant diffusion flames and pool fires. **Fire Materails**, v. 20, p. 261–271, 1996. 14

MORENO-BOZA, D.; COENEN, W.; SEVILLA, A.; CARPIO, J.; SÁNCHEZ, A. L.; náN, A. L. Diffusion-flame flickering as a hydrodynamic global mode. **Journal of Fluid Mechanics**, v. 798, p. 997–1014, 2016. 14

NALLASAMY, M.; PRASAD, K. K. On cavity flow at high reynolds numbers. **Journal of Fluid Mechanics**, v. 79, n. 2, p. 391–414, 1977. xv, 48, 49

ORAN, E. S.; BORIS, J. P. **Numerical simulation of reactive flow**. [S.l.]: Cambridge University Press, 2005. 30

PETERS, N. Local quenching due to flame stretch and non-premixed turbulent combustion. **Combustion Science and Technology**, v. 30, p. 1–17, 1983. 7

_____. Laminar diffusion flamelet models in non-premixed turbulent combustion. **Progress in Energy and Combustion Science**, v. 10, p. 319–339, 1984. 7

PETERS, N.; WILLIAMS, F. A. The asymptotic structure of stoichiometric methane-air flames. **Combustion and Flame**, v. 68, p. 185–207, 1987. 71

QIAN, J.; LAW, C. On the spreading of unsteady cylindrical diffusion flames. **Combustion and Flame**, v. 110, n. 1-2, p. 152–162, 1997. 9, 76, 78

ROBERTS, G. **Lecture Notes in Physics**. [S.l.]: Springer, 1971. 171–176 p. 39

ROGERS, S. E.; KWAK, D. Numerical solution of the incompressible navier-stokes equations for steady and time-dependent problems. In: 27TH AEROSPACE SCIENCES MEETING. **AIAA Meeting Paper**. [S.l.], 1989. v. 89, n. 0463. 28

SATO, H.; AMAGAI, K.; ARAI, M. Diffusion flames and their flickering motions related with froude number under various gravity levels. **Combustion Flame**, v. 123, p. 107–118, 2000. xix, 14, 59, 89, 104

_____. **Scale modeling of puffing frequencies in pool fires related with Froude number**. [S.l.]: Springer Science+Business, 2008. 14

SATO, H.; KUSHIDA, G.; AMAGAI, K.; ARAI, M. Numerical analysis of the gravitational effects on the buoyancy-driven fluctuations in diffusion flames. **Proceedings of Combustion Institution**, v. 29, p. 1671–1678, 2002. 14

SCHÄFER, M.; TUREK, S.; DURST, F.; KRAUSE, E.; RANNACHER, R. Benchmark computations of laminar flow around a cylinder. In: HIRSCHEL, E. H. E. (Ed.). **Flow simulation with high-performance computers II**. [S.l.]: Springer, 1996. p. 547–566. 51, 52

SCHLICHTING, H.; GERSTEN, K. **Boundary-layer theory**. [S.l.]: Springer, 2016. 41

SEE, Y. C.; IHME, M. Effects of finite-rate chemistry and detailed transport on the instability of jet diffusion flames. **Journal of Fluid Mechanics**, v. 745, p. 647–681, 2014. 14

SEN, U.; MUKHOPADHYAY, A.; SEN, S. Effects of fluid injection on dynamics of flow past a circular cylinder. **European Journal of Mechanics-B/Fluids**, v. 61, p. 187–199, 2017. 80, 85

SESHADRI, K.; PETERS, N. Asymptotic structure and extinction of methane-air diffusion flames. **Combustion Flame**, v. 73, p. 23–44, 1988. 71

SHAPIRO, E.; DRIKAKIS, D. Artificial compressibility, characteristics-based schemes for variable density, incompressible, multi-species flows. part i. derivation of different formulations and constant density limit. **Journal of Computational Physics**, v. 210, n. 2, p. 584–607, 2005. 30, 54

SOH, W.; GOODRICH, J. W. Unsteady solution of incompressible navier-stokes equations. **Journal of Computational Physics**, v. 79, n. 1, p. 113–134, 1988. 28

TOONG, T. Y.; SALANT, R. F.; STOPFORD, J.; ANDERSON, G. Y. Mechanisms of combustion instability. **Symposium (International) on Combustion**, v. 10, p. 1301–1313, 1965. 13, 59

TSA, S.-S.; CHEN, C.-H. Flame stabilization over a tsuji burner by four-step chemical reaction. **Combustion Science and Technology**, v. 175, n. 11, p. 2061–2093, 2003. xvi, 9, 56, 57, 89

TSUJI, H. Counterflow diffusion flames. **Progress in Energy and Combustion Science**, v. 8, p. 93–119, 1982. 7

TSUJI, H.; YAMAOKA, I. The counterflow diffusion flame in the forward stagnation region of a porous cylinder. **Symposium (International) on Combustion**, v. 11, p. 979–984, 1967. 1, 9, 55, 73, 89

_____. The structure of counterflow diffusion flames in the forward stagnation region of a porous cylinder. **Symposium (International) on Combustion**, v. 12, p. 997–100, 1969. 65

VERSTEEG, H. K.; MALALASEKERA, W. **An introduction to computational fluid dynamics: the finite volume method**. [S.l.]: Pearson education, 2007. 37

WILLIAMS, F. A. **Combustion theory: fundamental theory of chemically reacting flow systems**. [S.l.]: Benjamin/Cummings Publisher, 1985. 21

WITHINGTON, J.; YANG, V.; SHUEN, J. A time-accurate implicit method for chemically reacting flows at all mach numbers. In: 29TH AEROSPACE SCIENCES MEETING. **AIAA Meeting Paper**. [S.l.], 1991. p. 581. 27

WOHL, K.; KAPP, N. M.; GAZLEY, C. Stability of open flames. **Symposium (International) on Combustion**, v. 3, p. 3–21, 1949. 13

XIA, X.; P.ZHANG. A vortex-dynamical scaling theory for flickering buoyant diffusion flames. **Journal of Fluid Mechanics**, v. 855, p. 1156–1169, 2018. 14, 89

APPENDIX A - BUOYANT TSUJI

A.1 Stagnation point and strain rate estimation

Considering a fluid particle, determined by y_p, leaving the downside surface of the burner and displacing downwards on the symmetry axis, the force balance equation for determining its trajectory is given by

$$\frac{d^2 y_p}{dt^2} = \frac{1}{Fr^2}\left(1 - \frac{1}{T}\right) \tag{A.1}$$

Diffusion flames established in a counterflow configuration are known to sit in the oxidant side of a distance from the stagnation plane which scales as $Pe^{-1/2}$, thus, the flame position can be estimated by $y_f^- \sim y_{st} - Pe^{-1/2}$.

In this analysis, a linear temperature profile from the burner up to the flame is imposed, i.e., $T \sim T_b + \Delta_T(y_p + 1)$, with $\Delta_T = (T_f - T_b)/(y_f^- + 1)$.

Multiplying Equation (A.1) by $2dy_p/dt$ and integrating analytically, the fluid velocity on the symmetry axis below the burner is determined, by

$$(Fr^2)\left(\frac{d}{dt}(y_p + 1)\right)^2 = 2(y_p + 1) - \frac{2}{\Delta_T} ln\left(1 + \frac{\Delta_T(y_p + 1)}{T_b}\right) + (Fr^2) \tag{A.2}$$

in which the boundary condition at the burner surface was applied, i.e., $v = y_p' = -1$ at $y_p = -1$. The position of the stagnation point $y_p = y_{st}$ is found with the zero velocity condition $y_p' = 0$,

$$\frac{(y_{st} + 1)}{(y_f^- + 1)} + \frac{(Fr)^2}{2(y_f^- + 1)} = \frac{1}{(T_f - T_b)} ln\left(1 + \frac{(T_f - T_b)}{T_b}\frac{(y_{st} + 1)}{(y_f^- + 1)}\right) \tag{A.3}$$

A way to find the solution of Equation (A.3) is made in two steps. First, the position y_{tan} at which the functions of the left and right hand sides have the same tangent is calculated. Second, the condition for $(Fr)^2/2(y_f^- + 1)$ that makes the two functions to meet at y_{tan} is determined. Following this strategy, the stagnation point is determined by

$$(y_{st} + 1) = \frac{1 - T_b}{T_f - T_b}(y_f^- + 1) \tag{A.4}$$

and the Froude number is

$$\frac{(Fr)^2}{2(y_f^- + 1)} = \frac{ln(1/T_b) + T_b - 1}{T_f - T_b} \tag{A.5}$$

Imposing the flame position $y_p = y_f^-$ into Equation (A.2), the velocity $v_f = v(y_f^-)$ can be estimated by

$$(v_f - 1)(v_f + 1) = \frac{|y_f^- + 1|}{(Fr)^2} \left(\frac{ln(T_f/T_b)}{T_f - T_b} - 1 \right) \tag{A.6}$$

From Equation (A.6), the velocity of the gases at the flame is independent on the flame position for the particular ambient-atmosphere temperature $\hat{T}_{\infty,c} = (\hat{T}_f - \hat{T}_b)/ln(\hat{T}_f/\hat{T}_b)$ and its value is $v_f = 1$. The velocity is positive because the flame is in the oxidant side of the counterflow. For the addressed conditions $\hat{T}_b = 300K$ and $S = 9.5$, which leads to $\hat{T}_f = 2050K$ and $\hat{T}_{\infty,c}$ is $910K$. For $\hat{T}_\infty > 910K$, the velocity is $v_f > 1$.

The strain rate at the flame y_f^- is estimated by the derivative in y direction of Equation (A.6), according to

$$\left.\frac{dv}{dy_p}\right|_{y_f^-} = \frac{\Delta^2}{(Fr)^2 \; v_f} \tag{A.7}$$

which reveals its dependence on the Froude number and on the temperature of the flame, the fuel injected and the ambient atmosphere. For instance,

$$\left.\frac{dv}{dy_p}\right|_{y_f^-} \left[\begin{array}{c} > \\ = \\ < \end{array} \right] \left(\frac{\Delta}{Fr}\right)^2, \quad \text{for} \quad \left\{ \begin{array}{l} \hat{T}_\infty < \hat{T}_{\infty,c} \; (v_f < 1) \\ \hat{T}_\infty = \hat{T}_{\infty,c} \; (v_f = 1) \\ \hat{T}_\infty > \hat{T}_{\infty,c} \; (v_f > 1) \end{array} \right.$$

APPENDIX B - NUMERICAL EQUATIONS

B.1 Continuity

In constructing the staggered grid arrangement, the additional nodes are set up surrounding the physical boundary, as illustrated in Figure B.1. The calculations are performed at internal nodes only ($I = 2$ to $NI - 1$ and $J = 2$ to $NJ - 1$). Two notable features of the arrangement are (i) the physical boundaries coincide with scalar control volume boundaries and (ii) the nodes just outside the inlet of the domain (along $I = 1$ in Figure B.1) are available to store the inlet conditions. This enables the introduction of boundary conditions to be achieved with small modifications to the discretised equations for near-boundary internal nodes.

Figure B.1 - Pressure Scalar cell at a boundary.

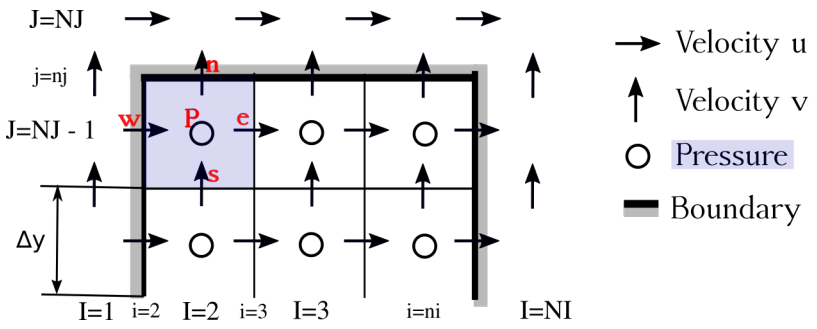

SOURCE: The Author.

$$\frac{\partial \rho}{\partial t} + \frac{1}{\beta}\frac{\partial p}{\partial \tau} + \frac{1}{x^\eta}\frac{\partial (x^\eta \rho u)}{\partial x} + \frac{\partial (\rho v)}{\partial y} = 0 \tag{B.1}$$

$$\int \frac{\partial \rho}{\partial t} x^\eta dx dy = x_P^\eta \frac{\partial \rho_P}{\partial t} \Delta\Omega \tag{B.2}$$

Defining $\Delta\Omega = \Delta x \Delta y$.

The third therm:

$$\int \frac{1}{x^\eta}\frac{\partial (x^\eta \rho u)}{\partial x} x^\eta dx dy = (x^\eta \rho u)|_w^e \Delta y = \left[x_e^\eta \frac{\rho_E + \rho_P}{2} u_e - x_w^\eta \frac{\rho_W + \rho_P}{2} u_w \right] \Delta y \tag{B.3}$$

The fourth term:

$$\int \frac{\partial(\rho v)}{\partial y} x^{\eta} dxdy = x_P^{\eta}(\rho v)|_s^n \Delta x = x_P^{\eta}\left[\frac{\rho_N + \rho_P}{2} v_n - \frac{\rho_S + \rho_P}{2} v_s\right]\Delta x \tag{B.4}$$

$$x_P^{\eta}\Delta\Omega\frac{\partial \rho_P}{\partial t} + (x^{\eta}\rho u)|_w^e \Delta y + x_P^{\eta}(\rho v)|_s^n \Delta x = 0 \tag{B.5}$$

$$\boxed{x_P^{\eta}\Delta\Omega\frac{\partial \rho_P}{\partial t} + \left[x_e^{\eta}\frac{\rho_E + \rho_P}{2} u_e - x_w^{\eta}\frac{\rho_W + \rho_P}{2} u_w\right]\Delta y + x_P^{\eta}\left[\frac{\rho_N + \rho_P}{2} v_n - \frac{\rho_S + \rho_P}{2} v_s\right]\Delta x = 0} \tag{B.6}$$

B.2 u-Momentum

Figure B.2 - u-Momentum cell at a boundary.

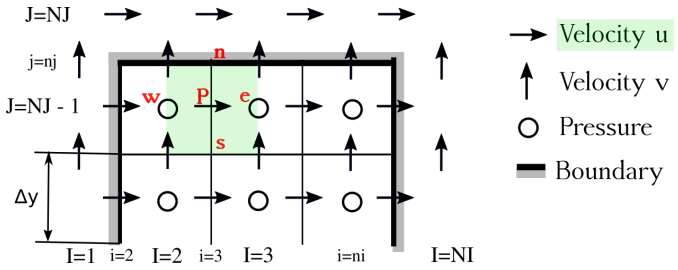

SOURCE: The Author.

$$\int \frac{\partial \rho u}{\partial t} x^{\eta} dxdy + \int \frac{1}{x^{\eta}} \frac{\partial x^{\eta}\rho u u}{\partial x} x^{\eta} dxdy + \int \frac{\partial \rho v u}{\partial y} x^{\eta} dxdy = R(u, v, p) \tag{B.7}$$

$$\int \frac{1}{x^{\eta}} \frac{\partial x^{\eta}\rho u u}{\partial x} x^{\eta} dxdy = x^{\eta}\rho u u|_w^e \Delta y \tag{B.8}$$

$$\int \frac{\partial \rho v u}{\partial y} x^{\eta} dxdy = \rho v u|_s^n x_P^{\eta} \Delta x \tag{B.9}$$

$$x_P^{\eta}\left(\rho\frac{\partial u}{\partial t} + u\frac{\partial \rho}{\partial t}\right)_P \Delta x\Delta y + x^{\eta}\rho u u|_w^e \Delta y + \rho v u|_s^n x_P^{\eta}\Delta x = R(u, v, p) \tag{B.10}$$

$$x_P^\eta \rho_P \left.\frac{\partial u}{\partial t}\right|_P \Delta\Omega + x_P^\eta u_P \left.\frac{\partial \rho}{\partial t}\right|_P \Delta\Omega + x^\eta \rho u u|_w^e \Delta y + \rho v u|_s^n x_P^\eta \Delta x = R(u,v,p) \quad \text{(B.11)}$$

$$x_P^\eta \rho_P \left.\frac{\partial u}{\partial t}\right|_P \Delta\Omega - u_P\left[(x^\eta \rho u)|_w^e \Delta y + x_P^\eta (\rho v)|_s^n \Delta x\right] + x^\eta \rho u u|_w^e \Delta y + \rho v u|_s^n x_P^\eta \Delta x = R(u,v,p) \quad \text{(B.12)}$$

$$x_P^\eta \rho_P \frac{\partial u}{\partial t}|_P \Delta\Omega + x^\eta \rho u u|_w^e \Delta y - u_P (x^\eta \rho u)|_w^e \Delta y + \rho v u|_s^n x_P^\eta \Delta x - u_P x_P^\eta (\rho v)|_s^n \Delta x = R(u,v,p) \quad \text{(B.13)}$$

$$\begin{aligned} x_P^\eta \rho_P \left.\frac{\partial u}{\partial t}\right|_P \Delta\Omega + \left[(x^\eta \rho u)_e u_e - (x^\eta \rho u)_w u_w\right] \Delta y \\ - \left[(x^\eta \rho u)_e - (x^\eta \rho u)_w\right] u_P \Delta y + \left[(\rho v)_n u_n - (\rho v)_s u_s\right] x_P^\eta \Delta x \\ - \left[(\rho v)_n - (\rho v)_s\right] x_P^\eta u_P \Delta x = R(u,v,p) \end{aligned} \quad \text{(B.14)}$$

Defining the fluxes:

$$F_i = (x^\eta \rho u)_i \Delta y$$

$$F_j = (\rho v)_j x_P^\eta \Delta x$$

where $i = [w, e]$ and $j = [s, n]$:

$$\begin{aligned} x_P^\eta \rho_P \left.\frac{\partial u}{\partial t}\right|_P \Delta\Omega + F_e u_e - F_w u_w - (F_e - F_w) u_P + F_n u_n - F_s u_s \\ - (F_n - F_s) u_P = R(u,v,p) \end{aligned} \quad \text{(B.15)}$$

Defining $F_P = (F_w - F_e + F_s - F_n)$, then:

$$x_P^\eta \rho_P \left.\frac{\partial u}{\partial t}\right|_P \Delta\Omega + F_e u_e - F_w u_w + F_n u_n - F_s u_s + F_P u_P = R(u,v,p) \tag{B.16}$$

Discrization of the right-hand-side without the source terms:

$$R(u,v,p) = \frac{\partial p}{\partial r} + \frac{1}{x^\eta}\frac{\partial}{\partial x}\left(x^\eta \mu \frac{\partial u}{\partial x}\right) + \frac{\partial}{\partial y}\left(\mu \frac{\partial u}{\partial y}\right) \tag{B.17}$$

$$\int R(u,v,p) x^\eta dxdy = x_P^\eta \left.\frac{\partial p}{\partial x}\right|_w^e \Delta\Omega + \left.\left(x^\eta \mu \frac{\partial u}{\partial x}\right)\right|_w^e \Delta y + \left.\left(\mu \frac{\partial u}{\partial y}\right)\right|_s^n x_P^\eta \Delta x \tag{B.18}$$

$$\begin{aligned}\int R(u,v,p) r dxdy = x_P^\eta \frac{p_e - p_w}{\Delta x}\Delta\Omega + \left[x_e^\eta \mu_e \frac{u_E - u_P}{\delta x_e} - x_w^\eta \mu_w \frac{u_P - u_W}{\delta r_w}\right]\Delta y \\ + \left[\mu_n \frac{u_N - u_P}{\delta z_n} - \mu_s \frac{u_P - u_S}{\delta z_s}\right] x_P^\eta \Delta x\end{aligned} \tag{B.19}$$

$$D_i = \frac{x_i^\eta \mu_i}{\delta r_i}\Delta y$$

$$D_j = \frac{\mu_j}{\delta z_j} x_P^\eta \Delta x$$

$$\begin{aligned}\int R(u,v,p) r dxdy = x_P^\eta \frac{p_e - p_w}{\Delta x}\Delta\Omega + D_e(u_E - u_P) - D_w(u_P - u_W) \\ + D_n(u_N - u_P) - D_s(u_P - u_S)\end{aligned} \tag{B.20}$$

$$\begin{aligned}x_P^\eta \rho_P \left.\frac{\partial u}{\partial t}\right|_P \Delta\Omega + F_e u_e - F_w u_w + F_n u_n - F_s u_s + F_P u_P \\ = x_P^\eta \frac{p_e - p_w}{\Delta x}\Delta\Omega + D_e(u_E - u_P) - D_w(u_P - u_W) \\ + D_n(u_N - u_P) - D_s(u_P - u_S)\end{aligned} \tag{B.21}$$

B.3 v-Momentum

Figure B.3 - v-Momentum cell at a boundary.

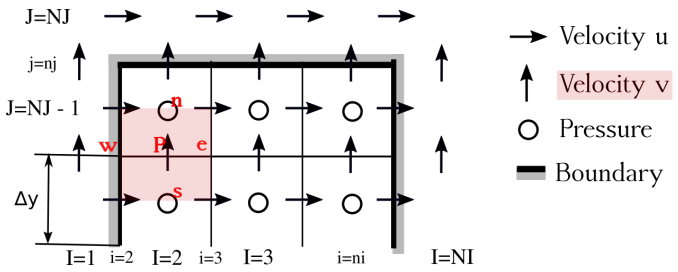

SOURCE: The Author.

$$\int \frac{\partial \rho v}{\partial t} x^{\eta} dxdy + \int \frac{1}{x^{\eta}} \frac{\partial x^{\eta} \rho uv}{\partial x} x^{\eta} dxdy + \int \frac{\partial \rho vv}{\partial y} x^{\eta} dxdy = R(u, v, p) \tag{B.22}$$

$$\int \frac{1}{x^{\eta}} \frac{\partial x \rho uv}{\partial x} x dxdy = x^{\eta} \rho uv|_{w}^{e} \Delta y \tag{B.23}$$

$$\int \frac{\partial \rho vv}{\partial y} x dxdy = \rho vv|_{s}^{n} x_P^{\eta} \Delta x \tag{B.24}$$

$$x_P^{\eta} \left(\rho \frac{\partial v}{\partial t} + v \frac{\partial \rho}{\partial t} \right)_P \Delta x \Delta y + x^{\eta} \rho uv|_{w}^{e} \Delta y + \rho vv|_{s}^{n} x_P^{\eta} \Delta x = R(u, v, p) \tag{B.25}$$

$$x_P^{\eta} \rho_P \left. \frac{\partial v}{\partial t} \right|_P \Delta\Omega + x_P^{\eta} v_P \left. \frac{\partial \rho}{\partial t} \right|_P \Delta\Omega + x^{\eta} \rho uv|_{w}^{e} \Delta y + \rho vv|_{s}^{n} x_P^{\eta} \Delta x = R(u, v, p) \tag{B.26}$$

$$x_P^{\eta} \rho_P \left. \frac{\partial v}{\partial t} \right|_P \Delta\Omega - v_P \left[(x^{\eta} \rho u)|_{w}^{e} \Delta y + x_P^{\eta} (\rho v)|_{s}^{n} \Delta x \right] + x^{\eta} \rho uv|_{w}^{e} \Delta y + \rho vv|_{s}^{n} x_P^{\eta} \Delta x = R(u, v, p) \tag{B.27}$$

$$x_P^{\eta} \rho_P \frac{\partial v}{\partial t}|_P \Delta\Omega + x^{\eta} \rho uv|_{w}^{e} \Delta y - v_P (x^{\eta} \rho u)|_{w}^{e} \Delta y + \rho vv|_{s}^{n} x_P^{\eta} \Delta x - v_P x_P^{\eta} (\rho v)|_{s}^{n} \Delta x = R(u, v, p) \tag{B.28}$$

$$x_P^\eta \rho_P \left.\frac{\partial v}{\partial t}\right|_P \Delta\Omega + \left[(x^\eta \rho u)_e v_e - (x^\eta \rho u)_w v_w\right] \Delta y$$
$$- \left[(x^\eta \rho u)_e - (x^\eta \rho u)_w\right] v_P \Delta y + \left[(\rho v)_n v_n - (\rho v)_s v_s\right] x_P^\eta \Delta x$$
$$- \left[(\rho v)_n - (\rho v)_s\right] x_P^\eta v_P \Delta x = R(u, v, p) \tag{B.29}$$

Defining the fluxes:

$$F_{i(e,w)} = (x^\eta \rho u)_i \Delta y$$
$$F_{i(n,s)} = (\rho v)_i x_P^\eta \Delta x$$

$$x_P^\eta \rho_P \left.\frac{\partial v}{\partial t}\right|_P \Delta\Omega + F_e v_e - F_w v_w - (F_e - F_w) v_P + F_n v_n - F_s v_s$$
$$- (F_n - F_s) v_P = R(u, v, p) \tag{B.30}$$

Defining $F_P = (F_w - F_e + F_s - F_n)$, then:

$$\boxed{x_P^\eta \rho_P \left.\frac{\partial v}{\partial t}\right|_P \Delta\Omega + F_e v_e - F_w v_w + F_n v_n - F_s v_s + F_P v_P = R(u, v, p)} \tag{B.31}$$

B.4 Enthalpy excess equation

$$\int \frac{\partial \rho H}{\partial t} x^\eta dx dy + \int \frac{1}{x^\eta} \frac{\partial x^\eta \rho u H}{\partial x} x^\eta dx dy + \int \frac{\partial \rho v H}{\partial y} x^\eta dx dy = R(H) \tag{B.32}$$

$$\int \frac{1}{x^\eta} \frac{\partial x^\eta \rho u H}{\partial x} x^\eta dx dy = x^\eta \rho u H|_w^e \Delta y \tag{B.33}$$

$$\int \frac{\partial \rho v H}{\partial y} x dx dy = \rho v H|_s^n x_P^\eta \Delta x \tag{B.34}$$

Figure B.4 - Enthalpy excess scalar cell at a boundary.

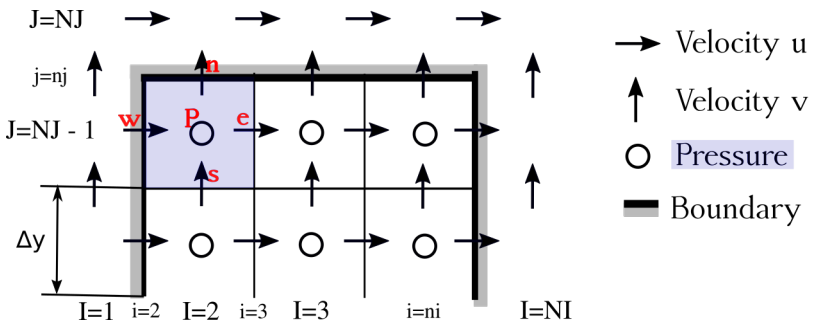

SOURCE: The Author.

$$x_P^\eta \left(\rho\frac{\partial H}{\partial t} + H\frac{\partial \rho}{\partial t}\right)_P \Delta x\Delta y + x^\eta \rho u H|_w^e \Delta y + \rho v H|_s^n x_P^\eta \Delta x = R(H) \tag{B.35}$$

$$x_P^\eta \rho_P \left.\frac{\partial H}{\partial t}\right|_P \Delta\Omega + x_P^\eta H_P \left.\frac{\partial \rho}{\partial t}\right|_P \Delta\Omega + x^\eta \rho u H|_w^e \Delta y + \rho v H|_s^n x_P^\eta \Delta x = R(H) \tag{B.36}$$

$$x_P^\eta \rho_P \left.\frac{\partial H}{\partial t}\right|_P \Delta\Omega - H_P\left[(x^\eta \rho u)|_w^e \Delta y + x_P^\eta (\rho v)|_s^n \Delta x\right] + x^\eta \rho u H|_w^e \Delta y + \rho v H|_s^n x_P^\eta \Delta x = R(H) \tag{B.37}$$

$$x_P^\eta \rho_P \left.\frac{\partial H}{\partial t}\right|_P \Delta\Omega + x^\eta \rho u H|_w^e \Delta y - H_P (x^\eta \rho u)|_w^e \Delta y + \rho v H|_s^n x_P^\eta \Delta x - H_P x_P^\eta (\rho v)|_s^n \Delta x = R(H) \tag{B.38}$$

$$\begin{aligned} x_P^\eta \rho_P \left.\frac{\partial H}{\partial t}\right|_P \Delta\Omega + \left[(x^\eta \rho u)_e H_e - (x^\eta \rho u)_w H_w\right] \Delta y \\ - \left[(x^\eta \rho u)_e - (x^\eta \rho u)_w\right] H_P \Delta y + \left[(\rho v)_n H_n - (\rho v)_s H_s\right] x_P^\eta \Delta x \\ - \left[(\rho v)_n - (\rho v)_s\right] x_P^\eta H_P \Delta x = R(H) \end{aligned} \tag{B.39}$$

Defining the fluxes:

$$F_i = (x^\eta \rho u)_i \Delta y$$

$$F_j = (\rho v)_j x_P^\eta \Delta x$$

where $i = [w, e]$ and $j = [s, n]$:

$$x_P^\eta \rho_P \left.\frac{\partial H}{\partial t}\right|_P \Delta\Omega + F_e H_e - F_w H_w - (F_e - F_w) H_P + F_n H_n - F_s H_s - (F_n - F_s) H_P = R(H) \tag{B.40}$$

Defining $F_P = (F_w - F_e + F_s - F_n)$, then:

$$\rho_P \left.\frac{\partial H}{\partial t}\right|_P \Delta\Omega + F_e H_e - F_w H_w + F_n H_n - F_s H_s + F_P H_P = R(H) \tag{B.41}$$

$$R(H) = \frac{1}{x^\eta}\frac{\partial}{\partial x}\left(x^\eta \rho \mathcal{D}_T \frac{\partial H}{\partial x}\right) + \frac{\partial}{\partial y}\left(\rho \mathcal{D}_T \frac{\partial H}{\partial y}\right) \tag{B.42}$$

$$\int R(H) x^\eta dx dy = \left(x^\eta \rho \mathcal{D}_T \frac{\partial H}{\partial x}\right)\Bigg|_w^e \Delta y + \left(\rho \mathcal{D}_T \frac{\partial H}{\partial y}\right)\Bigg|_s^n x_P^\eta \Delta x \tag{B.43}$$

$$\int R(H) x^\eta dx dy = \left[x_e^\eta \rho_e \mathcal{D}_{Te} \frac{H_E - H_P}{\delta x_e} - x_w^\eta \rho_w \mathcal{D}_{Tw} \frac{H_P - H_W}{\delta x_w}\right] \Delta y + \left[\rho_n \mathcal{D}_{Tn} \frac{H_N - H_P}{\delta y_n} - \rho_s \mathcal{D}_{Ts} \frac{H_P - H_S}{\delta y_s}\right] x_P^\eta \Delta x \tag{B.44}$$

$$D_i = \frac{x_i^\eta \rho_i \mathcal{D}_{Ti}}{\delta x_i} \Delta y$$

$$D_j = \frac{\rho_j \mathcal{D}_{Tj}}{\delta y_j} x_P^\eta \Delta x$$

$$\int R(H)x^{\eta}dxdy = D_e(H_E - H_P) - D_w(H_P - H_W) + D_n(H_N - H_P) - D_s(H_P - H_S) \tag{B.45}$$

$$x_P^{\eta}\rho_P \left.\frac{\partial H}{\partial t}\right|_P \Delta\Omega + F_eH_e - F_wH_w + F_nH_n - F_sH_s + F_PH_P = D_e(H_E - H_P) - D_w(H_P - H_W) + D_n(H_N - H_P) - D_s(H_P - H_S) \tag{B.46}$$

Defining $D_p = (D_w + D_e + D_s + D_n)$, then:

$$x_P^{\eta}\rho_P \left.\frac{\partial H}{\partial t}\right|_P \Delta\Omega + F_eH_e - F_wH_w + F_nH_n - F_sH_s + F_PH_P = -D_pH_P + D_eH_E + D_wH_W + D_nH_N + D_sH_S \tag{B.47}$$

B.5 QUICK scheme

From QUICK scheme, for momentum in x direction:

When $u_w > 0$:

$$u_w = \frac{6}{8}u_W + \frac{3}{8}u_P - \frac{1}{8}u_{WW} \tag{B.48}$$

When $u_e > 0$:

$$u_e = \frac{6}{8}u_P + \frac{3}{8}u_E - \frac{1}{8}u_W \tag{B.49}$$

When $u_s > 0$:

$$u_s = \frac{6}{8}u_S + \frac{3}{8}u_P - \frac{1}{8}u_{SS} \tag{B.50}$$

When $u_n > 0$:

$$u_n = \frac{6}{8}u_P + \frac{3}{8}u_N - \frac{1}{8}u_S \tag{B.51}$$

$$x_P^{\eta}\rho_P \left.\frac{\partial u}{\partial t}\right|_P \Delta\Omega + F_e\left(\frac{6}{8}u_P + \frac{3}{8}u_E - \frac{1}{8}u_W\right) - F_w\left(\frac{6}{8}u_W + \frac{3}{8}u_P - \frac{1}{8}u_{WW}\right)$$
$$+ F_n\left(\frac{6}{8}u_P + \frac{3}{8}u_N - \frac{1}{8}u_S\right) - F_s\left(\frac{6}{8}u_S + \frac{3}{8}u_P - \frac{1}{8}u_{SS}\right) + F_P u_P =$$
$$S_{M_u} + D_e(u_E - u_P) - D_w(u_P - u_W) + D_n(u_N - u_P) - D_s(u_P - u_S) \quad \text{(B.52)}$$

$$x_P^{\eta}\rho_P \left.\frac{\partial u}{\partial t}\right|_P \Delta\Omega + \left(D_e + \frac{6}{8}F_e + D_w - \frac{3}{8}F_w + D_n + \frac{6}{8}F_n + D_s - \frac{3}{8}F_s\right)u_P + F_P u_P =$$
$$+ S_{M_u} + \left(D_w + \frac{1}{8}F_e + \frac{6}{8}F_w\right)u_W + \left(D_e - \frac{3}{8}F_e\right)u_E +$$
$$\left(D_s + \frac{1}{8}F_n + \frac{6}{8}F_s\right)u_S + \left(D_n - \frac{3}{8}F_n\right)u_N +$$
$$\left(-\frac{1}{8}F_w\right)u_{WW} + \left(-\frac{1}{8}F_s\right)u_{SS} \quad \text{(B.53)}$$

The standard form for discretised equations

$$x_P^{\eta}\rho_P \left.\frac{\partial u}{\partial t}\right|_P \Delta\Omega + a_P u_P + F_P u_P = c + a_W u_W + a_E u_E + a_S u_S + a_N u_N + a_{WW} u_{WW} + a_{SS} u_{SS} \quad \text{(B.54)}$$

Where

$$a_P = D_e + \frac{6}{8}F_e + D_w - \frac{3}{8}F_w + D_n + \frac{6}{8}F_n + D_s - \frac{3}{8}F_s \quad \text{(B.55)}$$

$$a_W = D_w + \frac{1}{8}F_e + \frac{6}{8}F_w \quad \text{(B.56)}$$

$$a_E = D_e - \frac{3}{8}F_e \quad \text{(B.57)}$$

$$a_S = D_s + \frac{1}{8}F_n + \frac{6}{8}F_s \quad \text{(B.58)}$$

$$a_N = D_n - \frac{3}{8}F_n \tag{B.59}$$

$$a_{WW} = -\frac{1}{8}F_w \tag{B.60}$$

$$a_{SS} = -\frac{1}{8}F_e \tag{B.61}$$

$$c = S_{M_u} \tag{B.62}$$

Repeating for other velocities directions and signals:

$$x_P^{\eta}\rho_P \left.\frac{\partial u}{\partial t}\right|_P \Delta\Omega + a_P u_P + F_P u_P = c + a_W u_W + a_E u_E + a_S u_S + a_N u_N + a_{WW} u_{WW} + a_{SS} u_{SS} + a_{EE} u_{EE} + a_{NN} u_{NN} \tag{B.63}$$

$$a_P = a_W + a_E + a_S + a_N + a_{WW} + a_{EE} + a_{SS} + a_{NN} + F_e - F_w + F_n - F_s \tag{B.64}$$

$$a_W = D_w + \frac{6}{8}\alpha_w F_w + \frac{1}{8}\alpha_e F_e + \frac{3}{8}(1-\alpha_w)F_w \tag{B.65}$$

$$a_E = D_e - \frac{3}{8}\alpha_e F_e - \frac{6}{8}(1-\alpha_e)F_e - \frac{1}{8}(1-\alpha_w)F_w \tag{B.66}$$

$$a_S = D_s - \frac{6}{8}\alpha_s F_s + \frac{1}{8}\alpha_n F_n - \frac{3}{8}(1-\alpha_s)F_s \tag{B.67}$$

$$a_N = D_n - \frac{3}{8}\alpha_n F_n - \frac{6}{8}(1-\alpha_n)F_n - \frac{1}{8}(1-\alpha_s)F_s \tag{B.68}$$

$$a_{WW} = -\frac{1}{8}F_w \tag{B.69}$$

$$a_{EE} = \frac{1}{8}(1-\alpha_e)F_e \tag{B.70}$$

$$a_{SS} = -\frac{1}{8}F_s \tag{B.71}$$

$$a_{NN} = \frac{1}{8}(1-\alpha_n)F_n \tag{B.72}$$

$$c = S_{M_u} \tag{B.73}$$

where

$$\begin{array}{llllll} \alpha_w = 1 & \text{for} & F_w > 0 & \text{and} & \alpha_e = 1 & F_e > 0 \\ \alpha_w = 0 & \text{for} & F_w < 0 & \text{and} & \alpha_e = 0 & F_e < 0 \end{array}$$

$$\begin{array}{llllll} \alpha_s = 1 & \text{for} & F_s > 0 & \text{and} & \alpha_n = 1 & F_n > 0 \\ \alpha_s = 0 & \text{for} & F_s < 0 & \text{and} & \alpha_n = 0 & F_n < 0 \end{array}$$